Zinc-Silicate Glasses for Transarterial Chemoembolization of Hepatocellular Carcinoma

by

Nancy B. Kilcup

Submitted in partial fulfilment of the requirements
for the degree of Doctor of Philosophy

at

Dalhousie University
Halifax, Nova Scotia
September 2015

© Copyright by Nancy B. Kilcup, 2015

For Isaac

TABLE OF CONTENTS

LIST OF TABLES

LIST OF FIGURES

ABSTRACT

Drug eluting bead transarterial chemoembolization (DEB-TACE) has emerged as the gold standard therapy for patients diagnosed with hepatocellular carcinoma, the second leading cause of cancer-related deaths worldwide. Presently, DEB-TACE procedures are limited by two factors: (i) particles are radiolucent, making it impossible to determine spatial-temporal distribution within target tissues thus limiting optimum therapy, and (ii) conventional bead technologies require drug pre-loading, which is logistically challenging.

The research presented herein examines these material limitations through two different approaches. The first approach is based on the idea that systems can be optimized for an application by combining multiple components, where each component fulfills a specific role. Towards this end, drug preloaded radiopaque composite embolic microspheres were prepared from polylactic-co-glycolic acid, radiopaque zinc-silicate glass and doxorubicin. Using a design of experiments approach the composition was optimized to provide for maximum radiopacity while drug release was controlled over seven days.

The second approach is one of simplicity and reflects the emerging biomaterial design paradigm that seeks to elicit desired host responses. In this sense therapeutic inorganic ions (TII) released from biomedical glasses are known to promote hard tissue repair and regeneration by triggering angiogenesis and osteogenesis. In DEB-TACE, the desired host response is cell death. Within this framework, two zinc-silicate systems were prepared containing lanthanum and vanadium since these elements are known to have anticancer behavior. The composition-structure-property-function relationships were evaluated based on substitution of lanthanum or vanadium into the glass network. Critically, the ion release capabilities were evaluated in simulated physiological conditions. Increased lanthanum did not dramatically alter the structure of the glass but it did increase the hydrolytic stability of the glasses. Increased vanadium caused polymerization of the Si-network and simultaneously decreased its hydrolytic stability resulting in significant amounts of vanadium release. Exposure of HepG2 cells to vanadium containing extracts resulted in concentration dependent apoptotic cell death.

Biomedical glasses have potential in applications beyond hard tissue repair and regeneration, providing a radiopaque, drug preloaded alternative to existing DEB-TACE materials and a simple means for vectored delivery of TII.

LIST OF ABREVIATIONS AND SYMBOLS USED

%	Percent
%w/v	Weight/volume percent
°C	Degrees Celsius
^{90}Y	Yttrium 90
Å	Angstrom
Abs	Absorbance
Al	Aluminum
ALP	Alkaline phosphatase
AMPS	2-acrylamido-2-methylpropanesulfonate sodium salt
ANOVA	Standard analysis of variance
As	Arsenic
BCLC	Barcelona Clinic Liver Cancer Staging System
BO	Bridging oxygen
C	Carbon
c.	Approximately
Ca	Calcium
CEM	Composite embolic microsphere
Cl	Chlorine
cm	Centimeter
Co	Cobalt
CRC	Colorectal Cancer
CT	Computed Tomography

cTACE	Conventional Transarterial Chemoembolization
CTB	Cell Titer Blue
Cu	Copper
CV	Cell Viability
DCM	Dichloromethane
DEB-TACE	Drug Eluting Bead Transarterial Chemoembolization
DMSO	Dimethyl Sulfoxide
DNA	Deoxyribonucleic Acid
DOE	Design of Experiments
DOX	Doxorubicin
DSC	Differential Scanning Calorimetry
E_d	Single bond strength
EMEM	Eagles Minimum Essential Medium
EXFAS	Extended X-Ray Fine Absorption Structure
F	Fluorine
FBS	Fetal Bovine Serum
FCS	Fetal Calf Serum
FTIR	Fourier Transform Infrared Spectroscopy
g	Grams
Gy	Gray
H	Hydrogen
h	Hour
HBV	Hepatitis B Virus

HCA	Hydroxycarbonate apatite
HCC	Hepatocellular carcinoma
HCV	Hepatitis C Virus
HIF-α	Hypoxia-inducible factor alpha
HU	Hounsfield Units
Hz	Hertz
ICP-OES	Inductively Coupled Plasma Optical Emission Spectroscopy
IRI	Irinotecan
K	Potassium
kcal	Kilocalorie
kHz	KiloHertz
kPa	KiloPascal
kVp	Peak kiloVoltage
La	Lanthanum
MA	Methyl Acrylate
MAS NMR	Magic Angle Spinning Nuclear Magnetic Resonance
mCRC	Metastatic Colorectal Cancer
Mg	Magnesium
mg	Milligram
mL	Milliliter
mm	Millimeter
mol	Mole
MTT	3-(4,5-dimethylthiazol-2-yl)-2,5-diphenyltetrazolium bromide

Na	Sodium
NAAADA	N-acryloyl-aminoacetaldehyde dimethylacetal
NAFLD	Non-Alcoholic Fatty Liver Disease
NBO	Non-Bridging Oxygen
N_c	Network Connectivity
ng	Nanogram
nm	Nanometer
NWF	Network Formers
NWI	Network Intermediates
NWM	Network Modifiers
O	Oxygen
PBS	Phosphate Buffered Saline
Pen	Penicillin
PLGA	Polylactic-co-glycolic acid
ppm	Parts per million
psig	Pounds per square inch
PVA	Polyvinyl alcohol
PVAc	Polyvinyl acetate
RC-DEB	Radiopaque Composite Drug Eluting Beads
RCs	Radiopaque Composite Embolic Microspheres
RNA	Ribonucleic Acid
ROS	Reactive Oxygen Species
rpm	Revolutions Per Minute

RT-PCR	Reverse Transcription Polymerase Chain Reaction
s-PVA	Sulfonated Polyvinyl alcohol
SAP	Super Absorbent Particles
Sb	Antimony
Si	Silicon
Sr	Strontium
Strep	Streptomycin
TACE	Transarterial Chemoembolization
TAE	Transarterial Embolization
TARE	Transarterial Radioembolization
Tc99-MAA	Technetium-99 Macroaggregated Albumin
T_g	Glass Transition Temperature
Ti	Titanium
TII	Therapeutic Inorganic Ions
TIPS	Thermally Induced Phase Separation
TMEDA	Tetramethylethylenediamine
UV-Vis	Ultraviolet-Visible
V	Vanadium
VAc	Vinyl Acetate
VEGF	Vascular Endothelial Growth Factor
wt%	Weight percent
XRD	X-Ray Diffraction
Zn	Zinc

λ	Wavelength
μL	Microliter
μm	Micron
μM	Micromolar

ACKNOWLEDGEMENTS

First and foremost I would like to thank my supervisor, Dr. Daniel Boyd. Your support, patience, guidance and unique perspective have helped to shape my own ideas so much. Thank you for always having your door open for “just one more question”. Your advice and discussions about the research, career paths and future directions have inspired me. I think the statement “Context Nancy! Context” might forever ring in my mind each time I prepare to present my work.

Besides my supervisor, I would like to thank the rest of my thesis committee: Dr. Paul Gratzer and Dr. Bob Abraham for their insightful comments and encouragement. More importantly, for their hard questions, which drove me to expand my research to include different perspectives.

To my collaborators, Seán Gaynard and Dr. Jessica Hayes, at the National University of Ireland in Galway, it has truly been an honour and a pleasure to work with you both. Thank you for hosting me at your institution and taking the time and effort to train me and help make the investigation into cell death mechanisms possible. Your insights into the effect of glass extracts on cell behaviour have helped to shape this work immensely.

To Dr. Ulrike Werner-Zwanziger, I cannot thank you enough for your efforts; both technical and intellectual, concerning the solid-state NMR. I have learned so much from you and your unique way of approaching research. It has been a privilege and an honour. Thank you!

To my fellow group members: Brett Dickey, Kathleen O'Connell, Lauren Kiri, Kathleen MacDonald, Dr Sharon Kehoe, Dr. Xiao Zhang, Susan Batchilder and Dr. Caitlin Pierlot, thank you for always being ready for a coffee break and an opportunity to get out of the office. Thank you for the stimulating discussions on any topic as well as feedback on my own work. Your ideas have always been extremely helpful and insightful.

To Dr. Patricia Comeau and Dr. Esther Valliant, thank you for sharing your very interesting ideas and more importantly thank you for your friendship.

For all their technical assistance and, more often than not moral support, I would like to Maxine Langman and Gordie Hall.

I must also thank Dr. Elena Tonkopi for her expertise and assistance obtaining and analyzing the radiopacity data. Robbie Sanderson, thank you for your assistance in collecting the X-Ray Diffraction data.

To my family, thank you for always putting up with my excuses of "sorry, I can't go because I am writing or have an experiment running". Your love, support and understanding have been a rock for me.

Finally, I would like to acknowledge the financial assistance of the BioMedic Create Program, Mitacs Accelerate, and NSERC.

Chapter 1: Introduction

Hepatocellular carcinoma (HCC) has the second highest cancer death rate worldwide [1] and is difficult to treat since *c.*80 % of cases are diagnosed at the intermediate or advanced stage, when curative treatments options are contraindicated [2-4]. Based on substantiating clinical evidence for lower complication rates and improved survivability, drug-eluting bead transarterial chemoembolization (DEB-TACE) has emerged as a preferred treatment option for patients with HCC in Europe and North America [5-7]. In a one step procedure, DEB-TACE deploys embolic particles loaded with a chemotherapeutic agent (typically doxorubicin (DOX)), resulting in simultaneous vessel occlusion and localized DOX release [8, 9], to infarct and locally treat the target tissue.

Presently, the available materials for DEB-TACE are limited by two major factors. Firstly, existing materials are radiolucent, limiting the direct imaging of the particles during and after the procedure [10, 11]. Consequently, the terminal locations of embolic particles cannot be ascertained, limiting our basic understanding of embolization biology whilst also preventing real-time patient-specific procedural optimization. Secondly, existing particles must be drug-loaded immediately prior to the procedure, which causes significant logistical issues between clinic and pharmacy [12, 13] and limits the shelf life of the loaded beads [14]. These two material limitations contribute significantly to the procedural variability that exists between interventional radiologists and institutions [13, 15]. As yet, no consensus over the type of embolic agent, chemotherapeutic agent, location of injection, or optimal end point has been achieved [13, 15]. Accordingly, there

is significant room to improve DEB-TACE procedures by providing embolic materials, which are both radiopaque and pre-loaded with a therapeutic agent.

With respect to radiopacity, Sharma *et al.* proposed that "image-able" (radiopaque) microspheres would provide intra-procedural feedback regarding the temporal and spatial distribution of microspheres; such information is required to personalize embolization treatments, and optimize localized chemotherapy delivery [11]. The inability to directly visualize embolic particles has contributed to significant procedural variability and has arguably limited the advancement toward personalized treatments in this field of medicine [11]. The ambiguous relationships between patient outcomes and the spatial distribution of both the chemotherapeutic and embolic agents have left physicians without a quantitative method to relate particle position to patient outcomes. Post procedurally, "image-able" microspheres would also provide the interventional radiologist with a critical tool for identifying the spatial relationship between embolic particles and tumor tissue; permitting the quantitative evaluation of embolization treatment efficacy while also providing critical information for planning subsequent procedures designed to target under-embolized tissues [15].

Many attempts to render embolic particles radiopaque have been predicated on the inclusion of a radiopacifying agent into conventional polymer-based embolization systems [11, 16, 17]. There has been limited success experimentally from an "image-ability" perspective and additionally, the effect of the radiopacifying agents on the drug delivery capability of these particles is unknown. Using an alternative design philosophy,

Kehoe *et al.* have developed a zinc-silicate based glass material that is inherently radiopaque for use in transarterial embolization (TAE) [18, 19]. Recent *in vivo* studies using a swine kidney model have demonstrated that this zinc-silicate system is visible under fluoroscopy, which provides for real-time clinical assessment of the temporal and spatial distribution of particles [20]. However, due to its high temperature synthesis, this glass cannot be pre-loaded with organic based chemotherapies during production and therefore does not address the second limitation of current DEB-TACE particles (i.e. the provision of preloaded particles for localized therapeutic release). To address this issue Kehoe et al. have developed a thermally induced phase separation method for incorporating the radiopaque glass into microspheres composed of polylactic-co-glycolic acid (PLGA) [21]. However these particles were too large to be used in DEB-TACE and the authors suggest that the low glass content may negatively impact radiopacity.

Building on the work of Kehoe *et al.* it may be possible to design "image-able" bioactive glasses that are also capable of releasing therapeutic inorganic ions (TIIs) designed to cause selective and localized tissue damage. The potential of bioactive glass networks to provide controlled release of TII has been long recognized and was recently summarized in two reviews by Lakhar *et al.* [22] and Hoppe *et al.* [23]. These reviews show that TIIs can modulate and/or improve osteogenesis, angiogenesis and inflammatory responses *in vivo* and *in vitro*. However, research with respect to bioactive glasses has been largely constrained and circumscribed by (i) the almost exclusive and ubiquitous development of bioactive glass systems for applications in bone repair and regeneration [24], and (ii) the

examination of material compositions constrained within the compositional palette of the original bioactive glass (invented in the 1960s), based on Na_2O-CaO-P_2O_5-SiO_2 [24].

Developing a glass for oncology applications requires an expansion of glass compositions that contain TIIs. Based on the fact that TIIs impact host-glass interactions, it may be possible to design bioactive glasses to deliver TIIs that trigger cytotoxic responses, which is counter to the conventional perceptions of 'biocompatibility' which are typically related to repair and regeneration [22, 23, 25]. Using this philosophical approach, a bioactive glass may be provided "drug-loaded", with a TII, rather than a traditional chemotherapeutic agent. Such an approach would eliminate the drug-loading step and extend the shelf life compared to the current materials, while simultaneously providing "image-able" embolic particles.

In order to understand the design of DEB-TACE systems, a fundamental understanding of HCC and current therapies is required. To this end, Chapter Two of this thesis will discuss the epidemiology and pathophysiology of HCC along with a brief overview of the risk factors for developing HCC and the current treatment strategies. Chapter Three will provide a description of the various TAE procedures and their efficacy. The relevant hepatic anatomy will be described, as it is critical to understanding TAE procedures. Chapter Three also provides a summary of the biomaterials used in DEB-TACE procedures as well as the emerging material design philosophies for TAE.

Chapter Four provides a comprehensive overview of the literature concerning the current models used to describe glass structure of systems and how these models relate to bioactive glass design. The purpose of this overview is to provide a basis for understanding the composition-structure-property-function relationships in bioactive glasses. The relevant literature concerning the use of bioactive glasses and their ability to trigger desired host responses is also discussed, and the evidence supporting the idea that controlled release of TIIs mediate powerful host responses will be emphasized. In the context of a cancer therapy, the evidence supporting particular TIIs with the potential to elicit cytotoxic responses in cancer cell lines will be presented.

Chapters Six, Seven, and Eight, standalone papers, are provided as they were published and/or submitted in their respective journals. Chapter Six: *Composition-property relationships for radiopaque composite materials: pre-loaded drug-eluting beads for transarterial chemoembolization* [26], is published in the Journal of Biomaterials Applications. This paper investigates the ability of polymer-glass composite embolic materials to provide for the appropriate levels of radiopacity as well as drug loading and delivery of DOX for use in DEB-TACE. The approach utilized in this paper follows a similar archetype as that currently used in the literature, where material/chemical additions are made to a base polymer in order to achieve the desired material characteristics through the combination of properties derived from the individual components. In this case, additions of glass particles and DOX are made to PLGA, which provides both radiopacity and therapeutic benefit to the embolic particles, respectively.

Chapter Seven: *Unanticipated stabilization of zinc-silicate glasses by addition of lanthanum: implications for therapeutic inorganic ion delivery systems*; under review in the Journal of Non-Crystalline Solids and Chapter Eight: *Stimulation of Apoptotic Pathways in Liver Cancer Cells: An Alternative Perspective on the Biocompatibility and Utility of Biomedical Glasses*; submitted for peer review, demonstrates a marked shift in the design philosophy for materials used in DEB-TACE procedures. This new and emerging philosophy seeks to simplify the design of biomaterials for DEB-TACE, such that it is the composition of the material itself that provides for both the desired radiopacity and the vectored delivery of an active therapeutic. Chapters Six through Eight provide discrete analysis on the limitations of each contribution. Chapter Nine provides a concluding discussion of the work as a whole, potential future research directions, as well as the broader implications of this work.

Chapter 2: Hepatocellular Carcinoma: Epidemiology, Pathophysiology, and Current Treatment Strategies

Hepatocellular carcinoma (HCC) is the sixth most common cancer worldwide; with approximately 782,000 new cases reported annually, it has the second highest cancer death rate of 746,000 patients per year [1]. Globally there is a clear difference in the incidence rates of HCC, with the highest number of cases occurring in China and sub-Saharan Africa (Figure 2.1) [27].

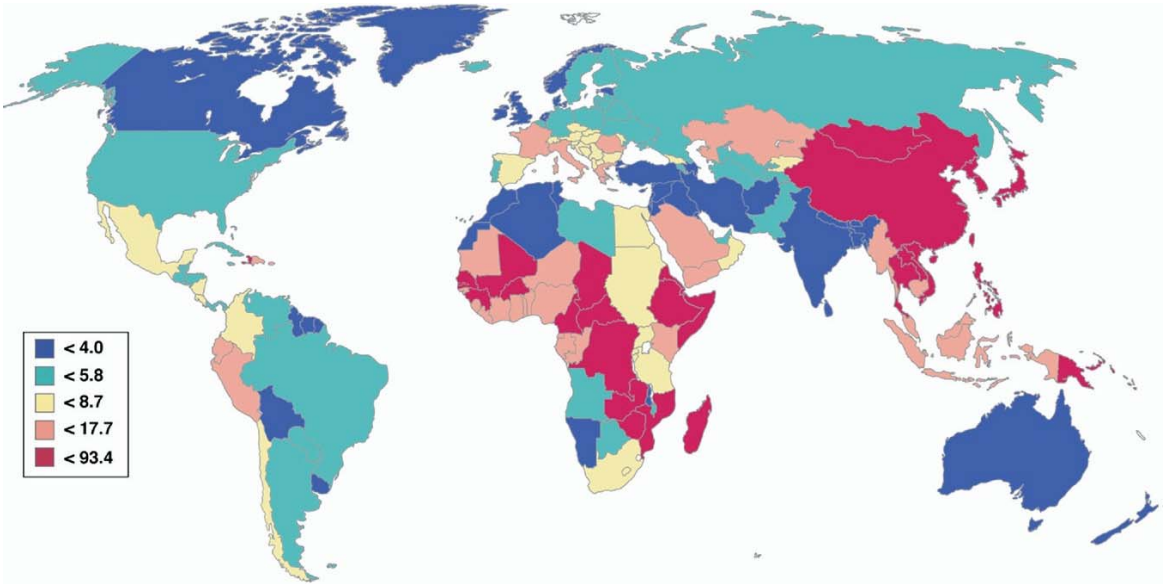

Figure 2.1: Global incidence of HCC per 100,000 people [27].

In the USA the incidence rate for HCC has increased steadily over the last four decades and it is expected to continue to rise at least until 2020 [28]; attributable to long-term chronic viral hepatitis infections prevalent in the aging baby boomer population. In addition, emerging evidence shows a significant increase in the relative risk of mortality due to liver cancer in obese men and women subsequent to nonalcoholic fatty liver

disease (NAFLD) [29]. Davis and Roberts suggest that NAFLD will become the most common cause of advanced liver disease in the USA due to the continued obesity epidemic [28], which is intimately connected to the increased rates of type II diabetes [30]. Within the literature it is difficult to determine if obesity or type II diabetes individually increase the risk of developing NAFLD since both often occur together. In a study of 173,643 healthy and 650,620 diabetic patients, El-Serag *et al.* determined that there was a higher incidence rate of NAFLD (18.13 cases per 10,000 people) in patients with diabetes compared to non-diabetics (9.55 cases per 10,000 people), and that there was also a higher incidence rate of HCC (2.39 cases per 10,000 people) in diabetic patients compared to non-diabetics (0.87 cases per 10,000 people)[31]. Due to the interrelated nature of HCC risk factors based on obesity, diabetes and NAFLD, El-Serag *et al.* postulate that the continued obesity epidemic in the USA will result in an overall increase in the number of HCC cases [27].

In addition to these drivers of HCC, significant numbers of liver tumors are caused by colorectal cancer (CRC) metastases. CRC is the third most common cancer worldwide and has the fourth highest death rate, with 1.3 million cases reported and 694,000 deaths reported each year, respectively [1]. Critically, 55 % of patients with CRC will develop metastases, primarily to the liver, during the course of the disease [32]. Two-thirds of patients with metastatic colorectal cancer (mCRC) die from liver failure as a direct result of complications resulting from these hepatic metastases [33].

In view of the epidemiology of HCC and the increasing number of cases of CRC and mCRC to the liver, it is important to note (in the context of this thesis) that liver directed therapies designed for use in HCC are also indicated for use in mCRC to the liver [34, 35].

2.1 Etiological Causes of HCC

There are two clear etiological causes of HCC: (i) chronic inflammation of the liver, and (ii) liver cirrhosis. The risk factors for HCC are intimately connected with its etiological factors and fall into two categories: (1) environmental and (2) host risk factors (Figure 2.2) [36]. In respect of the former, the environmental causes of HCC are associated with exposure to infectious diseases, toxins and a poor diet [36]. The two most prevalent infectious agents that correlate to HCC development are hepatitis B (HBV) and hepatitis C (HCV) viruses; associated with 52 % (HBV) and 20 % (HCV) of HCC cases worldwide, respectively [37]. Another major dietary factor is the consumption of alcohol. In Europe, approximately 72,000 HCC cases are reported each year that are attributed to alcohol abuse. Indeed, alcohol abuse has been associated with 10 % of liver disease cases, which leads to cirrhosis and/or HCC [36, 38].

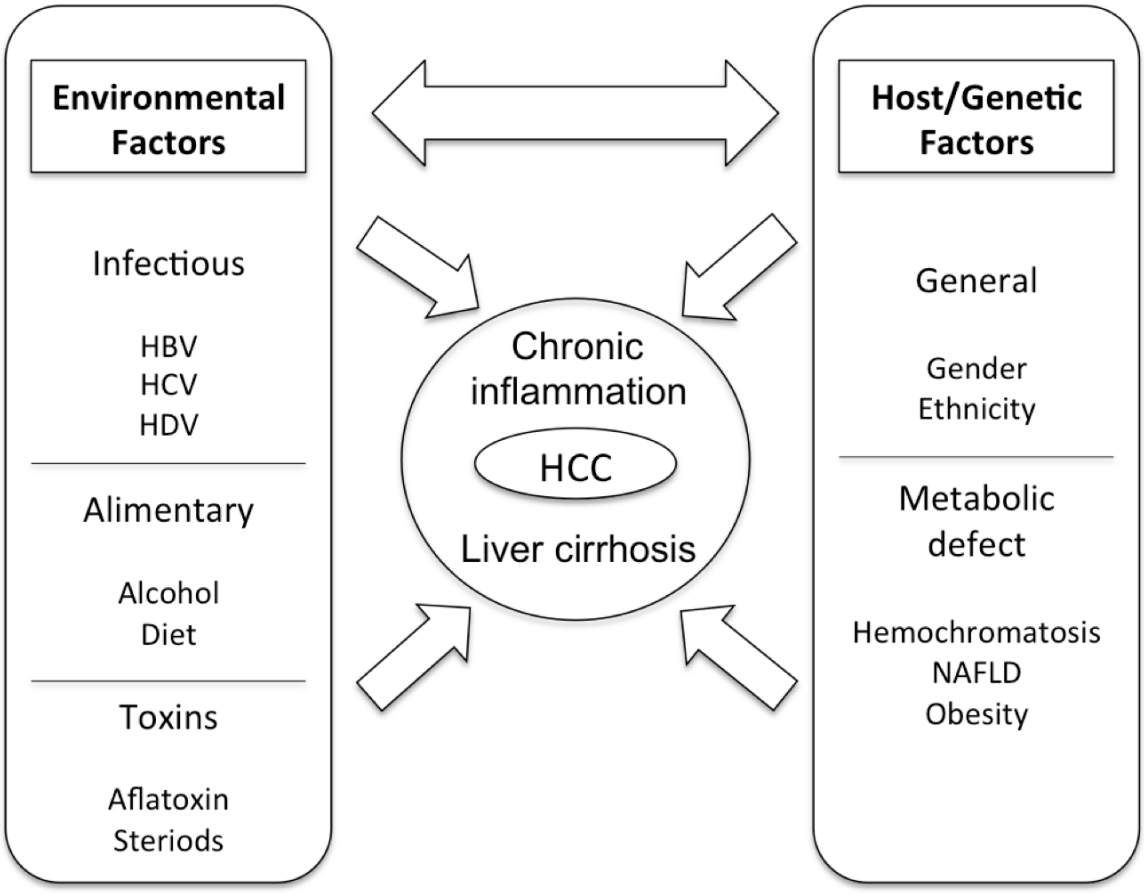

Figure 2.2: Schematic of risk factors for developing HCC, adapted from reference [36].

The major host factors that affect HCC development are (i) gender, (ii) ethnicity and (iii) NAFLD. Males typically have a 2:1 to 4:1 greater risk of developing HCC as compared to women [27]. People of Asian and Black descent are much more likely to develop HCC. In South East Asia high rates of HCC has been connected to the high prevalence of HBV and HCV infections [27, 36]. In Sub-Saharan Africa there is a high prevalence of aspergillus fungi species that grow on many of the staple foods. These fungi produce hepatotoxins; aflatoxins that have been connected to high rates of HCC [27, 36]. In the case of NAFLD, HCC risk assessments are complicated by the fact that NAFLD occurs

in a background of obesity and diabetes. In industrialized countries, there are approximately 134,000 reported cases of HCC each year [1] and it has been estimated that 30 to 40 % of these cases are a result of cirrhosis with no known causes [27]; however, new evidence is emerging and appears to show a correlation between NAFLD, obesity and type II diabetes with these cases of HCC from unknown cirrhosis [39].

2.2 Cellular Mechanism for HCC Development

The liver is a vital organ required for glucose and fat metabolism, synthesis of proteins and hormones, detoxification of the blood, and is pivotal in maintaining homeostasis [40-42]. Although there are many etiological factors that contribute to HCC across different populations, the pathophysiological process of HCC development eventually results in severe liver dysfunction in all patients, and ultimately impacts longevity and quality of life [43]. The subsequent paragraphs will detail the basic pathophysiology required to understand disease progression.

At a cellular level, the liver is composed of hepatocytes, which are the cells that perform the majority of the metabolic, secretory and endocrine functions of the liver and make up approximately 80 % of its volume [44, 45]. All of the aforementioned risk factors cause hepatocytes to be in a constant state of inflammation [46]. Accordingly, increased rates of cell proliferation occur to repair the damage, thereby increasing the likelihood of DNA mutations [36], a known mechanism for cancer initiation [47]. In some instances, the buildup of these mutations shuts down the biomolecular systems that initiate apoptosis, which allows the mutated cells to grow at an uncontrolled rate [47]. Based on these

cellular events, Thorgeirsson *et al.* propose a time line (Figure 2.3) for the formation of HCC neoplasia [46]. A primary insult occurs from infection or cirrhosis that initiates the preneoplasia phase, which can last 10 to 30 years. During this phase the rate of hepatocyte proliferation increases in response to the damage caused by the insult, which then leads to phenotypically altered cells. Over time, these altered cells become dysplastic hepatocytes and enter the dysplasia phase, lasting three to five years. These dysplastic hepatocytes become an *in situ* neoplasm and result in the formation of a HCC tumor. Crucially, these neoplastic cells have common features: self-sufficiency in growth signals, insensitivity to anti-growth signals, tissue invasion and metastatic potential, sustained angiogenesis, evasion from immune surveillance, limitless replication potential, and evasion of apoptosis [48]. It is thought that HCC initially starts as a small discrete nodule with the potential to either grow into a large single nodule (tumor) or invade other parts of the liver.

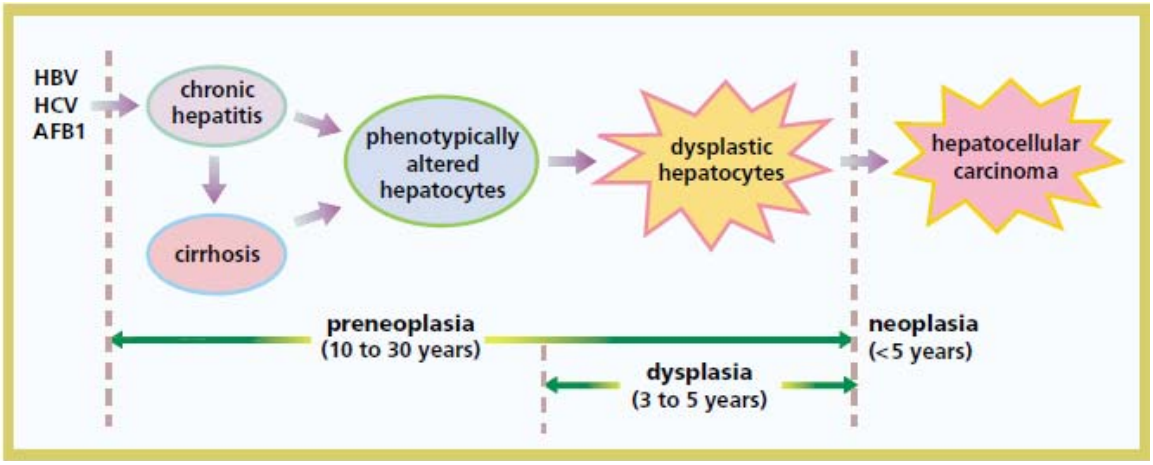

Figure 2.3: Timeline for progression of chronic liver inflammation to HCC [46].

Tumors can have well defined discrete nodules, can be large with satellite nodules, or may be poorly defined with many small nodules dispersed throughout the liver [44]. As malignant hepatocytes continue to invade the liver tissue, liver function becomes significantly impaired, ultimately resulting in loss of function. Moving forward from the epidemiology and pathophysiology of HCC and in order to develop an effective novel biomaterial based therapy for HCC, it is important to understand the factors that impact patient outcomes.

2.3 Tumor Staging and Overview of Current Therapies

Factors that impact the survival rate of patients with HCC include; liver function, tumor size, tumor shape, level of spreading, and the nature of portal vein involvement [49]. Liver function is assessed using the internationally accepted Child-Pugh system, which is based on (1) degree of ascites[1], (2) level of encephalopathy, (3) concentrations of bilirubin, (4) plasma albumin and (5) prothrombin time [50]. This approach places patients into one of three stages; A, B, or C, (Figure 2.4) [51]. Based on the stage of the disease as described by the Barcelona Clinic Liver Cancer (BCLC) staging system (Figure 2.4), patients are matched with the appropriate therapy [52].

[1] Accumulation of fluid in the peritoneal cavity, which causes abdominal swelling [50]

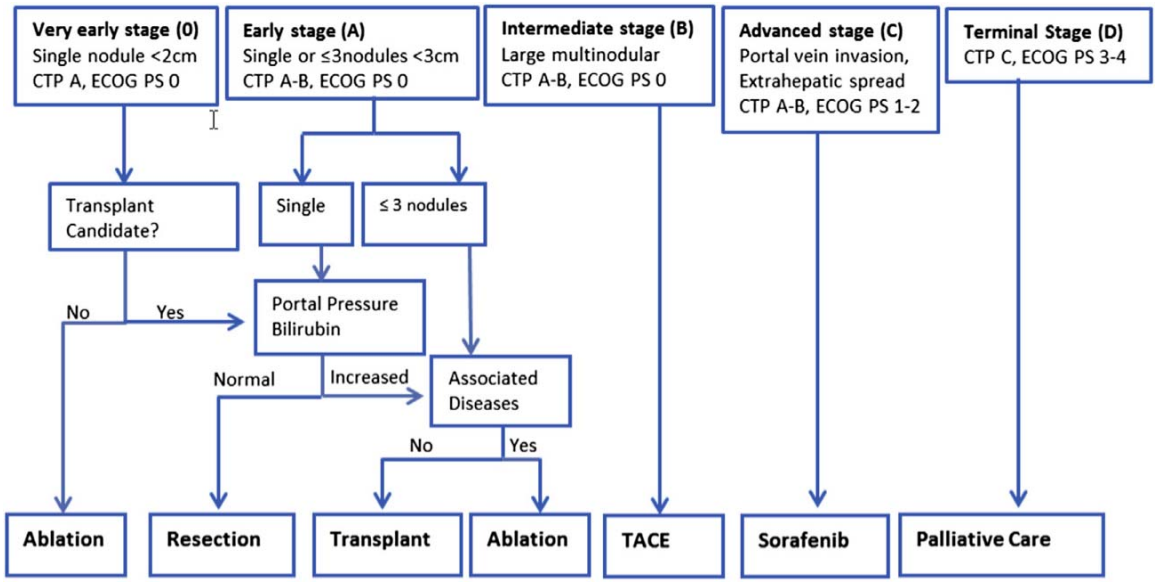

Figure 2.4: Staging of HCC and treatment options available [52].

Llovet and Bruix summarized the survival rates for different stages of HCC [53]. Patients diagnosed with early stage HCC had a five-year survival rate of 50 to 70 % [53]. However, the majority of patients with HCC were diagnosed at the intermediate to advanced stage of the disease [54, 55], and while mortality varies depending on sub-classification, the aggregate two-year survival rate is reported to be between 8 % to 50 % [56]. Regrettably, patients presenting with end-stage HCC have a median survival rate of three to four months [53], with a five year survival rate of 10 % [53]. For these patients, treatments are designed to manage and mitigate the morbidity associated with the symptoms of liver failure [52].

The treatment options for patients with HCC can be broken into two major groups: *curative* and *non-curative* [49]. Within the *curative* group, the treatment options are (i) complete liver transplant, (ii) hepatic resection or (iii) ablation. The 5-year survival rate

for resection patients is 70 %. The evidence for transplant patients shows a survival rate at four years of between 75-83 %. Finally, the 3-year survival rate for ablation patients is 62-78 % [57]. The introduction of surveillance programs for high-risk populations has resulted in more individuals receiving curative treatments, since HCC is detected at an early stage when these treatments are an option [49, 52]. Sadly, even with better surveillance programs, up to 60 % of HCC cases are diagnosed after curative treatments are no longer an option [54, 55].

In the early stages of the disease, the liver compensates for loss of function by hepatocyte growth, which typically causes HCC to remain asymptomatic until symptoms of liver failure are apparent [58]. The increased growth of hepatocytes allows critical functions to be maintained even with high tumor loads, which is why the majority of patients only qualify for non-curative, palliative therapies at the time of diagnosis. Within the *non-curative* group of therapies there are three subgroups: (i) symptomatic therapies, (ii) systemic therapeutic agents and (iii) transarterial chemoembolization (TACE). Although not shown in Figure 2.4, transarterial radioembolization (TARE) is emerging as an important therapy for advanced HCC. Symptomatic therapies are designed to ease the pain and suffering of patients with end stage HCC and include opioids, acetaminophen and corticosteroids with morphine recommended as a first line therapy [59]. Traditional systemic chemotherapy is associated with significant systemic toxicity and does not increase survival time for patients with advanced HCC [60, 61]. Currently, the only approved systemic chemotherapy with proven survival benefits in patients with advanced HCC is sorafenib tosylate, which is an angiogenesis kinase inhibitor and has been shown

to increase the median survival time in advanced HCC from 7.9 months in placebo treated patients to 10.7 months [62].

The traditional paradigm for treating cancer with chemotherapy is to systemically deliver high concentrations of one of the five major classes of cancer therapies: alkylating agents, antimetabolites, anthracyclines, plant alkaloids and topoisomerase inhibitors. Alkylating agents are antineoplastic compounds that alkylate/methylate amino acid residues within DNA strands. Temozolomide, an alkylating agent used for treating brain cancers, binds preferentially to and methylates atoms N7 on guanine, O6 on guanine and O3 on adenine [63]. It has long been recognized that the severe side effects caused by first generation alklylating agents were due to the irreversible non-selective binding to nucleophilic sites on biological compounds [64]. Antimetabolites interfere with cellular metabolic pathways. Since the metabolic rate of cancer cells is higher than normal tissues, antimetabolites cause greater damage to cancer cells. Capecitabine is an antimetabolite and when used in conjunction with thalidomide may increase the survival rate of patients with advanced HCC [65]. The anticancer action of capecitabine occurs by two routes: 1) the prevention of thymidine synthesis, which is critical for DNA synthesis and 2) insertion of a false base in RNA, which also inhibits DNA synthesis [66]. Anthracyclines prevent DNA synthesis by binding to DNA chains as well as unfolding DNA strands. Anthracyclines also produce free radicals that damage both the DNA and the cell walls. The most successful of this class is doxorubicin, which is used to treat HCC [67]. Plant alkaloids are compounds derived from plants that prevent cell division by inhibiting microtubules from depolymerizing during cell replication. Taxol, a plant alkaloid, is used

to treat a variety of malignancies including lung, ovarian, gastric and many others [68]. Topoisomerase inhibitors interfere with the topoisomerase enzymes. These enzymes promote the breaking and rejoining of the phosphate backbone of DNA during normal cell functions. Topoisomerase inhibitors are thought to prevent the rejoining of DNA fragments, which subsequently causes the cells to undergo apoptosis. Irinotecan is a topoisomerase inhibitor that has been used to treat HCC [69].

However, the complications of systemic chemotherapy include significant weight loss, ulcers, diarrhea and increased risk of infection. The impact of chemotherapy on bone marrow can cause anemia, increased risk of bleeding and weakened immune system, hair loss, as well as loss of fertility in both males and females [70]. The high morbidity associated with systemic chemotherapy treatments has led to development of localized and targeted drug delivery systems designed for HCC therapy. In patients with intermediate-advanced stage HCC TARE, a loco-regional therapy, has demonstrated similar survival benefits as sorafenib [71] and also has the potential to cause tumor down staging [72].

Chapter 3: Transarterial Embolization Procedures for HCC and mCRC

As mentioned, TAE therapies (palliative treatments) are the current standard of care for patients with intermediate and advanced HCC as they provide localized delivery of therapeutic agents and minimize side effects. Briefly, and at the most fundamental level, a TAE procedure involves the selective occlusion of blood vessels supplying a tumor with embolic particles, leading to infarction of the tumor [8]. Particle embolization procedures can be categorized as: (1) TAE, where only particles are used for therapy; (2) TACE, which uses a combination of directed chemotherapy and embolization; and (3) transarterial radio-embolization (TARE), which uses selective internal radiation therapy.

In order to understand the basis of TAE treatments for liver tumors, it is critical to first understand the vascular anatomy of the liver. Located in the upper right quadrant of the abdominal cavity and below the diaphragm, the liver is a unique organ which receives blood from *both* the hepatic artery and the portal vein (Figure 3.1) [73]. The hepatic artery carries oxygenated blood from the heart, while the portal vein carries nutrient rich deoxygenated blood from the gastrointestinal tract [74]. Normal liver tissue receives 75 % of its required blood supply from the portal vein and only 25 % from the hepatic artery [75]. Strikingly, HCC tumors receive *c.*95% of their blood supply from the hepatic arterial system and this fact makes embolization treatments possible, since the tumor can be occluded without causing significant damage to surrounding non-cancerous liver tissue [75].

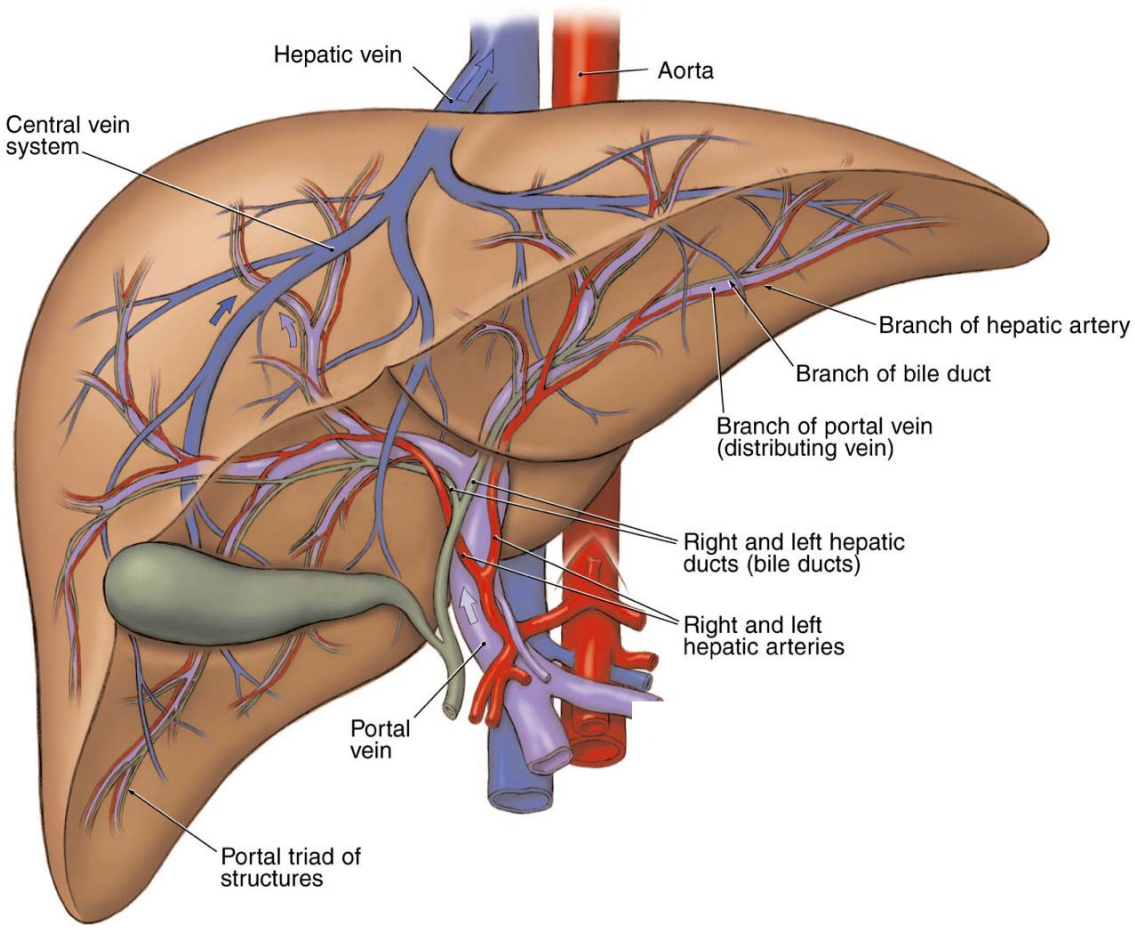

Figure 3.1: Vascular anatomy of the liver adapted from [73].

Generally, all TAE procedures share similar technical and methodological characteristics [76]. Under fluoroscopic guidance, a catheter is inserted percutaneously into the femoral artery and guided into the hepatic artery. The vasculature is imaged and assessed using fluoroscopy and/or cone beam CT after intra-arterial injection of non-ionic contrast media (e.g. Isovue) in order to identify the vessels perfusing the tumor (Figure 3.2(a))[77]. Embolic particles, suspended in a mixture of non-ionic contrast media and saline, are delivered through the catheter [78]. The particles flow with the blood stream towards the tumor, and become lodged in targeted vessels causing occlusion. Visually,

this causes the blood vessels distal to the point of occlusion to “disappear” since the contrast media can no longer penetrate into these vessels (Figure 3.2(b)) [77].

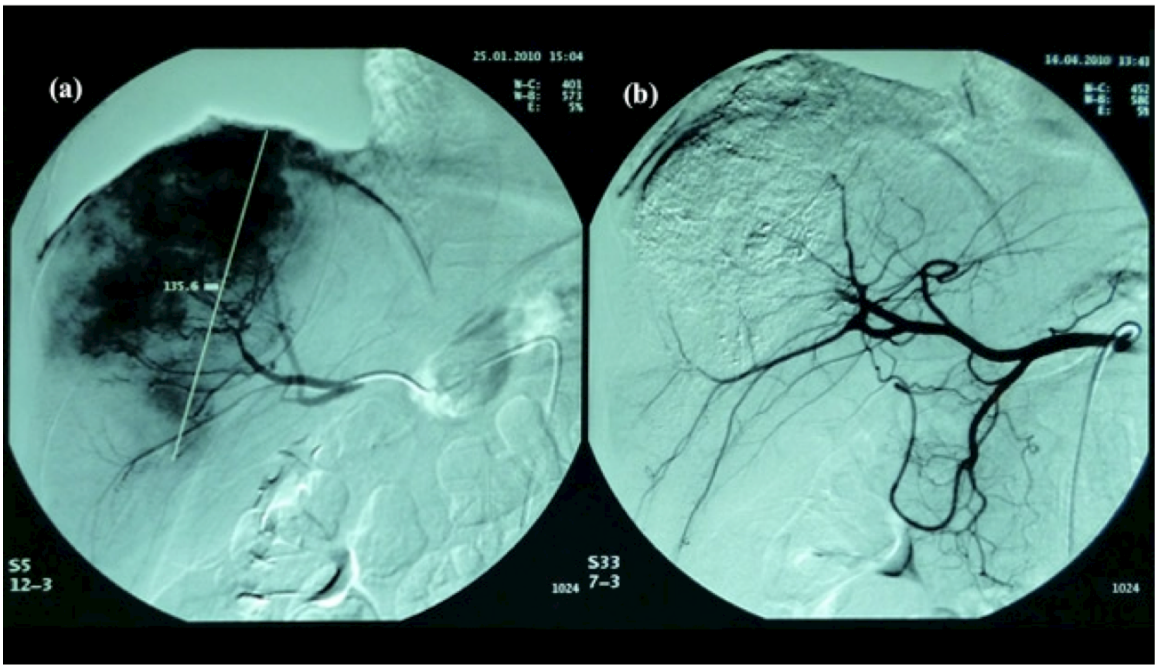

Figure 3.2: Representation of an embolization procedure for HCC treatment. (a) Identification of vessels perfusing the tumor and (b) post embolization image [77].

Prior to DEB-TACE, conventional TACE (cTACE) was the standard of care. In a cTACE procedure a chemotherapeutic agent mixed with lipiodol is delivered through the catheter and followed immediately by an embolic agent. The purpose of the embolization step is to increase tumor exposure time by preventing wash out of the chemotherapy (e.g., which is typically DOX). However, it is well known that lipiodol and chemotherapeutics do not provide for stable homogenous admixtures resulting in separation of the emulsions [79]. Significant increases in systemic levels of chemotherapeutic agents in patients receiving cTACE are also observed [80], which indicates that tumors are exposed to an unknown

amount of drug for an unknown amount of time with this approach. To increase the tumor-drug exposure time and reduce the systemic levels of chemotherapy DEB-TACE was developed. A DEB-TACE procedure is performed similarly to cTACE. However, the embolic agent is drug-loaded just prior to the procedure in DEB-TACE and provides for sustained local release at the embolic site, which will be described in more detail in subsequent sections. Based on substantiating clinical evidence for lower complication rates and improved survivability verses cTACE, DEB-TACE has emerged as the preferred treatment option for patients with intermediate HCC [5-7]. Only DEB-TACE and TARE provide vectored delivery of a therapeutic agent from the embolic particle.

TARE deploys embolic particles containing a radioactive beta emitter, yittrium 90 (^{90}Y), and provides for simultaneous embolization and localized delivery of radiation therapy [81]. The embolic agent is < 45 μm, which modifies the risk profile compared to DEB-TACE (conventionally performed using particles in the size range of 75-300 μm). In particular, there is a greater risk of portal vein shunting that can result in particle deposition and subsequent radiation exposure to non-target tissues [82]. These issues have been indicated as a cause of deaths in a number of patients undergoing TARE [83]. To prevent this and to predict the effective radiation dose in the target tissue and other organs, pretreatment angiography and imaging using technetium-99 macroaggregated albumin (Tc99-MAA) is performed. In this procedure, the hepatic artery is selectively catheterized, followed by coil embolization of hepatic arterial branches that vascularize other organs. Tc99-MAA is then injected and whole body single photon emission CT scan is performed to identify the Tc99-MAA distribution in the gastrointestinal tract and

lungs [84]. Should the calculated extra hepatic radiation dose be too high (in particular more than 30 Gy in the lungs), then TARE is contraindicated [85]. It has been shown in the literature that TARE is more effective, has lower clinical toxicities, greater tumour response and reduced adverse events when compared to patients receiving cTACE therapy [86]. Currently there is only one study available that directly compares DEB-TACE to TARE procedures, which showed no significant differences for progression free survival, overall survival and time to progression [87]. However due to the small size of this study (24 patients) the authors indicate that a much larger cohort will be needed to properly compare the two therapies [87]. Presently, there are conflicting views on the role of TARE for HCC therapy. Boily *et al.* recommended that TARE be considered in the context of clinical trials and not yet as a standard of care [88]. Contrastingly, Pitton et al indicated that TARE is considered as a second line treatment and suggest that TARE could become a first line therapy [87]. However, selective internal radiation therapy provided by TARE falls under the scope of nuclear medicine, not a chemically-based therapy, and as such is philosophically and scientifically beyond the scope of this thesis.

3.1 Materials for DEB-TACE

In an attempt to increase tumor-drug exposure time DEB-TACE was developed. In a one step procedure these particles provide for both occlusion of the tumor and concurrent localized drug delivery. In DEB-TACE procedures embolic particles are drug-loaded just prior to the embolization and slowly release their chemotherapy payload once the tumor's blood vessels have been occluded and in this way increases the tumor-drug exposure time.

Currently there are two clinically utilized materials for DEB-TACE and both are composed of modified polyvinyl alcohol (PVA). Unlike most vinyl polymers, PVA $(-CH_2CHOH-)_{n,,}$ cannot be directly synthesized from its monomer, vinyl alcohol ($H_2C=CHOH$). This is due to the tautomerization of the alcohol to acetaldehyde ($H_3C-CH=O$) [89]. Therefore to produce PVA, the precursor polymer, polyvinyl acetate (PVAc) $(-CH_2CHCOOCH_3-)_n$, is synthesized from the monomer, vinyl acetate (VAc, $H_2C=CHCOOCH_3$), via free radical polymerization [90]. PVAc is subsequently converted to PVA by saponification: hydrolysis of the acetate pendent group on the PVAc monomer unit [91].

The most studied of the clinically utilized materials is sulfonated PVA (s-PVA) hydrogel combined with DOX or irinotican (IRI). s-PVA, clinically available as DC Bead® or LC Bead® [92], is composed of PVA that has been modified to contain sulfonate groups by inverse suspension free-radical polymerization [93]. To enable drug loading PVA is first modified with N-acryloyl-aminoacetaldehyde dimethylacetal (NAAADA) so that a portion of the OH groups on the PVA macromolecule are replaced by NAAADA [94]. Figure 3.3 is a schematic representation of the inverse suspension free-radical polymerization [93]. A suspension of an aqueous solution containing potassium persulfate, 2-acrylamido-2-methylpropanesulfonate sodium salt (AMPS) and the NAAADA modified PVA is produced in an organic solution of butyl acetate and cellulose acetate butyrate. The suspension is then heated to 60 °C, at which point tetramethylethylenediamine (TMEDA) is added to the organic phase. Potassium

persulfate and TMEDA combine to initiate free-radical polymerization, which produces an insoluble cross-linked hydrogel composed of a s-PVA network [93]. s-PVA hydrogel microspheres are composed of approximately 90-95 % water by weight [95], which allows for up to 30 % compression during passage through a microcatheter [13].

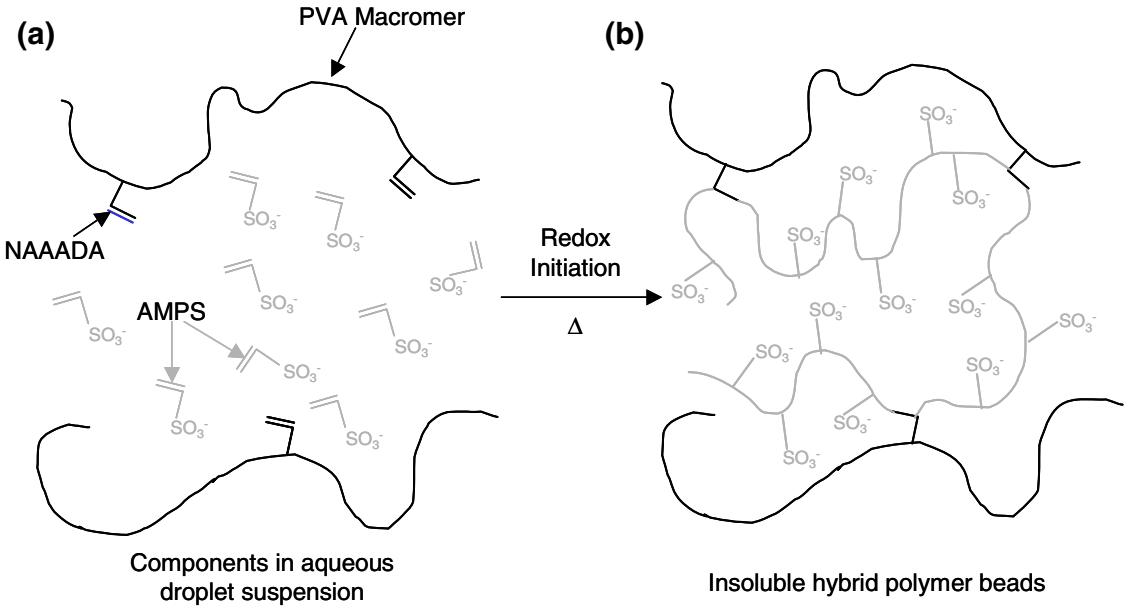

Figure 3.3: Schematic of s-PVA synthesis: (a) composition of aqueous suspension and (b) cross-linked s-PVA hydrogel [93].

Super absorbent particles (SAP) based on sodium acrylate/vinyl alcohol copolymer represent the existing clinical alternative to s-PVA [96]. SAPs were originally developed by Jiaqi *et al.* in 1996 [97] and are currently used under the trade name HepaSphere™. The two monomers used to synthesize the SAP particles are vinyl VAc and methyl acrylate (MA, H_2C=CH-$COOCH_3$). As mentioned previously VAc is used as a precursor monomer since vinyl alcohol monomers tautomerize easily [89]. Using free radical suspension polymerization methodology, the VAc and MA monomers are copolymerized

to produce microspheres containing both monomer units in the backbone. This copolymer is subsequently processed to convert the monomer functional groups to the following: acetate is replaced by an alcohol group and the methacrylate to a sodium acrylate group [97]. The particles are superabsorbent since they swell to four times greater than their original dehydrated state within 10 minutes [98].

3.2 Mechanism of Loading for Vectored Delivery

Drug loading of both s-PVA and SAP microspheres is facilitated by the inclusion of negatively charged moieties within their respective polymer backbones. The sulfate component of the s-PVA and the acrylate functional group of SAP carry a negative charge, which facilitates loading of positively charged drugs [99-101]. Microspheres are loaded with DOX when treating HCC and are loaded with IRI when treating mCRC [100]. A schematic describing the interaction of s-PVA sulfonate groups with DOX and IRI is shown in Figure 3.4 [100]. A similar interaction occurs in SAP microspheres but with the acrylate group rather than the sulfonate group [101].

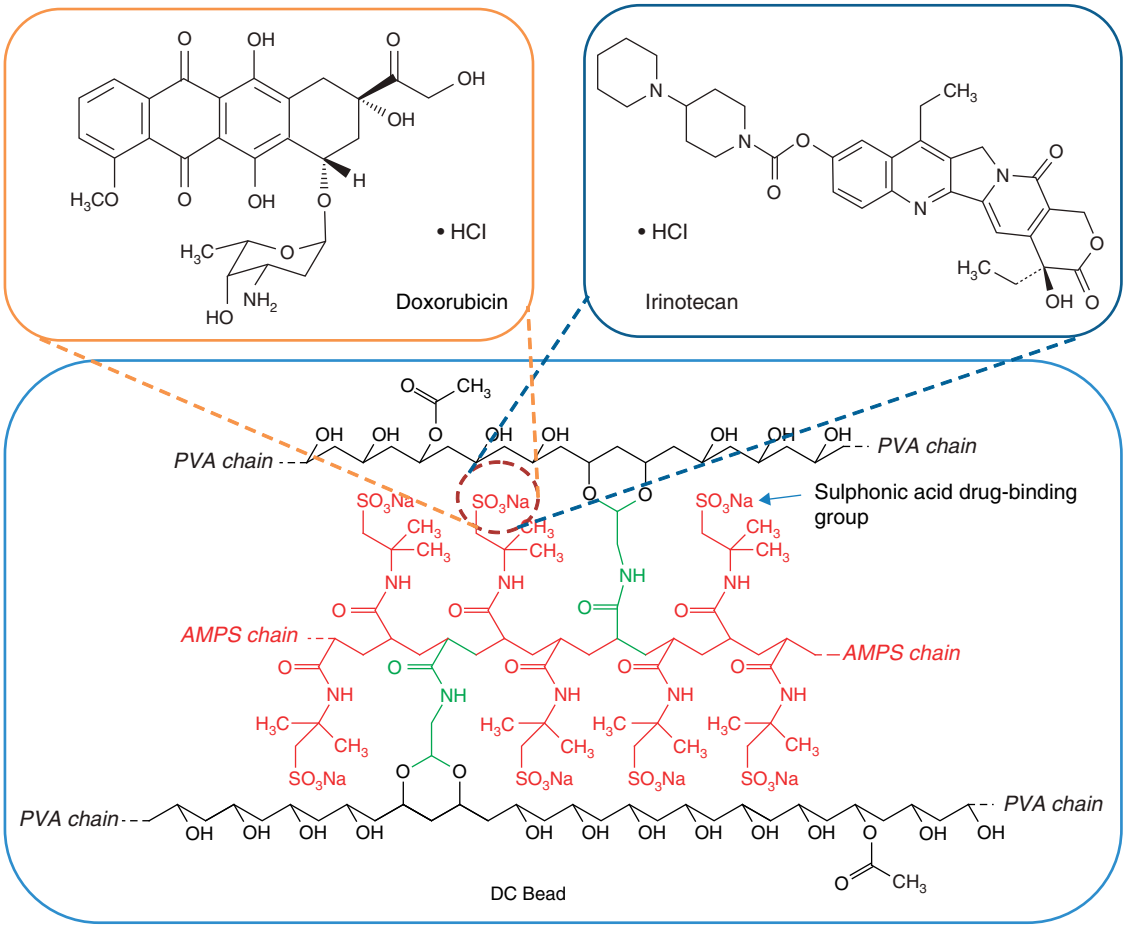

Figure 3.4: Drug loading schematic of s-PVA with DOX and IRI [100]

3.2.1 Practical Considerations for Drug Loading

Currently none of the clinically available embolic agents are provided with the therapeutic drug pre-loaded. This means that existing particles must be drug-loaded immediately prior to a procedure, requiring significant logistical coordination between the pharmacy and the interventional oncology team to ensure proper drug loading [12, 13, 102]. Since DOX loading into the clinically available embolic agents is the most studied drug it will be used as an example of the loading method. It is important to note that other positively charged drugs can also be loaded in a similar fashion [102, 103].

s-PVA microspheres are loaded following a four step procedure, which is outlined in the instructions for use [104]: (i) A DOX solution with the appropriate concentration is prepared (in the supplied vial) by mixing with sterile water, (ii) in a separate vial, “as much saline as possible” is removed from the s-PVA microspheres, which are supplied pre-hydrated, (iii) using sterile technique, the DOX solution is added to the pre-hydrated microspheres, (iv) the microsphere and DOX mixture is then agitated “occasionally” for 20 to 120 minutes, until the microspheres become red [104]. The loading efficiency of DOX is both time and particle size dependent. To achieve ≥ 99 % loading efficiency for all particle sizes 2 mL of s-PVA beads require 2 hours of exposure to a 25 mg/mL DOX solution [13, 104]. Once loaded the microspheres have a limited shelf life of four hours at room temperature and up 24 hours if refrigerated with or without non-ionic contrast media [14].

The loading process for SAP microspheres, as described in the instructions for use [105], is very different from s-PVA since they are provided dry. 20 mL of a DOX solution with a maximum concentration of 5 mg/mL is prepared using 0.9 % NaCl. This solution is transferred to two separate syringes, 10 mL in each syringe. 10 mL of the DOX solution is added to the dry SAP microsphere vial while it is held horizontally and simultaneously rolled. This is to ensure complete hydration of the microspheres. Once the DOX solution is added, the vial is placed in the vertical position and shaken every 2-3 minutes until a total of 10 minutes has passed. The entire contents of this vial are then transferred into the second syringe with the remaining 10 mL of DOX solution. The syringe is inverted

every 10-15 minutes for a minimum of 60 minutes to ensure SAP microspheres are homogenously exposed to the DOX solution. The supernatant is subsequently removed and replaced with non-ionic contrast medium prior to the embolization procedure. As in the s-PVA microspheres, the loading efficiency of DOX into SAP microspheres is time and particle size dependent. The loading efficiency can reach 82-94 % after an hour exposure to a 3.75 mg/mL DOX solution [12, 105]. The drug-loaded microspheres can be used for up to 24 hours if stored between 2-8 °C. However, if exposed to non-ionic contrast media the microspheres must be used immediately [105].

It is clear that drug loading into s-PVA or SAP is a time consuming and technically demanding process that must be properly coordinated with the hospital pharmacy in order to provide the optimum therapy. If done incorrectly the desired therapeutic levels may not be provided to the patient. The limited shelf life of the particles, once loaded, provides a small window to utilize these particles and unforeseen delays may result in wasted material. Also, it has been demonstrated that drug loading can cause fragmentation and microsphere delamination, which ultimately leads to particle aggregation and poor deliverability characteristics [101].

It is also important to note that drug loading in this manner causes significant changes to the physical properties of the microspheres. In an *in vitro* study, Jordan *et al.* evaluated the effect of DOX and IRI loading into s-PVA and SAP microspheres on the microsphere size and elastic modulus. DOX loading in s-PVA and SAP caused microsphere shrinkage of 20 % and 10 %, respectively [106]. IRI loading caused microsphere shrinkage of 34 %

(s-PVA) and 23 % (SAP) [106]. The elastic modulus of s-PVA increased from 5.5 kPa to 7.3 kPa for IRI and 15.3 kPa for DOX while the SAP modulus increased from 1.6 kPa to 2.9 kPa for IRI and 11.5 kPa for DOX [106]. Lewis *et al.* attribute these changes to the physical properties to the displacement of water during drug loading (related to the ionic binding strength of the drug to the polymer) [13]. Upon release of the therapeutic agent it is uncertain if the physical properties of the particles will return to their original state since these values were not reported [106]. This lack of understanding concerning the physical properties of embolic particles *in vivo* may be a contributing factor to poor clinical outcomes. To improve, optimize and standardize DEB-TACE procedures it is imperative that methods be established to evaluate particle behavior *in vivo*.

3.2.2 Evaluation of Vectored Delivery

Currently patients are administered a maximum of 150 mg of DOX per DEB-TACE treatment [107] and can receive a maximum of 450 mg/m^2 (body surface area) of DOX over a lifetime [108]. These values are based on a study by Lefrak *et al.* where systemically administered DOX caused cardiotoxicity and death in patients receiving DOX doses above 500 mg/m^2 [109]. The optimum dose required for a DEB-TACE procedure has not been specifically determined and it is unclear if the values determined for systemic therapy are appropriate for a vectored delivery system.

In order to improve vectored delivery from DEB-TACE systems it is important to understand the behavior of the current systems. Lewis *et al.* evaluated the *in vitro* drug release properties of DOX from s-PVA microspheres and showed that the 700-900 μm

sized particles released only 10 % of the loaded drug while the 100-300 μm sized particles released 20 % of the loaded drug [13]. In a subsequent study, Gonzalez *et al.* demonstrated that increasing the ionic strength of the elution media increased DOX release allowing 36 % of the loaded DOX to be released after 25 days in 9 % saline solution [110]. Both of these studies show that drug release is particle size dependent where smaller particles release greater amounts of the loaded drug [13, 110]. *In vitro* data for DOX-loaded SAP microspheres shows that maximum release of DOX occurs after 5-7 days [101], which is shorter than the maximum release from s-PVA microspheres, which occurred at 10 days [110]. Kos *et al.* demonstrated that in SAP microspheres up to 40 % of the loaded DOX can be released into 0.9 % saline solution [111], which is a much lower ionic strength solution than that used by Gonzalez *et al.* [110]. Since both materials (s-PVA and SAP) bind DOX through an ion exchange mechanism and drug release appears to depend on the ionic strength of the solution this suggests that DOX binding to s-PVA is stronger than SAP microspheres.

In vivo DOX release s-PVA was studied over 90 days in a swine model [112]. Nearly 90 % of the total DOX load was released after 90 days and penetrated into the tissue up to 600 μm from the bead edge. Smaller particles, 100-300 μm, caused greater cytotoxic effect than the 700-900 μm size range and in all cases the DOX concentration was at cytotoxic levels [112]. In explanted human livers, Namur *et al.* showed that 100-300 μm s-PVA microspheres blocked vessels with a mean diameter of 237 μm and that a single microsphere occluded a single vessel [113]. This indicates that the s-PVA microspheres do not form aggregates *in vivo*, which has previously been attributed to recanalization of

vessels and embolization failure [114]. Namur *et al.* verified that the DOX released from s-PVA particles was above the cytotoxic threshold for all time points measured, 5 μM at 8 hours post embolization and at one month 0.65 μM and that DOX penetration up to 1.2 mm into the tissue indicating appropriate chemotherapy delivery [113]. SAP microspheres have also been shown to provide sustained release of DOX *in vivo*. In a rabbit VX2 tumor model comparing DOX-loaded SAP microspheres to cTACE using trisacryl gelatin microspheres, the peak plasma DOX concentration was lower in the SAP group, indicating increased intratumoral retention compared to cTACE [115]. As expected the SAP group had the highest intratumoral DOX concentration, which penetrated up to 1.6 mm from the microsphere edge [115]. Gupta *et al.* showed in a rabbit liver model that the maximum DOX release into a VX2 tumor occurred by 3 days for SAP microspheres [115], which is much shorter than the 28 days observed for s-PVA [113]. In a clinical study comparing SAP microspheres to cTACE, Malagari *et al.* showed that the maximum DOX plasma concentration is dramatically reduced in the SAP group (84 ng/mL vs 761 ng/mL) [116] and had a similar reduction in DOX plasma concentration for s-PVA microspheres (79 ng/mL vs 895 ng/mL) [80]. This indicates that both s-PVA and SAP microspheres provide for controlled release of DOX. Combining the pre-clinical with the clinical data suggest that the both s-PVA and SAP microspheres reduce the peak concentration of DOX; however, the extended release of DOX from s-PVA make them for better long-term drug delivery. Since it is clear that DEB-TACE procedures reduce systemic DOX concentrations, it may be possible to increase the total amount of DOX a patient receives without the risk of cardiotoxicity. However, dosing has not been determined specifically for DEB-TACE procedures.

3.2.3 Clinical Efficacy of DEB-TACE

In a short term, one year, prospective randomized clinical trial the response of patients treated with DOX-loaded microparticles verses patients treated by embolization alone was studied by Malagari *et al.*; they showed that the 'time to progression' was longer in the DEB-TACE group [117]. In this same study no difference in the number of complications or severity of complications was observed between DEB-TACE and embolization alone, an improvement compared to cTACE procedures, which have a higher incidence and severity of adverse events [6]. The PRECISION V study was an international, multicenter prospective randomized clinical trial including 212 patients and was designed to establish if a clinical difference exists between DEB-TACE and cTACE procedures. DEB-TACE was compared to cTACE in both intermediate and advanced HCC. DEB-TACE treated patients showed higher response rates than the cTACE group [6]. The authors report that there was a significant reduction in the severity of liver toxicity and side effects of DOX in the DEB-TACE group even though those patients received a higher dose of DOX [6]. This may be a direct result of reduced DOX plasma concentrations for patients receiving DEB-TACE [80]. Meza-Junco *et al.* state that the improvement of DEB-TACE over cTACE for patients with more advanced disease is a major factor in changing the standard of care for intermediate HCC to DEB-TACE [118]. In a study of 129 patients receiving DEB-TACE or cTACE, Song *et al.* again showed that DEB-TACE had better treatment response rates, and the time to progression without compromising the rate of adverse events [119]. Two recent reviews of the clinical data comparing DEB-TACE and cTACE both conclude that DEB-TACE is a better treatment

option due to the reduction in side effects, increased objective tumor response and increased overall survival at one and two years post therapy [120, 121]. It is clear from the clinical data that the targeted delivery and controlled release of chemotherapy from drug eluding beads improves TACE therapy.

3.3 Personalization of Embolization Procedures

Independent of the type of TAE procedure significant procedural variability exists between interventional radiologists and institutions. As yet, no consensus over the type of embolic agent, location of injection or optimal end point has been achieved [13, 15]. This lack of consensus is due, in part, to the fact that all embolic particles used in TAE procedures today cannot be visualized during and after the procedure [11]. Existing embolic particles are radiolucent, and therefore their spatial and temporal distribution may only be inferred based on a cessation of blood flow, which is also inferred based on the flow of contrast media. All information concerning particle location relies on the assumption that the location of contrast media is an accurate surrogate measure for particle location. However, Sharma *et al.* demonstrated that this is not the case in swine liver and kidney systems and that contrast media location does not reflect the terminal location of embolic particles [11]. In the context of DEB-TACE procedures, the lack of knowledge concerning particle location also causes uncertainty concerning the local concentration of chemotherapy and may therefore result in inappropriate dosing of tumor tissue. The inability to directly visualize embolic particles both intra- and post-procedurally has contributed to the ongoing procedural variability that has arguably

limited the advancement of TAE procedures toward personalized treatments for patients [11].

Another source of uncertainty in particle location is due to the high degree of deformation many of these particles experience during a procedure. Bilbao *et al.* compared four commercially available embolic materials in a swine kidney model and showed that both nominal particle size and deformation played a role in the final location of embolic particles in the target tissue [122]. Increased particle deformation, which was dependent on the embolic agent used, caused more distal embolization than the nominal size predicted. It has been hypothesized that deformability is a desired property since it facilitates particle delivery through a microcatheter [123]. However, in a randomized clinical study comparing two clinically available embolic agents for TAE procedures Spies *et al.* determined that incomplete infarction and a high rate of tumor recurrence occur for some deformable particles [124]: the clinical consequence was so severe that the study was halted after only 36 patients had been enrolled. This emerging data suggests that a deformable particle is not ideal due to its variable characteristics once delivered [124-126]. Since existing TAE materials are based on hydrogels, it is possible that the water content [99] may change during the procedure when exposed to non-ionic contrast media. More critically, the water content may subsequently change once in the body, contributing to variable terminal particle locations in highly deformable microspheres [122]. The changes in the water content could affect particle size and ultimately impact particle performance.

It has previously been proposed that deformable particles were necessary for particle delivery through micro-catheters. However this is no longer necessary since the majority of DEB-TACE procedures are performed using 75 to 300 μm particles and the inner diameter of commonly used catheters exceeds 600 μm [127]. The use of non-deformable microspheres may offer unique benefits not possible with the highly deformable hydrogels currently used. A non-deformable embolic agent could provide for better correlation between the particle's terminal location and the nominal vessel diameter since the diameter remains constant throughout the procedure. This may provide physicians with increased precision over the diameter of blood vessels that are occluded during embolization. Using non-deformable particles, it may be possible to reduce the risk of recanalization and poor tumor responses observed in highly deformable particles [125] since non-deformable particles are less likely to fragment during delivery.

An intrinsically radiopaque, "image-able", embolic agent would provide a method to determine the true spatial and temporal distribution of particles [11]. This intra-procedural feedback would provide the physician with the necessary information to modify the procedure in real time, thereby personalizing each treatment. Another benefit to image-ability is the standardization of materials and procedures for TAE, along with a new ability to quantify procedural success based on tumor response in relation to particle position [11, 16, 17]. With respect to TARE procedures, Vente *et al.* found that there is a need for high quality visualization of microspheres in order to determine patient specific radiation doses, thereby improving the safety and efficacy of these procedures [128]. This is also true for DEB-TACE procedures. Without information concerning the spatial-

temporal distribution of particles, it is difficult to determine if the tumor has received the appropriate therapeutic dose. This data would provide critical information for planning follow-up procedures so that undertreated areas can be specifically targeted to optimize therapy.

Chapter 4: Bioactive Glasses as Potential DEB-TACE Systems

Kehoe et al. recently developed a radiopaque zinc-silicate based glass proposed for use in TAE, which addresses the issue of image-ability [18, 19]. However, due to the high temperature synthesis, this glass cannot be loaded with traditional chemotherapies during production. An alternative approach to loading embolic microspheres with traditional chemotherapies is to produce bioactive glasses containing radiopaque elements that are also capable of releasing TII which may cause localized tissue damage in a manner consistent with accepted mechanisms of action for DEB-TACE. In this way, the bioactive glass would be provided both radiopaque and "drug-loaded", thereby ameliorating the current material limitations of DEB-TACE. These glass particles would be visible under x-ray imaging and be provided as a pre-loaded particle, eliminating the logistical issues whilst concurrently extending the shelf life as compared to existing material technologies. In order to design a bioactive glass material for use in DEB-TACE that provides for both "image-ability" and delivery of a therapeutic agent, it is important to first understand what a glass is and how its properties can be manipulated.

Specifically for medical applications, silicate based glasses have been used clinically for the repair and regeneration of hard tissues for over 30 years and have a proven track record of excellent biocompatibility [25, 129, 130]. The success of these glasses in these applications is due to their ability to bond directly to bone, which is attributed, in part, to the partial dissolution and recrystallization of ions at the implant surface [25, 130]; providing a surface with the appropriate microstructure for cells to adhere to and subsequently proliferate on. Recent developments have shown that the ions released from

bioactive glasses, termed TII, can perform much more critical functions than simply dissolution and recrystallization. TII directly impact cellular functions by up-regulating gene expression [131], particularly genes involved with angiogenesis [132-134] and osteogenesis [135-137], both of which are crucial for effective implant integration. The therapeutic effect of different TIIs, summarized in two reviews by Lakhar et al. [22] and Hoppe et al. [23], show that TIIs may modulate and/or improve osteogenesis, angiogenesis and inflammatory responses to bioactive glasses both *in vivo* and *in vitro*. Based on these data, a new design philosophy is emerging that aims to trigger specific host responses through localized delivery of TIIs from bioactive glasses [22, 23, 25]. From this perspective, bioactive glasses have the potential to act as delivery vehicles for a vast number of TIIs in applications outside of hard tissue repair and regeneration [138]. For completeness, it is important to note that glass-based therapies are also used to deliver localized radiation therapy and localized hyperthermia therapy in oncology applications. Reviews on these applications and technologies are provided elsewhere [139, 140].

4.1 Material-Host Responses Bioactive Glasses

The first bioactive glass was developed by Hench in 1969, under the trade name Bioglass®, which promoted osseointegration into hard tissues rather than fibrous encapsulation [141]. Bioglass® is a degradable glass with the following composition, listed as mol %: 46.1SiO_2, 24.4Na_2O, 26.9CaO and 2.6P_2O_5 [142]. The composition of Bioglass® encourages direct bonding of bone to the implant since ions released from the surface are able to trigger the body to make new bone [143]. First, Na^+, PO_4^{3+} and Ca^{2+}

dissolve from the glass network, which causes a subsequent increase in the local pH. The high pH promotes cleavage of the silica network (Si-O) bonds by OH^- releasing $Si(OH)_4$ at the surface of the implant. Subsequently, Si-OH condenses onto the surface of the glass, which creates a repolymerized silica rich surface with a high concentration of amorphous $CaO\text{-}P_2O_5$. This surface interacts with hydroxyl and carbonate groups within the host, causing amorphous $CaO\text{-}P_2O_5$ to form crystalline hydroxycarbonate apatite (HCA). The host responds to the presence of HCA by producing extracellular matrix that interacts with the HCA surface, forming an extremely strong bond [144]. Excellent clinical success has been achieved with Bioglass® based products. Over a million procedures have been performed using Perioglas®, which is used primarily to repair bone defects in the jaw [129]. One of the most successful clinical products is NovaMin®, a particulate additive to toothpaste used to treat and prevent sensitive teeth by promoting remineralization of small defects in tooth enamel [129].

To date the term biocompatibility is used ubiquitously with implant integration in hard tissue repair. However, 'biocompatibility' is defined by Black as the ability of a material to perform with the appropriate **host** *and* **material** response in a particular application [145], which encompasses much more than implant integration. If one considers the definition of biocompatibility in the context of cancer therapy, the appropriate host and material response results in cell death. Therefore the bioactive glass design paradigm shifts from tissue repair and regeneration to localized tissue damage. From a design perspective, the simple compositional control over glass properties and their ability to release TII is congruent with the emerging consensus in the literature, which states that

research should “aim to develop synthetic materials that establish key interactions with cells in ways that unlock the body’s innate powers of organization and self-repair.” [146]. With this in mind and the knowledge that glass properties are easily modulated through compositional changes, silicate based glasses can be designed to deliver TII that induce cell death. In order to do this, the composition-structure-property-function relationships of glasses and their constituents must be well understood.

4.2 Composition-Structure-Property Relationships in Glasses

The broadest definition of a glass is an amorphous solid exhibiting glass transformation behavior [147]. In this way glasses can be thought of as solid liquids since their structure is similar to traditional liquids. Using the above definition many different forms of glasses exist, including organic glasses typically composed of polymers, metallic glasses composed of metals and their alloys, and inorganic glasses, such as those based on silica.

Control over glass properties and function is dependent on composition-structure relationships. In order to design glasses for specific purposes these relationships need to be understood. The elements within the glass are chemically bonded to each other in a random network. Zachariasen’s random network theory has four rules that must be “followed” to form a hypotethical glass A_xO_y: 1) an oxygen atom is linked to only two atoms of A, 2) the oxygen coordination around A is small (three or four), 3) the polyhedron of A can only share corners and 4) at least three corners are shared [148]. Modifying the Random Network Theory, Cooper combined rules three and four and

stated that each oxygen polyhedron must be connected to at least three other polyhedrons [149].

Sun attempted to explain the process of glass formation, in melt derived glass, as the inability of bonds to rearrange upon the rapid transition from liquid to solid when quench cooled. He attributed this to high single bond strengths (E_d) between a metal center (A) and the surrounding oxygen atoms [150]. A-O bonds with greater single bond strength are less able to reorganize during cooling. In this way, Sun separated the components of a glass are into three classes: network formers (NWF), network modifiers (NWM) and network intermediates (NWI). NWF, as their name implies, form the network structure of the glass and have high E_d. The most common example of a NWF is SiO_2 and the Si-O bond has an E_d of 106 kcal/mol. NWMs have low single bond strengths, which allow these bonds to rearrange easily and thereby modify the random network. Na_2O is a common NWM and the E_d is 20 kcal/mol. NWI are elements that can behave as either a NWF or NWM. PbO is used as a NWI and the E_d is 73 kcal/mol. In general the E_d for NWFs is 80 kcal/mol and above, for NWM 60 kcal/mol and below. The E_d for NWI are between 60 and 80 kcal/mol [151]. Another method used to classify the function of elements in a glass is based on the cationic field strength of the element, which is proportional to the force exerted on a point charge at one oxygen bond length from the cation. In this way Deitzel classified NWFs as having a field strength between 1.3 and 2. NWMs have field strengths between 0.1 and 0.4. NWIs have field strengths between 0.5 and 1 [152]. Often elements are classified into the same groups when using either Sun's or Dietzel's model, however there are cases when elements are classified as a modifier in

one model and an intermediate in another model. As an example, Sun's model predicts La will be a NWM [151], while Dietzel's model classifies La as a NWI [153].

In order to understand how to modulate the properties of glasses it is important to understand how the NWF, NWM and NWI impact the atomic/molecular scale structure of the glass and as a consequence, contiguous properties. The NWFs bond together through oxygen atoms to form a 3-dimensional architecture of the glass network and it is this bonding structure that is responsible for the observed physical properties of glasses. In silicate-based glasses, Si adopts a tetrahedral structure and bonds to four oxygen (O) atoms [154]. These oxygen atoms can either form bridges by bonding to other Si tetrahedron, termed bridging oxygen (BO) or can form non-bridging oxygens (NBO) when bonding to NWM elements. Q^n terminology is used to denote the number of BO around the Si. As an example, vitreous silica contains only SiO_2, with each Si surrounded by four BO oxygen atoms resulting in a Q^4 structure [151]. When NWM elements are added to the glass, BOs are replaced by NBOs, thereby reducing Q^n. In the case of M_2O, where M is in a +1 oxidation state, each M^+ produces one NBO. The NBO is only anchored to one Si tetrahedron and therefore breaks up the three dimensional network. As the amount of M_2O increases the number of NBOs increases causing a greater disruption in the 3-dimentional network and this forces some of the silicon atoms into Q^3, Q^2 or Q^1 structures, depending on the M_2O concentration [155].

Network connectivity (N_c) is used to numerically describe the effect NWM and/or NWI additions have on a glass structure. N_c is defined as the ratio of the average number of BO to the number of NWF elements in the glass [155] as shown in equation 4.1.

N_c= (# BO - # NBO)/ total # of Bridging Elements 4.1

For vitreous silica there are no NBO therefore the N_c=4. Addition of NWM causes an increase in NBO, which causes a subsequent reduction in the N_c. NWI species complicate the calculation of N_c due to the fact that they can act as either a NWF, increasing the number of BO, or as a NWM, increasing the number of NBO. Increases in the number of NBO results in a lower N_c value and a more fragmented the network. Properties linked to N_c include glass transition temperature (T_g, the temperature when an amorphous solid becomes a super-cooled liquid [156]), thermal expansion coefficient, glass-in-glass phase separation, density and durability [157].

It is possible to verify the theoretical structure as determined by N_c calculations using magic angle spinning nuclear magnetic resonance (MAS NMR). This spectroscopy technique is used to determine the Q^n species and their relative amounts present in the glass, which provides a means to assess N_c [158]. However, Q^n speciation using MAS NMR is complicated by the fact that glasses are amorphous and therefore have very broad peaks. Studies of crystalline materials using MAS NMR show sharp peaks due to the ordered arrangement of the atoms in a crystal structure, which gives rise to well resolved spectra. In glasses this is not the case; bond angles and bond lengths vary in an

amorphous material, which changes the local environment around each atom, broadening the spectra i.e. there are more possible atomic arrangements in glasses than in crystals. Generally, the peak positions of glasses are similar to the chemical shifts of a corresponding crystalline material; however, the peak is broadened in glasses. This is due to the fact that atomic arrangements in glasses, over the short range i.e. the nearest neighbor, are similar to that of a corresponding crystalline material [159].

All of the oxygen atoms in vitreous silica are in a Q^4 arrangement [151]. As NWMs or NWIs are added to the glass the bonding structure around the Si center changes, which is observed as a peak position shift of the chemical shift in the MAS NMR spectra. Generally, the chemical shift range for the different Q^n species are as follows: Q^4 centers, between -120 and -105; Q^3 centers, between -100 and -90 ppm; Q^2 centers between -90 and -70 ppm; Q^1 centers between -70 and -95 ppm and Q^0 centers between -65 and -80 ppm [160]. It is clear that there is significant overlap between the different Q^n species, which makes it difficult to specifically identify all of the different Q^n species present. Q^n speciation is further complicated by the fact that peak position is also dependent on the electronegativity of the next nearest neighbor to the Si center. NWM or NWI with increased electronegativity compared to Si will cause the peak position to move downfield. This explains why the peak position of Si with a Q^3 structure bonded to Zn can overlap with Si with a Q^2 structure bonded to two Al [160].

Understanding the role a particular additive will play in the glass structure is imperative to designing glasses with the specific properties for an intended application, which then

imparts predictive power over the final properties of a glass. Although N_c can be a good predictor of glass behavior in simple glasses, it has limited use for more complex glass compositions. In particular, Hill acknowledges that N_c calculations do not account for field strength or charge to size ratio, which also impacts glass properties [161]. Accepting these limitations to N_c, there are some important general trends observed between N_c, composition and glass properties. As NWMs are added to vitreous silica, N_c is reduced, T_g decreases [162], density increases [163, 164] and the glass becomes more susceptible to degradation [155]. With respect to biologically active glasses, Hill has connected degradation (i.e. ion release) to N_c, showing that as N_c is reduced, bioactive glasses become more degradable and increases in N_c produce more durable glasses [155, 157, 161]. The ability of silicate glass systems to elicit a biological response is due, in part, to the release of ions from their surface.

Generally a bioactive material is defined as a material that elicits specific and desired biological activity [165]. For biologically active glasses used in hard tissue applications, biological activity is derived from the release of ions from the glass network followed by repolymerization of that same material that subsequently interacts with the host environment to produce an implant that is integrated with the local tissue [144]. There is a fine balance between ion release and either promoting or preventing cell growth. The key factor in controlling ion release is control over composition, which thereby controls N_c. Eden *et al.* determined that a glass with a N_c greater than 2.6 is generally not biologically active because of its resistance to dissolution and that the optimum N_c range is typically between 2.0 and 2.6 for hard tissue applications [166]. Through careful

control of glass composition, susceptibility to degradation can be controlled [167] and thereby biological active glasses can be designed to deliver TIIs payloads.

4.3 Therapeutic Inorganic Ions Modulate Host Responses

Biologically active glasses have been designed to deliver therapeutic inorganic ions (TII) in dental applications. Initially NovaMin®, a fine particulate composed of Bioglass®, was used in toothpastes designed to relieve pain from hypersensitivity by causing mineralization of tubules in dentin [129]. The success of NovaMin® prompted the development of a biologically active glass containing CaF_2 that release fluoride ions, which then mineralized into flouroapatite [168].

Recently it has been recognized that the biological role of TIIs extends far beyond simple mineralization and that these ions play an active biological role through gene activation. A number of reviews have summarized the different TIIs incorporated into bioactive glasses for improved angiogenesis and osteogensis [22, 23, 169, 170]. Evidence from *in vitro* studies show that addition of copper (Cu) and cobalt (Co) ions to cell culture media can modulate the production of factors associated with angiogenesis: HIF-α and VEGF. Wu *et al.* cultured human bone marrow stromal cells on a mesoporous bioactive glass containing 5 mole % Cu demonstrated increased production of VEGF and of HIF-α, biological markers for angiogenesis. In fact, when these cells were exposed to extracts of the same glass they demonstrated a concentration dependent increase in VEGF and HIF-α [135]. Lee *et al.* cultured a human osteosarcoma cell line (MG63A) on titanium phosphate glass disks doped with 0, 5, 10 and 15 mol% of CoO, substituted for $CaCO_3$.

VEGF concentration (normalized by number of cells) was significantly increased for all glass samples, with the highest observed VEGF concentration occurring in the 5 and 10 % Co doped glasses, which suggests that there is an optimum Co concentration for stimulating VEGF expression [171].

There is a growing body of evidence that indicates that Zn and Sr doping in bioactive glasses promotes osteogenesis. Oki *et al.* evaluated the effect of a Zn doped bioactive glass (64% SiO_2, 26%CaO, 5% ZnO, and 5% P_2O_5 (mole%)) on the activity of alkaline phosphatase (ALP) from human fetal osteoblasts and showed that Zn doped bioactive glass increased ALP activity compared to controls [172]. Saino *et al.* evaluated a human osteosarcoma cell line (SAOS-2) after culturing on sol-gel derived silicates and found that the Zn-doped glasses had 2-fold greater extracellular matrix deposition compared to the undoped glasses [173]. Gene expression was also evaluated using quantitative reverse transcriptase polymerize chain reaction (RT-PCR) and showed that type-I collagen, bone sialoprotein and osteopontin genes were expressed to a greater extent in the Zn-doped glass [173]. Sr has been shown to have a positive impact on osteoblast differentiation, proliferation and matrix deposition. RNA collected from cells cultured with Sr containing bioactive glass has been analyzed using RT-PCR for the presence of common genes associated with osteoblast function: collagen type 1, ALP, bone sialoprotein, Runx2, osteopotin and osterix [174-176]. In these studies, one or more of the genes listed were up regulated when cultured on Sr-doped bioactive glasses. Clearly, there is a body of literature that indicates that TIIs like Zn and Sr have the potential to elicit a beneficial host response in hard tissue applications.

Control of the composition-structure-function relationship is critical to controlling the properties of a bioactive glass. The composition creates the chemical structure of the glass, which in turn governs function. Many of the commercially available bioactive glasses are used in hard tissue augmentation, and therefore, are required to perform mechanical functions as well as promote tissue integration. The application of bioactive glass as an occluding agent and vectored drug delivery vehicle does not require the same stringent mechanical requirements as in hard tissue applications. This allows for greater freedom to develop compositions that have therapeutic impact when released from the glass. The production of an inherently radiopaque biologically active glass composed of elements that elicit a cytotoxic response in different HCC models will be the focus of this thesis.

4.4 Bioactive Glasses Designed as Therapeutic Inorganic Ion Delivery Systems

In a review of tissue engineering therapies, Place *et al.* described a shift in the design paradigm of biomaterials from one of complexity to one of simplicity. They argue that research should focus on designing biomaterials that elicit desired biological responses by triggering cellular functions that unlock the native healing properties of the body through simple structural and/or chemical composition [146]. With respect to DEB-TACE particle design, perhaps the simple approach, where the embolic agent, radiopacifier and drug are intrinsically one and the same, is appropriate. As the goal of DEB-TACE procedures is to provide permanent embolization along with sustained therapeutic delivery, degradable glasses based on phosphate and borate systems were not

considered for use in this system, as permanent embolization would not be possible. Kehoe *et al.* applied the rationale of simplicity to designing a radiopaque embolic agent for TAE, composed of a durable and intrinsically radiopaque silicate glass, which has demonstrated excellent *in vivo* visibility [20]. Building on the philosophy of simplicity and considering the versatility of silicate glasses to provide for predictable delivery of TIIs, these materials offer a vast number of compositional possibilities capable of meeting the requirements for the "ideal" embolic agent. The question is: what elements should be included in these glasses?

4.4.1 Metals Used in Chemotherapy

To determine what TIIs should be included in a glass delivery system, it is important to first evaluate metal-based chemotherapeutic agents. These drugs may give insight into possible therapeutic ions for inclusion into bioactive glasses. Historically, metal containing drugs have been used to treat cancer as far back as the 16^{th} century [177]. Modern use of metals in cancer therapy stems from the discovery of the cytotoxic effects of cis-diamminedichloroplatinum (II), known today as cis-platin [178]. From this discovery, other platinum-based chemotherapeutics have been developed that have significant clinical use worldwide and include carboplatin and oxaliplatin [179, 180]. Since the discovery of cis-platin and its analogues many metals have been used as targets for chemotherapy drugs [181, 182]. Much research has been done investigating the role of metals and their complexes in the treatment of disease. In general, the therapeutic effect of a metal is due to its ability to modulate the activity of enzymes and/or to alter the molecular structure of biologically important molecules [182, 183]. Another

important effect of metals is their ability to generate reactive oxygen species (ROS), which has been connected to the cytotoxic effect of metal compounds on cancer cells [181-183].

Many different metal-containing compounds, other than cis-platin and its derivatives have been studied as chemotherapy agents [184]. However, the toxic effect of metal-based drugs is typically non-selective, which contributes to a general reluctance in developing metal-based therapies [182]. In a review article in Science, Thompson and Orvig address the need to develop new metal-based therapies with the understanding that it is the *dose* that differentiates a therapy from a toxin [185]. Some examples of these toxic compounds that have therapeutic benefits in the appropriate doses are arsenic trioxide (As_2O_3), used to treat acute promyelocytic leukemia [186], and antimony trioxide (Sb_2O_3), which is active against human leukemia cell lines [187]. In these two examples, dose determines if the compound is toxic or therapeutic. Due to the *in vitro* and *in vivo* success of experimental therapies based on transition metal therapies there has been a drive to develop new cancer therapies based on these systems [188].

In a glass designed for DEB-TACE, the ideal TII must be homogenously incorporated into the glass network and must also have the ability to be released from the glass at therapeutic levels. Keeping in mind the desire to provide a radiopaque material for DEB-TACE, it is also desirable, although not necessary, that the TII would contribute positively to the radiopacity of the glass system. However, the most critical and important feature of the ideal TII is that it will have demonstrated effectiveness treating cancer. To

this end, two target TIIs have been identified due their established anticancer properties (*in vitro* and/or *in vivo*): lanthanum and vanadium. The following two sections will outline the beneficial properties of these two elements for inclusion in a DEB-TACE material.

4.4.2 Lanthanum

Lanthanum (La) belongs to the rare earth metals and typically exists in the 3+ oxidation state [189]. Generally, naturally occurring lanthanum compounds are insoluble at physiological pH, which is perhaps why no known native biological roles for lanthanum have been identified [190]. La^{3+} is very similar to Ca^{2+} in atomic radius, coordination environment, and ligand binding properties, but is a stronger Lewis acid [190]. For this reason, Fosrenol® composed of $La_2(CO_3)_3$, has been used as a dietary phosphate scavenger in dialysis patients that develop hyperphosphatemia [191]. Patients treated with $La_2(CO_3)_3$ have the unexpected side effect of radiopaque colons, which makes diagnosis of rectal bleeding difficult [192]. Yet, in the context of DEB-TACE particle, the radiopaque nature of La is highly desirable.

Lanthanum (La^{3+}) has been investigated for its anticancer properties due to its the similarity with calcium (Ca^{2+}) in biological systems [193]. Dai *et al.* exposed NB4 cells (acute promyelocytic leukemia cell line) to increasing concentrations of $LaCl_3$, which caused concentration dependent cell death mediated by apoptosis [194]. Su *et al.* determined that the mechanism of action of lanthanum citrate on cervical cancer (HeLa) cell lines involves the initiation of anoikis [195], which is a special type of apoptosis

initiated by inadequate or inappropriate interactions with the cells and their extracellular matrix [196]. In an *in vitro* study using human gastric cancer cells, Shi *et al.* demonstrated that incubation with $LaCl_3$ caused down regulation of proteins responsible for maintaining cell morphology while simultaneously causing up regulation of proteins responsible for controlling RNA synthesis [197]. In a chicken lymphoblast tumor cell line treated with $LaCl_3$ Zhang *et al.* showed that $LaCl_3$ induced apoptosis through a telomerase mediated mechanism [198]. Heffeter *et al.* showed, in four different multidrug resistant human cancer cell lines, that [tris(1,10-phenanthroline)lanthanum(III)] trithiocyanate has both cytostatic and cytotoxic effects [199]. It is very interesting that both lanthanum citrate and lanthanum chloride have anticancer properties because it suggests that it is the free La^{3+} ions that provide for the therapeutic effect. This makes La a very promising candidate for inclusion into a novel bioactive glass as a TII,.

4.4.3 Vanadium

The second element identified as a target TII is Vanadium (V). V is a transition metal that can exist in a number of different oxidation states, predominantly +4 and +5 in biological systems and is highly dependent on pH. In 2001, a report published by the Food and Nutrition Board of the Institute of Medicine stated that there were no known biological functions for vanadium and reported no recommended daily intake for this element [200]. However, more recent research has shown that vanadium can mimic insulin, has action on growth factors, and can be osteogenic [201]. Humans ingest vanadium as a trace element in food, between 10 and 60 μg/day. In the stomach, ingested vanadium is converted to VO_2^+, adsorbed in the duodenum and is subsequently stored as part of the

mineral component of bone [202]. Vanadium deficient diets in higher animals have been connected to increased abortion rates, poor growth rates, lipid metabolism impairment and inhibition of the Na^+/K^+ ATPase in the kidney, brain and heart tissues [203]. Pharmacologically vanadium has been used for its diuretic effects, vasoconstriction abilities, to increase the oxygen affinity of hemoglobin, and has also been used to lower blood cholesterol, triglyceride and glucose levels [203]. More recently, the discovery of the insulin mimetic behavior of vanadium salts and vanadium-based compounds has lead to the development new treatments for type II diabetes [204], which are beginning to be studied in phase 1 and phase 2 clinical trials [205]. In a small study, 11 patients with type II diabetes received vanadyl sulfate for a six-week period. These patients showed a decrease in their fasting glucose levels and an increase in the rate of endogenous glucose production (EGP). This suggests that vanadyl sulfate has a greater affect in liver tissue, where EGP is produced, than in muscle tissue [206].

Clearly, vanadium plays a critical role biologically and shows promise as a treatment for type II diabetes. However, the use of vanadium in cancer therapy was largely ignored since initial studies in the 1960's found that vanadium compounds were inactive as a chemotherapy [207]. With the discovery in the mid 1980's that vanadium-rich diets inhibit chemically induced mammary carcinogenesis in rats, research in this area has been reinvigorated [208]. Studies in rats have shown that consumption of ammonium monovanadate in drinking water can prevent chemically induced hepatocarcinogenesis [209]. The potential use of vanadium salts as a therapeutic agent has gained credence since it was shown to have few adverse effects when used for the management of

diabetes [210]. Of particular interest to HCC therapy, Wang *et al.* have shown that vanadium concentrations are higher in HepG2, a HCC cell line, as compared to non-diseased L02 hepatocytes [211], suggesting that vanadium by be selective for cancer cells.

Evangelou *et al.* described four features that an ideal cancer therapy should possess: (1) antiproliferative effects, (2) cytotoxic and/or cytostatic through induction of apoptosis or necrosis, (3) reduction and/or prevention of metastasis and (4) prevention of drug resistance [212]. The function of vanadium-based compounds has been tested against a vast number of malignant cell types from multiple species and has been reviewed elsewhere [212]. Through these studies, it has been demonstrated that V possesses all of these features, which makes it an excellent candidate for consideration in this thesis as a target TII. The antiproliferative effects of vanadium-based compounds are due to cell cycle arrest at the G2/M phase, which has been connected to the inhibition of protein phosphotyrosines [213]. Sodium metavanadate ($NaVO_3$) has been shown to prevent cell proliferation in human prostate cancer cell line PC-3 due to cell cycle arrest at G2/M phase by production reactive oxygen species (ROS) [214]. Ray *et al.* showed that ammonium monovanadate (NH_4VO_3) caused apoptosis in MCF7 breast cancer cell line due to DNA fragmentation and inappropriate chromatin condensation [215]. The anti-metastatic behavior of sodium orthovanadate was evaluated in genetically modified rat 3Y1 cells known to be highly metastatic. It was found that metastatic cells grew in weakly bound colonies while normal cells grew in tightly bound colonies. Addition of sodium orthovanadate to metastatic cells caused their morphology to become similar to

the non-metastatic controls [216]. With respect to prevention of drug resistance, in multi-resistant cell lines, vanadium compounds have been shown to re-sensitize cells to therapy. As an example, in cis-platin resistant human ovarian cancer cells treated with chelated vanadium caused a significant increase in cytotoxicity of the cis-platin [217].

Based on the above information there are two general mechanisms of action for vanadium that may work synergistically: 1) production of ROS and free radicals that cause DNA damage and 2) interfering with cellular signal transduction due to the structural similarity between vanadate and phosphate, which interferes with intracellular phosphorylation processes [211]. All of these features, along with the well-established use of vanadium in glass make it an excellent candidate for a component in a novel bioactive glass used to treat HCC.

Chapter 5: Thesis Objectives

The overall objective of this work was to investigate glass materials suitable for use in DEB-TACE procedures. As such, three different embolic materials were synthesized, characterized and evaluated with respect to their potential use as DEB-TACE as outlined below:

1. The first original contribution of this thesis (Chapter Six) deals with the examination of a composite embolic material containing PLGA and the glass composition developed by Kehoe *et al.* [21]. The aim of this study was to synthesize intrinsically radiopaque composite embolic microspheres capable of being pre-loaded with DOX, thus providing an avenue to develop inherently radiopaque drug pre-loaded microspheres for DEB-TACE. To achieve this, a two-stage approach was adopted. Stage one comprised the systematic evaluation of composition-property relationships for nine different PLGA:Glass formulations of composite microspheres. Mathematical models based on a D-Optimal response surface methodology were developed to determine the optimal formulation that maximized radiopacity. In stage two, the optimized formulation was pre-loaded with DOX and the *in vitro* drug release characteristics and cytotoxicity against HepG2 cells were evaluated.

2. Transitioning from conventional design approaches the second original contribution of this thesis (Chapter Seven) is the evaluation of a new class of

potentially bioactive glasses composed of La_2O_3, Na_2O, ZnO and SiO_2. The aim of this study was to evaluate the composition-structure-property-function relationships as a function of La_2O_3 composition, with specific focus on the ability of this new glass formulation to provide for controlled release of lanthanum. Lanthanum was selected as a target TII due to its established cytotoxic effects in different cancer cell lines [195, 197-199, 218, 219]. The structural role of lanthanum was determined experimentally using ^{29}Si MAS NMR, density and T_g and theoretically using the Brow and Bunker model of glasses [220]. In addition, the clinical utility of the glass with respect to diagnostic imaging visualization was assessed using CT radiopacity. Finally, to assess the utility of these zinc-silicates to act as TII delivery systems the ion releasing characteristics of the glasses were assessed after exposure to simulated physiological conditions.

3. The third original contribution of this thesis (Chapter Eight) develops the philosophy of TII use in oncology and relates to a new class of bioactive glasses composed of V_2O_5, Na_2O, ZnO and SiO_2. This study evaluated the composition-structure-property-function relationships as a function of V_2O_5 composition with a specific focus on the ability of this new glass formulation to provide for controlled release of vanadium. Vanadium was selected at a target TII due to its established chemo-protective properties [209, 221], cytotoxic effects in different cancer cell lines [211, 215, 222] and its established use in cancer therapies [212]. The structural role of silicon and vanadium were determined using ^{29}Si and ^{51}V MAS NMR, density and T_g measurements. The ability of these glasses to deliver

their therapeutic payload (i.e. vanadium content) was determined after exposure to simulated physiological conditions. Subsequently, the *in vitro* host responses in HepG2 cells – cell viability and mechanism of cell death after exposure to glass extracts – were evaluated. The clinical utility of the glass with respect to diagnostic imaging visualization was also assessed using CT radiopacity.

Chapter 6: Synthesis and Evaluation of a Pre-Loaded Drug Eluting Radiopaque Composite Embolic Microsphere (CEM) for Transarterial Chemoembolization (TACE)

Nancy Kilcup[1], Sharon Kehoe[2], Elena Tonkopi[3], Bob Abraham[2,3], Daniel Boyd[1-4]

[1]School of Biomedical Engineering, Dalhousie University, Halifax, NS, Canada

[2]ABK Biomedical Inc., Halifax, NS, Canada

[3] Department of Diagnostic Imaging and Interventional Radiology, QE II Health Sciences Centre, Halifax, NS, Canada

[4]Department of Applied Oral Sciences, Dalhousie University, Halifax, NS, Canada

This manuscript was written by the candidate (Nancy Kilcup) under the supervision of Dr. Boyd, who provided guidance and assistance to all aspects of the work. Ms. Kilcup proposed, designed and conducted all of the experiments described. Ms. Kilcup assisted Dr. Tonkopi with CT radiopacity data collection and Dr. Tonkopi provided assistance with manuscript preparation regarding CT radiopacity. Dr. Kehoe provided extensive assistance and training for the Design of Experiments software, the analysis thereof, and manuscript review for Chapter Six. Dr. Abraham reviewed the manuscript the manuscript with respect to the clinical significance of the findings.

6.1 Abstract

The purpose of this study was to synthesize and optimize intrinsically radiopaque composite embolic microspheres (RCs) for sustained release of doxorubicin (DOX) in drug eluting bead transarterial chemoembolization (DEB-TACE). Using a design of experiments approach, 12 RCs composed of polylactic-co-glycolic acid (PLGA) and a radiopaque glass (ORP5) were screened over a range of compositions and examined for radiopacity (computed tomography (CT)) and density. In vitro cell viability was determined using an extract assay derived from each composition against the human hepatocellular carcinoma cell line, HepG2. Mathematical models based on a D-Optimal response surface methodology were used to determine the preferred RC. The resulting RC was validated and subsequently loaded with DOX between 0-1.4% (wt% of PLGA) to yield radiopaque composite drug eluting beads (RC-DEBs). Thereafter, the RC-DEBs were subjected to an elution study (up to 168 hours) to determine DOX release profiles (UV-Vis spectroscopy) and in vitro cell viability. RCs evaluated for screening purposes had densities between 1.28-1.67g.cm^{-3}, radiopacity ranged between 211-1450HU and cell viabilities between 91-106% were observed. The optimized RC comprised of 23wt% PLGA and 60wt% ORP5 with a corresponding density of 1.63 ± 0.001g.cm^{-3}, radiopacity at 1930 ± 44HU and cell viability of 89±7.6%. RC-DEBs provided sustained DOX release over 168 hours. In conclusion, the mathematical models allowed for the identification and synthesis of a unique RC. The optimized RC had similar density and cell viability to commercially available embolic microspheres. It was possible to preload DOX into RC-DEBs, such that sustained release was possible under simulated physiological conditions.

6.2 Introduction

Hepatocellular carcinoma (HCC) has the second highest cancer death rate worldwide [1] and is difficult to treat since 80% of cases are diagnosed at the intermediate or advanced stage, when curative treatments options are limited [2-4]. Conventional transarterial chemoembolization (cTACE) has been a standard option for patients with intermediate stage HCC. Generally the steps for a cTACE provide for loco-regional transcatheter delivery of a mixture of lipiodol with a chemotherapeutic agent often followed by bland particle embolization. There are many procedural variables that exist between interventional radiologists and institutions and, as yet, no consensus over the type of embolic agent, chemotherapeutic agent, location of injection and optimal end point has been achieved [13, 15]. The inability to directly visualize embolic particles during and after the procedure is also an additional source of procedural variability and has arguably limited the advancement toward personalized treatments for patients [11]: the argument being premised on the ambiguous relationships between patient outcomes and the spatial-temporal distribution of both the chemotherapeutic and embolic agents. Advancing knowledge in this context is critical to improving cTACE procedures. In cTACE, the chemotherapeutic agent is mixed with lipiodol (ethiodized oil), a radiopaque contrast agent, in an effort to provide real time clinical feedback on the spatial and temporal distribution of the agent within the vasculature. However, it is well known that lipiodol and chemotherapeutics (such as, doxorubicin (DOX)) do not provide for stable homogenous admixtures. Furthermore, significant increases in systemic levels of chemotherapeutic agents have been observed in patients receiving cTACE. To overcome

these limitations, drug-eluting beads (DEB) were developed to provide controlled and localized release of chemotherapeutic agents, thereby lowering systemic toxicity. Based on substantiating clinical evidence for lower complication rates and improved survivability, DEB-TACE has emerged as a preferred treatment option for patients with HCC [5-7]. In a one step procedure, DEB-TACE deploys embolic particles loaded with a chemotherapeutic agent (typically DOX) providing for simultaneous occlusion of blood vessels and localized DOX release [8, 9]. Ideally, particles used for DEB-TACE should be intrinsically radiopaque, so as to provide for direct intra-procedural feedback on the spatial and temporal distribution of particles [10, 11]; a feature which could provide for a variety of benefits, as outlined by Sharma et al. [11], including the personalization of a variety of embolization treatments. Additionally, it may be beneficial to have particles pre-loaded (by the manufacturer) with chemotherapeutic agents so as to overcome issues of shelf-life and pharmacy logistics associated with existing DEB-TACE drug eluting beads [12, 13]: presently, embolic particles utilized for DEB-TACE are composed of polymeric materials, such as sulfonated polyvinyl alcohol [223, 224] or sodium acrylate/vinyl alcohol copolymers [96, 97] [12, 13, 101] and as such, do not provide for the benefits of radiopacity, and require preloading in pharmacy, thereby limiting shelf-life to 24h.

Recently a new type of bland embolization material, based on a highly radiopaque and biocompatible multicomponent zinc-silicate glass (named ORP5), has been proposed in the literature for treatment of arteriovenous malformations and hypervascularized tumors [18, 19, 225]. Due to the high temperature synthesis of ORP5, it is not possible to pre-

load the particles with DOX for DEB-TACE procedures. To ameliorate this issue, it is proposed that ORP5 could be combined with an appropriate polymer to yield a composite material that is both radiopaque and suitable for DEB-TACE. Polylactic-co-glycolic acid (PLGA) is an excellent candidate for the polymer component due to its well-known drug delivery properties from microspheres [226] and its use in the synthesis of glass-polymer composites [227]. Previously, Kehoe et al. [21] demonstrated that it was possible to produce PLGA:ORP5 composites through a process of thermally induced phase separation (TIPS). However, the process was not suitable for preloading chemotherapeutic agents, nor did it provide for synthesis of clinically relevant particle size distributions. Consequently, alternative synthesis routes and formulations must be considered to prepare radiopaque composite (RC) embolic microspheres based on PLGA and ORP5.

The aim of this study is to synthesize, using a solvent extraction process, intrinsically radiopaque RCs (PLGA:ORP5) capable of being pre-loaded with DOX (i.e. radiopaque composite drug eluding beads (RC-DEBs)). To achieve this, a two-stage approach was adopted. Stage one comprised the systematic evaluation of composition-property relationships for nine formulations of RCs. This data was used to determine an optimal RC using mathematical models based on a D-Optimal response surface methodology from which to produce the RC-DEBs. RC-DEBs were evaluated in stage two where controlled drug-release characteristics and efficacy were evaluated

6.3 Materials and Methods

6.3.1 Stage 1: Composition-Property Relationships for RCs

6.3.1.1 Glass Synthesis and Characterization

ORP5 glass ($0.562SiO_2$–$0.035CaO$–$0.188ZnO$–$0.068La_3O_2$–$0.042TiO_2$–$0.035MgO$–$0.035SrO$–$0.035Na_2O$ mol. fraction [19]) with a D_{50} particle size of 51μm (lot# 12924/V3039 (1)-3) was synthesized. Glass particles were subsequently ground with an agate planetary ball mill (Pulverisette 7, Laval Labs Inc., Laval, QC, Canada) at 600rpm for a total of 82min. (4 x 3min. grinding segments followed by 14 x 5min. grinding segments). Particle size distribution was determined using a Mastersizer 3000 (Malvern Instruments, Laurent, QC, Canada). Background measurements of deionized water were used to zero the instrument. Obscuration value was set between 4-8%. The particle size was measured (n=5) using both a blue (λ = 470nm) and red (λ = 632.8nm) laser with values reported as the mean diameter D_{90}, D_{50} and D_{10}, which are particle diameters at 90, 50 and 10% cumulative size, respectively.

6.3.1.2 Design of Experiments and Generation of Models

A D-Optimal response surface method comprising two independent factors (Table 6.1) was utilized to establish composition-property relationships for nine formulations of RCs. The factors are as follows:

Factor A: Referred to as PLGA (wt%), represents the PLGA:DCM[2] ratio used to synthesize the RCs.

Factor B: Referred to as ORP5 (wt%), represents the ORP5:PLGA ratio use to incorporate ORP5 into the RCs.

[2] DCM refers to dichloromethane (full details are provided in section 6.3.1.3).

For clarity, the D-Optimal design maximizes the information about polynomial coefficients [18] whilst minimizing the variance associated with the estimates of the model coefficients. For statistical validity, three formulations were repeated for a total of 12 experimental runs. Response data (i.e. radiopacity, density and cell viabilities) were analyzed by D-Optimal algorithms through standard analysis of variance (ANOVA) using statistical software Design-Expert (Ver.8.0.3, Stat-Ease Inc. Minneapolis, MN) to calculate the coefficients of the following second order cubic polynomial equation 5.1:

$$Y = C_0+C_1X_1+C_2X_2+C_3X_1^2+C_4X_2^2+C_5X_1^2X_2+C_6X_1X_2^2+C_7X_1^3+C_8X_2^3 \quad (5.1)$$

where Y denotes the response, C_0 is a constant while C_1–C_8 denote the coefficient effects associated with individual factors or the two-way interactions. X_1 and X_2 denote the coded levels of PLGA and ORP5. X_1X_2 denotes two-way interactions between PLGA and ORP5. An optimal RC formulation was determined using models derived from the developed mathematical models using the desirability approach following standard procedures [227, 228].

6.3.1.3 RC Synthesis, Characterization and Optimization

RCs were synthesized using a solvent extraction method adapted from Park et al. [229]. Briefly, 12 different RCs were synthesized (Table 6.1) for stage 1 variable amounts of PLGA (25:75 lactic acid-co-glycolic acid mole %, M_w=113kDa; IV, 0.74dl/g; Lot #: LP-719, Lakeshore Biomaterials, Birmingham, AL) was dissolved in dichloromethane

(DCM, Sigma-Aldrich, Oakville, ON, Canada) followed by addition of variable amounts of ground ORP5 glass to form a suspension. The PLGA:ORP5 suspension was added through a 10mL syringe into a stirred (1200rpm) 2% aqueous polyvinyl alcohol (PVA, Sigma-Aldrich, Oakville, ON, Canada) solution. The subsequent suspension was stirred for a minimum of two hours to allow the microspheres to harden by extraction of the DCM. The RCs were then filtered, rinsed three times using distilled water and freeze dried (FreeZone$^{2.5}$ Labconco, Kansas City, MO) over night.

6.3.1.4 RC Characterization

6.3.1.4.1 RC Radiopacity

Quantitative radiopacity measurements of each RC formulation (n=5) were determined by taking Axial CT scans (1mm slice thickness, pitch=0.5, 140kVp) through glass vials using a Siemens Somatom Definition Flash Scanner (Siemens Healthcare, Erlangen, Germany). All measurements were performed on the 'as synthesized' microspheres. A clinically used contrast agent, Isovue® 370 (Iopamidol; 370mg of non-ionic iodine per mL, Bracco Diagnostics Inc., Monroe Township, NJ) was tested at half strength (i.e. mixed 50:50 with saline) under the same CT settings in order to benchmark the RC compositions. Radiopacity is reported in Hounsfield Units (HU) ± SD.

6.3.1.4.2 RC Density

The dry density of each RC composition was determined using helium pycnometry (AccuPyc 1340, Micromeritics, Norcross, GA) and reported as the average of 10 measurements ± standard deviation (SD). A zero pressure calibration was performed on a

1cm^3 aluminum chamber insert, which was used for all measurements, followed by a volume calibration using a stainless steel sphere with a known volume of 0.718512cm^3. The applied fill pressure was 19.500psig and the equilibration rate was 0.002psig/min. RC samples were added to the sample chamber until it was approximately 75% full and the mass was recorded. Before beginning the measurement all samples were put through a fill/purge cycle 10 times in order to remove any trapped air.

6.3.1.4.3 Preparation of RC Extracts for Cell Viability

As per Tsigkou et al. [230], 0.1g of 150-300μm RCs (n=3) were immersed in 10mL (1 % w/v) of sterile tissue culture water (Sigma-Aldrich, Oakville, ON, Canada) using 15mL falcon tubes for 24 hours. Specimens were incubated at 37°C in a shaking water-bath (Stuart Sb40, Techne Inc., Burlington, NJ) and agitated at 2Hz (longitudinal movement). After each incubation period, extracts derived were filtered using a sterile 0.20μm filter (Sarstedt, Montreal, QC, Canada) and stored at 4°C.

6.3.1.4.4 Evaluation of RC Cell Viability

Human hepatocellular carcinoma cell line HepG2, passages 5-10, (American Tissue Culture Collection (ATCC); Cederlane, Burlington, ON, Canada) were used for cell viability testing. Cells were grown in 75cm^2 tissue culture flasks in Eagles Minimum Essential Medium (EMEM, ATCC) containing 10% fetal calf serum (FCS, Sigma-Aldrich, Oakville, ON, Canada) at 37°C and 5% CO_2. Once cells reached 70% confluence the medium was removed, 2mL of 0.25% trypsin-EDTA was added to detach cells that were re-suspended in 3mL of EMEM containing 10% FCS. To achieve a

homogenous cell mixture the liquid was gently mixed using a 5mL pipette. 1mL of the cell suspension was transferred to 75cm^2 tissue culture flask containing 19mL of EMEM with 10% FCS. Flasks were placed in an incubator for approximately 2 days or until cells reached 70% confluence.

Subcultured HepG2 cells were used to evaluate the in vitro cell viability of the extracts produced above following an MTT assay [18, 227, 231]. 96-well plates (CoStar, Corning Incorporated Life Sciences, Tewksbury, MA) were seeded using 200µL per well of a 1x10^{5}cells/mL suspension. After 24 hours incubation (37°C, 5% CO_2) 20µL of each extract was added to the appropriate wells (n=3) and incubated for a further 24 hours. 20µL addition of tissue culture water was used as the positive control and 20µL addition of DMSO was used as the negative control. Extracts from Embosphere® Microspheres (Merit Medical Inc., South Jordan, UT), a triscaryl gelatin based embolic agent, were used as a commercial control. 22µL of 5mg/mL solution of 3-(4,5-dimethylthiazol-2-yl)-2,5-diphenyltetrazolium bromide (MTT, Sigma-Aldrich, Oakville, ON, Canada) in 0.1M phosphate buffered saline was added to each well for an additional 3 hours. Subsequently, 100µL of DMSO was added to each well after the medium was removed and gently agitated at room temperature for approximately 5 minutes. The absorbance of each well was measured a 580nm using a multi-detection microplate reader (Synergy HT, BioTek, Winooski, VT).

6.3.2 Stage 2: Drug Release Characteristics and Efficacy of RC-DEBs

The optimum composition (23 wt% PLGA; 60 wt% ORP5), determined from Stage 1, was synthesized and characterized similarly to all other RC formulations to validate the characteristics.

6.3.2.1 Synthesis of RC-DEBs

RC-DEBs were synthesized similarly to RC formulations and were based on the optimal RC formulation (23wt% PLGA; 60wt% ORP5). In order to assess the initial loading capabilities of this RC formulation, DOX hydrochloride (Lot# SLBF-1340V, Sigma-Aldrich, Oakville, ON, Canada), at variable levels from 0.5, 1.0 and 1.4 wt%, w/w PLGA (equivalent to 46, 92 and 127mg of DOX, respectively, in 9.2g of PLGA) was added during the synthesis process at the point where PLGA was dissolved into DCM along with the ORP5, yielding three groups of RC-DEBs, (1 group per DOX loading condition) for subsequent analysis.

6.3.2.2 Preparation of Extracts, DOX Release Profiling and Cell Viability

Extracts from RC-DEBs were prepared as previously described at 1, 4, 8 24 and 168 h. DOX release characteristics were quantified using UV-Vis spectroscopy. Each DOX containing extract was measured in triplicate by placing 100µL into three different wells on a 96 well plate (CoStar, Corning Incorporated Life Sciences, Tewksbury, MA). The absorbance of each well was measured a 480nm using a multi-detection microplate reader (Synergy HT, BioTek, Winooski, VT). The DOX absorbance was calibrated using DOX

solutions made in tissue culture water with known concentrations between 0-0.25mg/mL. Cell viability was tested as previously described.

6.3.3 Statistical Methods

One-way analysis of variance (ANOVA) was employed followed by a Tukey post-hoc test to compare the mean values of cell viability (n=3). Two-way ANOVA was employed followed by a Tukey post-hoc test to compare the mean values of DOX concentration (n=3) for each extract condition. Error bars on all graphs represent standard deviation about the mean. Data was considered significant when $p \leq 0.05$. All calculations were done using Prism 6 for Mac OS X (GraphPad Software Inc., La Jolla, CA).

6.4 Results

6.4.1 Stage 1:Composition-Property Relationships for RCs

ORP5 particles used for the synthesis of RCs had the following particle size distribution characteristics: D_{90} = 21.5μm, D_{50} = 6.09μm and D_{10} = 0.162μm. RCs synthesized at 30wt% PLGA consistently demonstrated a lack of sphericity; reduction to 23wt% PLGA provided consistent synthesis of spherical particles. The range of properties observed for the RCs examined in Stage 1 are summarized as follows and supported with Table 6.1 and Figure 6.1:

- Radiopacity values ranged between 211.3 ± 20 and 1455 ± 65HU (Table 6.1).
- Density values ranged between 1.23 ± 0.0030 and 1.67 ± 0.0034g.cm^{-3} (Table 6.1).
- Cell viability ranged between 91 (±17) – 106 (±11)% (Figure 6.1).

For comparison purposes the observed CT radiopacity of half strength contrast media was 2455±23HU.

Table 6.1: RC formulations used for Stage 1: composition optimization including measured values for radiopacity and density ± standard deviation

Label	PLGA (wt%)	ORP5 (wt%)	Radiopacity (HU)	Density (g.cm^{-3})
RC1	30	60	1317±35	1.67±0.003
RC2	30	20	523±53	1.28±0.003
RC3	10	47.8	972±17	1.61±0.004
RC4	30	60	1455±65	1.63±0.001
RC5	16	60	1077±22	1.61±0.006
RC6	21.4	37.4	912±19	1.54±0.001
RC7	19	20	574±20	1.43±0.003
RC8	23	52.8	1316±68	1.66±0.001
RC9	30	41.2	765±25	1.56±0.001
RC10	10	20	378±10	1.44±0.002
RC11	10	20	211±20	1.45±0.002
RC12	30	20	1283±31	1.41±0.001

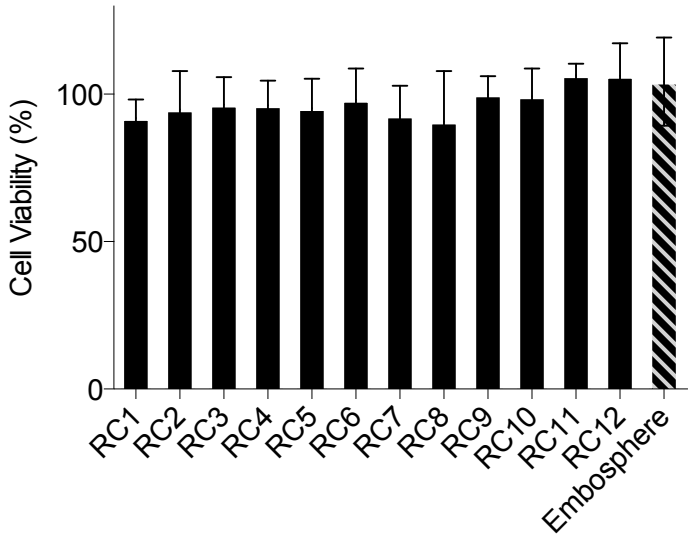

Figure 6.1: Cell viabilities (%) for extracts derived from the RCs vs. control.

Reduced linear models for radiopacity and density demonstrated significant model terms (Table 6.2). To understand the effect of each compositional factor, the model equations in coded values will be discussed; with coded analysis, the units of measure are normalized by coding, with the regression coefficients (measuring half the change from -1 to +1 for each factor). The regression coefficients for each equation (actual and coded) identify how the properties measured change relative to the intercept. The intercept in coded values is in the center of the compositional design space, while in actual values the intercept can be far from the design space; thus accounting for the variance in the level of importance for each factor between the actual and coded equations for both radiopacity and density. A statistically significant model for cell viability could not be determined. The reduced linear models for radiopacity and density have 'Prob>F values of 0.0037 and <0.0001, implying significant models at the 63 and 99% confidence intervals (CI), respectively.

Table 6.2: RSM models in terms of actual factors for the two independent factors PLGA and ORP5 and summarized ANOVA for each response.

		Summarized ANOVA			
		R^2	R^2_{adj}	R^2_{pred}	Prob>F
Radiopacity					
Actual:	-113.28 + 19.36PLGA + 15.49ORP5	0.7115	0.6473	0.4377	0.0037
Coded:	+893.75 + 193.62PLGA + 309.89ORP5				
Density					
Actual:	+1.283 + 0.006293ORP5	0.8341	0.8175	0.7525	<0.0001
Coded:	+1.54 + 0.13ORP5				

The model coefficients of determination (R^2: 0.7115 and 0.8341), difference between the R^2_{ad} and the R^2_{pred} (less than 0.2096 for both models) as well as the coefficient of variance 3.39-27.15% confirms the statistical validity of the developed models.

Based on the radiopacity model, both PLGA and ORP5 exert a significant influence on material properties in the following order of significance (in terms of coded factors): ORP5>PLGA. Graphical representation illustrating the extent of this composition-property (radiopacity) relationship is provided in Figure 6.2 (a). Based on the density model, ORP5 content is the only compositional factor to significantly influence density. Graphical representation of this composition-property (density) relationship is identified

in Figure 6.2 (b). As noted, the cell viability of RC formulations was observed to vary between 91 (±17) – 106 (±11)% (Figure 6.1); all RCs were substantially equivalent to the control, trisacryl gelatin microspheres (Embosphere®, Merit Medical, South Jordan, UT). There were no statistically significant differences observed between RC formulations.

(a)

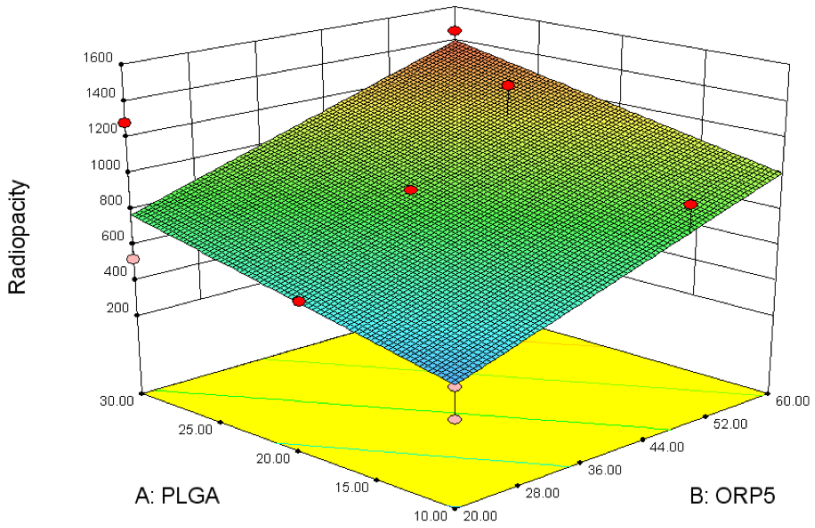

(b)

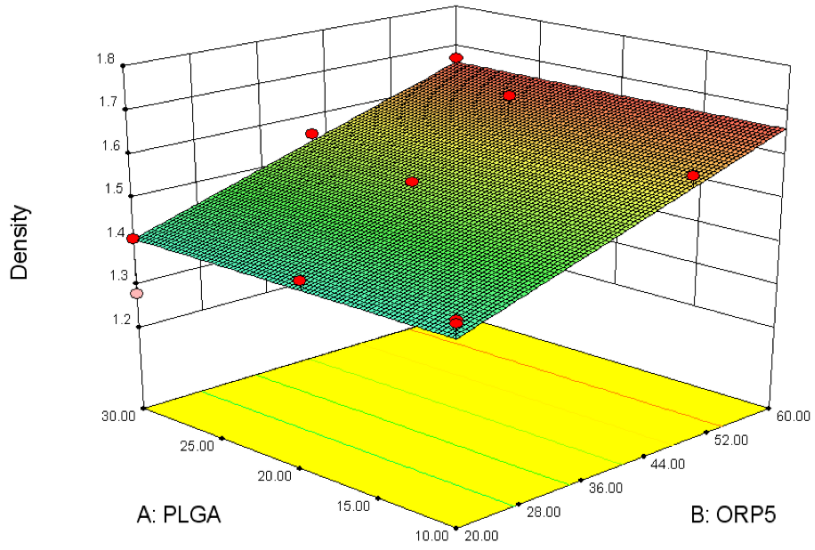

Figure 6.2: 3D surface contour plots show the effect of RC formulation on (a) radiopacity and (b) density within the observed design space.

To select an RC formulation for Stage 2, a desirability approach prioritizing radiopacity (full desirability criteria outlined in Table 6.3) was utilized. For PLGA and ORP5, the design space was constrained between 10 to 23wt% and maximized between 20 to 60wt%, respectively.

Table 6.3: Desirability optimization criteria

Name	Goal	Lower Limit	Upper limit	Lower weight	Upper weight	Importance
PLGA	In range	10	23	1	1	+++
ORP5	Maximize	20	60	1	1	+++
Radiopacity	Maximize	209.45	1454.52	1	1	+++++
Density	In range	1.26	1.67	1	1	+++

For completeness, the top four ranked solutions (based on the desirability criteria outlined in Table 6.3) are shown in Table 6.4. The optimal solution, for subsequent use in the synthesis of RC-DEBs (Stage 2), comprised 23wt% PLGA and 60wt% ORP5 and has a desirability of 0.900: predicted radiopacity and density of 1261HU and 1.66g.cm^{-3}, respectively. The optimal solution was validated experimentally and had a radiopacity of 1930 ± 44HU and a density of 1.63 ± 0.0007g.cm^{-3}.

Table 6.4: Optimal solutions based on the desirability approach.

Solution #	PLGA	ORP5	Density	Radiopacity	Desirability
1	23.00	60	1.66094	1261	0.900
2	23.00	59.84	1.65995	1259	0.898
3	22.71	60	1.66094	1256	0.897
4	14.97	60	1.66094	1103	0.813

6.4.2 Stage 2: Drug Release Characteristics and Efficacy of RC-DEBs.

The optimal formulation identified in Stage 1 (Solution 1, Table 6.4) was synthesized and loaded with DOX as to yield RC-DEBs. All RC-DEBs demonstrated a color change from white to red upon loading with DOX. It was noted that some of the DOX was lost during synthesis, as evidenced by the color change (from clear to red) in the PVA solution. Figure 6.3 (a) shows the release of DOX from the RC-DEBs after exposure to extract media for 1, 4, 8, 24 and 168 hours. Continued release was observed over the timeframe examined. A positive correlation exists between DOX loading and release levels. Statistically significant differences in maximum DOX release were observed for all loading conditions. With respect to the temporal modulation of DOX release from the RC-DEBs, the following observations were noted:

- Significant increases in DOX release were noted, as a function of time, for each group of RC-DEBs examined.
- The 1.4% DOX-loaded RC-DEBs demonstrated significant increases in DOX release between each time point.

- The 1.0% DOX-loaded RC-DEBs demonstrated significant increases in DOX release between all time points from 4 hours.
- The 0.5% DOX-loaded RC-DEBs demonstrated significant increases in DOX release between all time points from 24 hours.

(a)

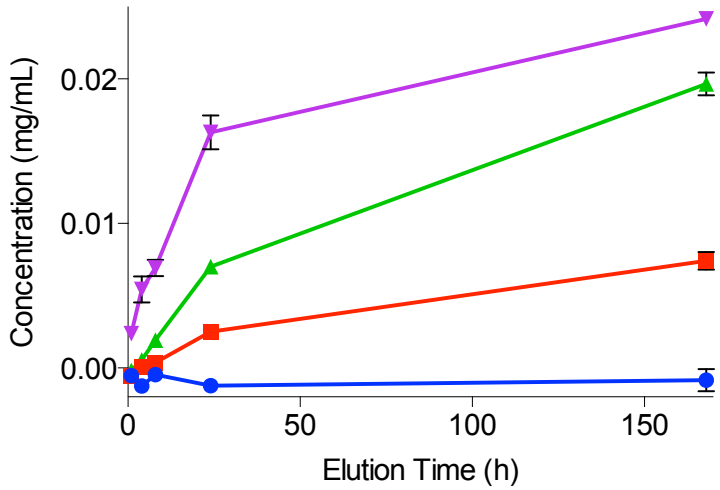

(b)

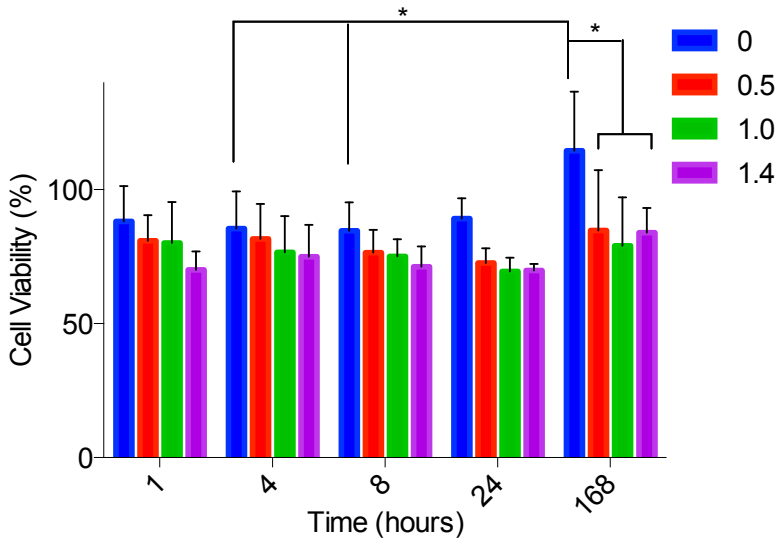

Figure 6.3: (a) DOX release and (b) Cell Viability (%) of extracts prepared from RC-DEBs (0, 0.5, 1.0 and 1.4 DOX (wt% of PLGA)) after 1, 4, 8, 24 and 168 hours[3].

With respect to the cell viability associated with RC-DEBs, the DOX release levels observed in this experiment did not decrease cell viability as a function of loading

[3] Error bars represent the standard deviation and are only shown when they exceed the size of the point

condition or elution period up to 24 hours. A significant increase in cell viability was noted between the unloaded RC-DEB formulation at 168 hours compared to 4 and 8 hours. At 168 hours, the unloaded RC-DEBs cell viability was significantly higher than that observed for the other RC-DEBs.

6.5 Discussion

Composition-property (radiopacity and density) relationships were established using DOE D-Optimal methodology for RCs having variable blends of PLGA and ORP5. In a traditionally designed experiment, one factor is varied at a time while all other variables are held constant, and this approach is repeated for each independent factor tested. This method is able to determine the effect of each component on the desired responses; however is unable to reveal second order interactions between independent factors. The DOE approach utilized in this study provides a robust methodology that reduces the number of RC formulations required for subsequent evaluation to determine first and second order interactions to establish important composition-property relationships such that the final characteristics of medical devices can be optimized.

The radiopacity regression model developed in this work showed a positive correlation with both PLGA and ORP5 content (Figure 6.2 (a)). With respect to CT radiopacity, radiopacity reached a maximum of 1455 ± 65HU for RC 4, which had the highest PLGA (30wt% of DCM) and ORP5 (60wt% of PLGA) content (Table 6.1). The observed CT radiopacity for RC 4 was significantly lower than half strength contrast media (2455 ± 23HU), which likely precludes angiographic evaluation to demonstrate their spatial and

temporal distribution. However, the primary advantage for these RCs relates to identifying their spatial distribution under CT evaluation, such that the interventional radiologist may be able to evaluate if tumors have been adequately targeted on either cone beam CT, immediately after embolization, or on conventional CT scan follow up. Furthermore, it is clear from the radiopacity data that embedding PLGA with OPR5 provides a mechanism for exacting control on radiopacity, which may provide a route to expand the radiopacity limits of the RCs produced herein. The density regression model was dependent on the wt% loading of ORP5 alone. This was expected since the density of ORP5 is 3.696g.cm^{-3} [18] compared to PLGA, 1.283g.cm^{-3}; taken from the y-intercept of the density regression model (Table 6.2). When an embolic microsphere is too dense there is a risk of particle sedimentation if conventionally prepared as a suspension, which can cause technical problems during delivery [232]. The dry density of all RCs in this study were lower than that of dry polyvinyl alcohol, 1.8g.cm^{-3} [18], a commonly used embolic agent, which demonstrates that the RC formulations examined may have clinically appropriate densities. Further evaluation of the RCs delivery characteristics however is warranted, to fully evaluate their clinical utility in the treatment of hepatocellular carcinomas. All RCs in this study have excellent cell viability, consistent with the work of Kehoe et al. [21] that evaluated the cell viability of microspheres comprising both PLGA and ORP5, in different ratios. From Figure 6.1, RC extracts have similar cell viabilities to each other as well as that of the control, with no statistically significant difference between any of the compositions.

Optimization of the RC composition in order to define the best RC-DEB formulation was designed to maximize radiopacity and cell viability and minimize density. Since there was no statistical difference observed between RC compositions for cell viability, no model could be determined that would adequately predict cell viability with respect to PLGA and ORP5; therefore it could not used as a criterion for composition optimization. Both radiopacity and density increase with incremental ORP5 content. It is therefore challenging to increase radiopacity while concurrently decreasing density based on the existing formulations. On this basis, and from the composition-property relationships established, the need to minimize density, as a criterion in the optimization was investigated at a reduced importance level compared to radiopacity. To validate the optimal formulation Solution #1 (Table 6.4) was synthesized and verified to have a radiopacity of 1930 ± 44HU and density of 1.63 ± 0.0007g.cm^{-3}. The radiopacity value was much greater than predicted, indicating poor model predictability with respect to radiopacity. This is most likely due to the high standard deviation values amongst the raw data, reported in Table 6.1. Radiopacity was measured on "as made" RCs comprising a wide range of particle sizes, which may have led to inconsistencies across each RC sample subjected to CT evaluation potentially leading to an unknown number of radiolucent voids of varying sizes, which may artificially reduce the measured radiopacity of the measured sample. The density value matched very well with the predicted value from the DOE model indicating good model predictability with respect to density.

Stage 2 of this study was designed to investigate both the feasibility of DOX loading RC-DEBs and to evaluate their release properties; for this reason low DOX loading levels were selected. Evaluation of the drug-release characteristics and efficacy of the RC-DEBs, the RC Solution #1 described above was loaded with DOX at 0, 0.5, 1.0 and 1.4% (wt% of PLGA) and subjected to a time-dependent elution study; quantified for extracts derived from 1, 4, 8, 24 and 168 hours elution time points. DOX release increased over the entire elution period (Figure 6.3 (a)) with the 1.4% RC-DEBs releasing the most DOX. Gonzalez et al. [110] performed a DOX release study from sulphonated PVA (s-PVA) hydrogel. Unlike the RC-DEBs in the current study, Gonzalez et al. (32) showed that DOX would elute into plasma and phosphate buffered saline (PBS), but not water, for which they attributed the likely cause as method of drug loading. s-PVA particles bind DOX, post synthesis, via an ion exchange process; the positively charged DOX binds to negatively charge sulphonate groups [99] and the lack of counter ions in water prevents release of DOX from the s-PVA matrix. PLGA:ORP5 based RC-DEBs are loaded with DOX during synthesis so that DOX is embedded within the PLGA matrix, but not actively bound. Since DOX is not bound to the matrix, it can be released into water. Gonzalez et al. (32) showed that DOX release from their embolic agents reached a plateau within 60 minutes in PBS extract media with maximum release approximately equal to 3mg/mL of s-PVA microspheres after 9 days (media was changed three times). This appears to be a much greater release of DOX compared to the RC-DEBs produced herein, but does not account for the difference in DOX loading or that the media was not changed during the elution period. As is common practice, previous studies [110]) report DOX loading and release as mg of DOX per mL of hydrated beads. However, when

DOX loadings are presented as a weight percent of dry s-PVA, Gonzalez loaded 25mg/mL of hydrated beads, which is equivalent to 25wt% of dry beads, compared to the 0-1.4wt% of PLGA load in the current study, much less DOX was available to elute from the RC-DEBs compared to the s-PVA. It is also important to note that DOX loading was determined as a percentage of PLGA not the total mass of the RC-DEBs, which includes ORP5 glass. Therefore, there is significantly less DOX available to elute in the current study, which explains the two orders of magnitude difference in DOX release. Using a T-Cell apparatus Lewis et al. [13] evaluated the elution characteristics of DOX from s-PVA microspheres. Particles were loaded with 100mg/mL of hydrated beads (100wt% of dry beads) and less than 20% of the loaded DOX was released after 22 hours in PBS. In the present study, all RC-DEBs tested showed extended release of DOX up to 168 hours and DOX release was comparable to that of Lewis et al. [13] when loading differences was taken into account. In the current study, the mass of RC-DEBs, not the volume of beads, was held constant. For this reason it is difficult to compare DOX release because the total number of DOX-loaded beads is unknown. To facilitate comparisons between studies it may be more appropriate to use a standard surface to volume ratio for extract production rather than mL of beads used or mass of beads used. Further tests are warranted to assess the full DOX loading capabilities and drug release properties of RC-DEBs over an increased range of loading conditions as well as other possible therapeutic agents (i.e. Irinotecan), in order to evaluate the clinical utility of RC-DEBs.

Cell viability was determined from RC-DEBs extracts tested between 1 and 168 hours. There was a reduction in cell viability of HepG2 cells for DOX containing samples,

though in most cases not statistically significant, compared to the unloaded RC-DEBs (Figure 6.3 (b)). Cell viability was lowest for all DOX containing samples at 24 hours with a value of approximately 70%. Using HepG2 cells, Yu et al. [233] demonstrated cell viabilities of approximately 30% for DOX solutions with a concentration of 1.6μg/mL, which is similar to the DOX concentration from the 24 hour extracts in the present study; however, Yu et al. [233] incubated the cells for 48 versus 24 hours. The greater reduction in cell viability in this study may be due to two possible factors: increased cell exposure time to DOX and testing of fresh DOX solutions [233]. Furthermore, in this study, cell exposure time was 48 hours versus 24 hours in the current study, which may have allowed a greater cytotoxic response to occur. Although outside the scope of this study, stability of the RC-DEBs needs to be investigated further to understand this data. RC-DEB extracts were produced over 1 to 168 hours, therefore some of the released DOX was held for extended periods at 37°C in order to simulate physiological conditions. Such an approach raises an interesting question since the simulated conditions are representative of material response behavior in DEB-TACE and this may have caused reduction in DOX cytotoxicity and/or chemical breakdown of the molecule. This is an important point of note given some of the alternate methodologies deployed in the literature and the conclusions drawn as a result. Stability data taken from previous studies [234],[235] show that DOX is chemically broken down when stored in aqueous solutions. Mayer et al. [234] observed a loss of 60% of the original DOX concentration for solutions stored at 37°C for 140 hours in normal saline and Ioversol. In separate study, a loss of approximately 70% of the original DOX concentration for solutions stored at 40°C for 168 hours in water and Radioselectan® was reported [235]. In the current study,

it was expected that extracts derived from the 1.4wt%-loaded RC-DEBs at the 168 hours elution time point, which had the highest DOX concentration of 2.3μg/mL in the cell culture media, would have the lowest cell viability. Instead, all DOX containing extracts at 168 hours exhibited similar cell viabilities between 85 and 79%. It is unclear why the 168 hours extracts showed higher cell viability than the earlier time points, since there was a greater release of DOX at 168 hours. This may suggest that DOX: (a) may be unstable at the extract conditions over the entire elution period and/or (b) its interaction with individual components in the RC-DEBs may have resulted in reduced cytotoxicity [234, 235]. It may be necessary to evaluate the cell viability of aged solutions with similar concentrations over the same time period in order to understand how exposure to extract conditions may affect cytotoxicity.

6.6 Study Limitations

As with any scientific study, limitations exist. The authors would like to acknowledge the following limitations to the present research:

- A morphological study was not undertaken to determine the location of either the OPR5 glass particles or DOX within the PLGA matrix and therefore the authors assume that both are evenly distributed. A full morphological study is required in order to determine the spatial distribution of ORP5 and DOX within the PLGA.
- Radiopacity was measured on the “as made” RCs, which contained a wide range of particle sizes using CT. An unknown number of radiolucent voids are present, which leads to artificial reduction in the measured radiopacity. Variance in the

particle size distributions between samples can also result in differences in void number and size.

- The efficacy of drug loading is yet unknown as well as the maximum loading potential of this composition. The total drug load in the RC-DEBs after synthesis was not measured; therefore, it was assumed that DOX loading post-synthesis was equivalent to the initial DOX loading. It was clear from the presence of DOX in the PVA solution during synthesis that DOX was lost however this was not quantified.
- RC-DEB drug release profiles in the particle size range of 150-300μm were evaluated herein, since this particle size range represents an intermediate particle size range commonly used in chemoembolization [236, 237]. The effect of particle size on drug loading and subsequent release profiles however, was not evaluated.
- The difference between the adjusted and predicted R-squared terms for the density and radiopacity models is 0.0650 and 0.2096 respectively. While the differences are considered to be within reasonable agreement (within approximately 0.2), an outlier (Composition RC12) within the compositional design space investigated herein is attributable to the larger difference in value obtained with respect of the radiopacity model.

6.7 Conclusion

A DOE approach was successfully used to establish composition-property relationships (radiopacity and density) for RCs comprising PLGA and ORP5. From the resulting

regression models, an optimal formulation was determined that maximized RC radiopacity and was loaded with varying amounts of DOX. The drug release characteristics and efficacy from the RC-DEBs was investigated that successfully demonstrated controlled release of DOX up to 168 hours. The RC-DEBs produced herein may potentially overcome existing limitations for DEB-TACE procedures resulting in improved patient outcomes.

Chapter 7: Unanticipated Stabilization of Zinc-Silicate Glasses by Addition of Lanthanum: Implications for Therapeutic Inorganic Ion Delivery Systems

Nancy Kilcup[1], Ulrike Werner-Zwanziger[2], Elena Tonkopi[3,4], Daniel Boyd[1,4,5]

[1]School of Biomedical Engineering, 5981 University Avenue, Dentistry Building, Dalhousie University, PO BOX 15000, Halifax, NS, Canada, B3H 4R2

[2]Department of Chemistry and Institute for Research in Materials, 6274 Coburg Road Dalhousie University, PO BOX 15000, Halifax, NS, Canada, B3H 4R2

[3]Department of Diagnostic Radiology, Dalhousie University, 1276 South Park Street, PO BOX 9000, Halifax, NS, Canada, B3H 2Y9

[4]Department of Diagnostic Imaging and Interventional Radiology, QEII Health Sciences Centre, Victoria General Hospital, Victoria Building, 1276 South Park Street, PO BOX 9000, Halifax, NS, Canada, B3H 2Y9

[5]Department of Applied Oral Sciences, 5981 University Avenue, Dentistry Building, Dalhousie University, PO BOX 15000, Halifax, NS, Canada, B3H 4R2

This manuscript was written by the candidate (Nancy Kilcup) under the supervision of Dr. Daniel Boyd, who provided guidance and assistance to all aspects of the work. Ms.

Kilcup proposed, designed and conducted all of the experiments described. Dr. Ulrike Werner-Zwanziger provided critical support, training, assistance, and manuscript review concerning the solid state NMR evaluations for Chapter Seven. Dr. Elena Tonkopi conducted the data collection for the CT radiopacity measurements and provided assistance with the manuscript preparation regarding CT radiopacity.

7.1 Abstract

Two series of lanthanum containing zinc-silicate glasses were developed (A: $0.51SiO_2$-$0.29Na_2O$-$(0.20-X)ZnO$-XLa_2O_3, $0 \leq X \leq 0.09$; B: $0.51SiO_2$-$0.35ZnO$-$(0.14-Y)Na_2O$-YLa_2O_3, $0 \leq Y \leq 0.14$). Glasses were characterized in order to examine composition-structure-property-function relationships with a view to their potential use as therapeutic inorganic ion delivery systems. Glasses were melt synthesized and the role of lanthanum was investigated with respect to (i) glass structure based on density, glass transition temperature (T_g) and ^{29}Si MAS-NMR, (ii) the effect on radiopacity (computed tomography) as a function of composition and (iii) the ion release characteristics under simulated physiological conditions. A linear increase in density and T_g was observed with the addition of La_2O_3 to each glass series. Generally, glasses demonstrated a constant molar volume, while density was observed to increase linearly with the addition of La_2O_3. The peak maxima of the ^{29}Si MAS NMR spectra remained relatively unchanged by the addition of La_2O_3 in both glass series, but the line shapes and widths reveal modifications in the local silica structure. Radiopacity increased with La_2O_3: series A ranged between 1770 ± 33 and 6590 ± 89 HU and B Series B ranged between 2340 ± 54 and 9120 ± 290 HU. Series A glasses were observed to release only Na, it was also noted that increased La_2O_3 caused a reduction in Na^+ release. Series B glasses released all constituent glass elements. Interestingly, in series B, La^{3+} concentration decreased over time indicating possible reprecipitation. Based on the structural data, lanthanum does not behave as a traditional network modifier and may in fact act to stabilize the network against degradation by the formation of mixed cation clusters.

7.2 Introduction

Over the last 30 years, bioactive glasses have been used in applications for hard tissue repair and regeneration because these glasses bond directly to bone, which is attributed, in part, to the partial dissolution and recrystallization of ions at the implant surface [25, 130]. Therapeutic inorganic ions (TII) released from these glasses directly impact cellular functions by up-regulating gene expression [131], particularly genes involved with angiogenesis [132-134] and osteogenesis [135-137], both of which are crucial for effective implant integration. The therapeutic effect of different TIIs, summarized in two reviews by Lakhar et al. [22] and Hoppe et al. [23], show that TIIs may modulate and/or improve osteogenesis, angiogenesis and inflammatory responses to bioactive glasses both in vivo and in vitro. Based on these data, a new design philosophy is emerging that aims to trigger specific host responses through localized delivery of TIIs from bioactive glasses [22, 23, 25]. In this context, bioactive glasses have the potential to act as delivery vehicles for a vast number of TIIs in applications outside the area of hard tissue repair and regeneration [138].

In the context of cancer therapy, the design paradigm shifts from one of tissue repair to one where localized tissue damage is the goal. A promising application for TII releasing glasses in cancer therapy is the treatment of hepatocellular carcinoma (HCC). Drug eluting bead-transarterial chemoembolization (DEB-TACE), is a minimally invasive procedure that has emerged as the standard of care for the majority patients with HCC or metastatic colorectal cancer [6]. Briefly, in DEB-TACE chemotherapy, typically

doxorubicin (DOX), is loaded into microspheres composed of either sulphonated polyvinyl alcohol (s-PVA) via an ion exchange mechanism [223] or sodium acrylate/vinyl alcohol copolymer via absorption and ion exchange mechanisms [116]. Under fluoroscopic guidance, a catheter is inserted percutaneously into the femoral artery, and is guided into the blood vessels feeding the tumor. The drug-loaded microspheres are then deployed through the catheter and flow with the blood stream leading to vessel occlusion, causing tumor infarction with concurrent localized delivery of the chemotherapic agent. Presently, the available materials for DEB-TACE are limited by two major factors. Firstly, existing materials are radiolucent, which prevents direct imaging of the particles both during and after the procedure [10, 11]. Secondly, existing particles must be drug-loaded prior to the procedure, which requires significant logistical coordination between the pharmacy and the interventional oncology team to ensure proper drug loading [12, 13]. Once loaded the microspheres have a limited shelf life of four hours at room temperature and 24 hours if refrigerated [14].

To overcome the first of these issues, Sharma et al. proposed that “image-able” microspheres (i.e. radiopaque microspheres) should be developed in order to provide intra-procedural feedback regarding their temporal and spatial distribution in the target tissues. Such information would allow physicians to personalize embolization treatments and ensure optimal embolization and localized chemotherapy delivery [11]. To address the issue of image-ability, Kehoe et al. recently developed a radiopaque zinc-silicate based glass proposed for use in transarterial embolization (TAE) of uterine leiomyomas [18, 19]. However, due to its high temperature synthesis, this glass cannot be loaded with

traditional organic chemotherapies during production. An alternative approach to loading embolic microspheres with traditional chemotherapies is to produce bioactive glasses composed of radiopaque elements, which are also capable of releasing TII's that may permit localized tissue damage. In this way, the bioactive glass would be provided "drug-loaded" thereby eliminating existing logistical issues whilst concurrently extending the shelf life as compared to existing material technologies.

Selection of an appropriate TII within the framework of a DEB-TACE treatment requires that, upon release, the TII will cause cellular damage through either a necrotic and/or apoptotic pathway. Research into new metal-based drugs containing lanthanum is fueled by an increase in cisplatin-resistant cancers and has led to the development of a number of lanthanum-based therapies [238, 239]. This growing body of literature indicates that lanthanum (La^{3+}) is a good target TII for treating a number of different cancers. Soluble lanthanum citrate induces anoikis in human cervical cancer cells line (HeLa) by cleavage of caspase-9, the principal initiator of most apoptosis pathways [195]. In a study using SiHa cells (a human cervical cancer), lanthanum citrate caused apoptosis through an oxidative stress mediated pathway [219]. In a chicken lymphoblastoid cell line, Zhang et al. demonstrated that $LaCl_3$ induced apoptosis reduced the number of cells in G2/M phase, increased the number of cells in G0/G1 phase and also inhibited telomerase activity [198]. Durgo et al. showed that complexation of quercetin with lanthanum increased the cytotoxicity of quercetin as well as its stability [218]. Complexes of lanthanum with natural melophlins have demonstrated significant in vitro cytotoxicity to renal cancer A-498, however the mechanism underlying this observation remains unclear

[239]. Since lanthanum, in a simple salt or organometallic compound, causes cell death in a number of different cancer cell lines, human and animal, it is an excellent target TII for use in HCC.

Kehoe et al. have demonstrated that incorporation of La_2O_3 into zinc-silicate glasses increases radiopacity of embolic particles [19]. In addition, the growing body of literature revealing the anti-cancer properties of lanthanum makes it an excellent target TII for use in bioactive glasses for HCC therapy. However, designing a La^{3+} releasing glass depends on understanding its structural role and impact on ion release. Coon and Shelby suggested that lanthanum behaves as a network intermediate in a sodium-silicate glass, supported by the large increase in glass transition temperature (T_g) with increased La_2O_3 loading [240]. However, in a Na-Ca-Si based glass, Branda et al. concluded that lanthanum behaves as a network modifier due to a shift to lower wavenumbers and broadening of the SiO_4 FTIR peak with La_2O_3 addition [241]. In a borosilicate glass, Molieres et al. showed that La_2O_3 addition caused network depolymerization using Raman spectroscopy. Generally network depolymerization results in increased ion release; unexpectedly Molieres et al. found that La_2O_3 addition slowed dissolution [242]. Schaller et al. demonstrated increased network polymerization with addition of La_2O_3 to Na_2O or K_2O containing silicate glasses, as well as production of O^{-2} species [243]. It is clear that La_2O_3 has an impact on the controlled release of ions from glasses, however the literature pertaining to the impact of La_2O_3 on zinc-silicates is limited.

The aim of this study is to examine the fundamental composition-structure-property-function relationships in a new class of bioactive glasses containing La_2O_3, Na_2O, ZnO and SiO_2 in order to design a bioactive glass capable of controlled release of La^{3+} for use in DEB-TACE. To support this objective, this paper will evaluate the role of lanthanum in a novel quaternary glass system using theoretical structure analysis identified by Brow and Bunker [220]. The theoretical data will be compared to the ^{29}Si MAS-NMR, density and T_g data for glasses in this system as a function of La_2O_3 replacement for either ZnO or Na_2O. In addition, the ion releasing characteristics of the glasses will be determined after exposure to simulated physiological conditions. Finally, the clinical utility of the glasses with respect to diagnostic imaging visualization will be assessed using CT radiopacity. The findings will be used to better understand the fundamental role of lanthanum in zinc-silicates as well as determine if these compositions have potential for use in DEB-TACE.

7.3 Materials and Methods

7.3.1 Glass Synthesis and Processing

Two series of glasses (A and B) were synthesized as in Table 7.1. Briefly, the composition of series A was $0.51SiO_2$-$0.29Na_2O$-$(0.20-X)ZnO$-XLa_2O_3, where $0 \leq X \leq 0.09$. The composition of glass series B was $0.51SiO_2$-$0.35ZnO$-$(0.14-Y)Na_2O$-YLa_2O_3, where $0 \leq Y \leq 0.14$.

Table 7.1: Glass Composition, reported as mole fraction of raw materials used

	Glass ID	SiO_2	Na_2O	ZnO	La_2O_3
Series A	A.1	0.51	0.29	***0.20***	***0***
	A.2	0.51	0.29	***0.1775***	***0.0225***
	A.3	0.51	0.29	***0.155***	***0.045***
	A.4	0.51	0.29	***0.1325***	***0.0675***
	A.5	0.51	0.29	***0.11***	***0.09***
Series B	B.1	0.51	***0.14***	0.35	***0***
	B.2	0.51	***0.0933***	0.35	***0.0467***
	B.3	0.51	***0.07***	0.35	***0.07***
	B.4	0.51	***0.056***	0.35	***0.084***
	B.5	0.51	***0.0467***	0.35	***0.0933***
	B.6	0.51	***0***	0.35	***0.14***

The appropriate mass of each analytical grade reagent: silicon dioxide (SiO_2), sodium carbonate (Na_2CO_3), zinc oxide (ZnO) and lanthanum oxide (La_2O_3) (Sigma Aldrich, Canada) were weighed using an analytical balance and combined in plastic mixing containers. Powders were homogenously mixed for 1 h using a mechanical mixer, packed into a platinum crucible (50 mL) and fired at 1520 °C (Carbolite High Temerature Box Furnace RK-33859-03, Cole Parmer) for 1 h, then quenched, and dried over night at 120

°C. Glass frits were ground using an agate planetary ball mill (Pulverisette 7, Laval Labs Inc., Canada) for 180 seconds and sieved to retrieve particles with the following size ranges: 150-300 μm and <45 μm. The <45 μm powders were subsequently used for basic material characterization. The 150-300 μm fractions were used for experiments with direct clinical relevance (ion release properties and radiopacity) since this range is commonly used during TACE procedures [244].

7.3.2 Characterization of Glass Powders

7.3.2.1 Particle Size Analysis

Particle size distribution was evaluated using a Mastersizer 3000 (Malvern Instruments, Canada). Background measurements of deionized water were used to zero the instrument. Obscuration value was set between 5-8%. The particle size was measured (n=5) using both a blue (λ = 470 nm) and red (λ = 632.8 nm) laser with values reported as the mean diameter (μm) D_{90}, D_{50} and D_{10}, which are particle diameters at 90, 50 and 10% cumulative size by volume, respectively.

7.3.2.2 X-Ray Diffraction

The amorphous nature of each glass was evaluated using x-ray diffraction (XRD). A Bruker D-8 Discover diffractometer equipped with a Vantec-500 area detector and a Cu target X-ray tube was used for XRD measurements. Each powder sample, particle size <45 μm, was pressed into a square, hollow, steel wafer and scanned between $10° \leq 2\theta \leq 95°$ with a step size $2\theta = 0.02°$. Data collection required 3 hours.

7.3.2.3 Helium Pycnometry

The density of each glass was determined using helium pycnometry (AccuPyc 1340, Micromeritics) and reported as the average of 10 measurements. A zero pressure calibration was performed on a 1 mL aluminum chamber insert, which was used for all measurements, followed by a volume calibration using a stainless steel sphere with a known volume of 0.718512 mL. The applied fill pressure was 19.500 psig and the equilibration rate was 0.002 psig/min. Glass samples (<45 μm) were added to the sample chamber until it was approximately ¾ full and the mass was recorded. Before beginning the measurement all samples were put through a fill/purge cycle 10 times in order to remove any trapped air.

7.3.2.4 Differential Scanning Calorimetery

Differential scanning calorimetry (DSC) was performed using a Netzsch Luxx 409 PC to study the thermal properties of each glass. Glasses were heated at 10 °C/min from 30 to 1000 °C. Three individual powder samples (<45 μm) were weighed into a platinum crucible having a mass no greater than 40 mg. The T_g, taken to be the temperature at the inflection point for the only step change observed in the heat flow curve, was determined using Proteus Analysis software (VERSION 5.1.1) and is reported as the average of the three runs per glass composition.

7.3.3 Structural Evaluation of Glasses

7.3.3.1 ^{29}Si MAS-NMR

^{29}Si magic angle spinning nuclear magnetic resonance (MAS NMR) studies were carried out on a Bruker Avance NMR spectrometer with a 9.4 T magnet (79.51 MHz ^{29}Si Larmor frequency) using the probe for 4 mm diameter rotors. The specimens were spun at 5.00 kHz. 200 scans were accumulated with single pulse excitation using a pulse length of 5.24 μs at 28 kHz rf field strength. The recycle delays were chosen to be five times the spin lattice relaxation times as determined by inversion recovery sequences. Spin lattice relaxation times range between 15 and 26 s. The chemical shift scale was referenced externally against Kaolin as secondary chemical shift standard at 91.34 ppm (center between doublet) relative to tetramethylsilane.

7.3.3.2 Brow and Bunker Model

The possible theoretical structures in the glass were modeled using the Brow and Bunker method [220]. Based on this model, glasses are composed of cationic metal ions bonded to anionic oxygen ions and oxygen can have more than two bonds. The bonding requirements of oxygen are satisfied when the sum of all the positive charge of the nearest neighbors is equal to 2, balancing the formal charge of -2 on oxygen. The charge donated by each ion is equal to the formal charge divided by the coordination state, termed the valance unit (VU). The model consists of five rules: 1) the sum of all positive charges coordinating to oxygen cannot be more than 2.2, i.e. 10% greater than the formal charge on oxygen; 2) oxygen net charge, due to coordination with network forming components can be highly negative when network modifiers are present; 3) the structure

of the network forming elements minimizes the anionic nature of oxygen as the network modifier content increases; 4) network modifier cations with greater ionic potential (formal charge/ionic radius; Z/r) will stabilize oxygen that have greater anionic character; 5) oxygen can be coordinated up to a maximum of four times, including network modifying elements.

7.3.4 Quantification of Therapeutic Inorganic Ion Release After Exposure to Simulated Physiological Conditions

All glass samples were processed identically, independent of glass series. Extracts were produce similarly to Tsigkou et al. [230]: 0.1 g of each glass, having a particle size between 150-300 μm (n=3), was immersed in 10 mL (1 % w/v) of sterile tissue culture water (Sigma-Aldrich, Canada) in 15 mL falcon tubes for 1, 4, 7, 14 and 30 days. Each specimen was stored at 37 °C in a shaking water-bath (Stuart Sb40, Techne Inc., USA), and agitated at 2 Hz (longitudinal movement). After each storage period the extracts were sterile filtered through a 0.20 μm filter (Sarstedt, Canada) into 15 mL falcon tubes; all samples were stored at 4 °C until tested. Si^{4+}, Na^{+}, Zn^{2+} and La^{3+} ions released into tissue culture water were quantified using inductively coupled plasma optical emission spectroscopy (ICP-OES) with a Perkin Elmer Optima 8000. Extracts derived from series A were diluted (1/10) using 2 % nitric acid (HNO_3) so that the ion concentrations were below the saturation point of the instrument. Series B glasses were measured without dilution since all ion concentrations were within the sensitivity range of the instrument. In order to eliminate any matrix interference, samples from series A were calibrated with multicomponent standards made in 2 % HNO_3 and series B glasses were calibrated using

multicomponent standards made in tissue culture water. Ion concentrations are reported as the average of three speciments ± standard deviation (SD). All standards were purchased from Perkin Elmer.

7.3.5 Evaluation of Clinically Relevant Parameter: CT Radiopacity

Quantitative CT radiopacity measurements of each glass were determined by taking axial CT scans (1 mm slice thickness, pitch=0.5, 140 kVp) through glass vials using a Somatom Definition Flash Scanner (Siemens Healthcare, Erlangen, Germany). All measurements were performed on the 150-300 μm particle size range, repeated five time,s and radiopacity was reported in Hounsfield Units (HU) ± SD.

7.3.6 Statistical Analysis of Data

One-way analysis of variance (ANOVA) was employed followed by Bonferroni post-hoc test to compare the mean values of density (n=10), T_g (n=3), radiopacity (n=5). Two-way ANOVA was used followed by a Tukey post-hoc test to compare ion concentrations (n=3). Error bars on all graphs represent standard deviation about the mean. Data was considered significant when $p \leq 0.05$. All calculations were done using Prism 6 for Mac OS X (GraphPad Software Inc., La Jolla, USA)

7.4 Results

7.4.1 Characterization of Glass Powders

7.4.1.1 Particle Size Analysis

For completeness the particle size distributions of all glasses used are shown in Table 7.2.

Table 7.2: Particle size distribution for glass series A and B

Glass Series	Glass ID	<45 µm			150-300 µm		
		D_{10}	D_{50}	D_{90}	D_{10}	D_{50}	D_{90}
A	A.1	11.7	28.9	55.9	189	291	439
	A.2	10.8	27.4	53.6	191	298	447
	A.3	11.1	26.9	51.4	180	282	424
	A.4	9.18	27.6	55.8	187	284	420
	A.5	10.9	27.8	54.3	188	288	427
B	B.1	12.38	32.14	61.88	185.4	280.6	414.2
	B.2	9.626	31.4	64.7	190.4	290.4	437.6
	B.3	11.24	32.02	63.42	187.2	286.4	432.8
	B.4	10.146	29.7	59.32	195.8	300.6	451
	B.5	9.378	31.6	69.18	200	318.4	496.8
	B.6	10.22	32.14	69.12	197	299.6	446.2

7.4.1.2 X-Ray Diffraction

The XRD measurements of each glass powder revealed that all compositions displayed diffuse peaks associated with amorphous structures (Figure 7.1). Glasses in series A showed two peaks indicative of two different d-spacing values, i.e. inter-atomic distances, within the glass; only one peak was observed for series B glasses.

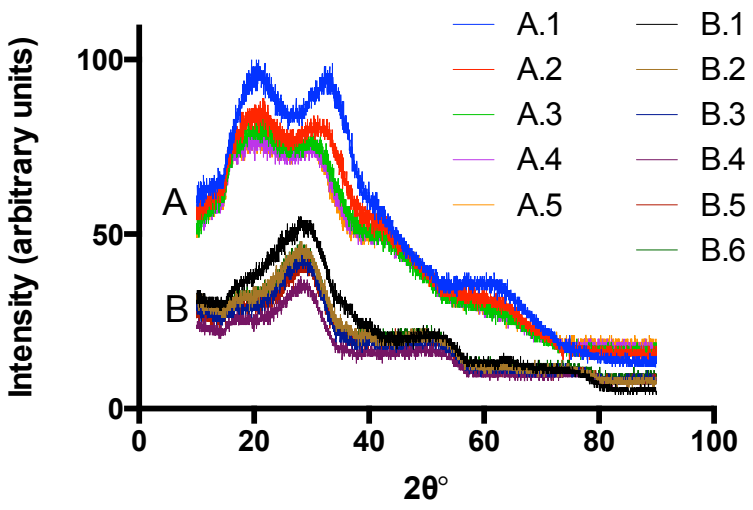

Figure 7.1: Diffractogram of each glass composition.

7.4.1.3 Helium Pycnometery

Density, as measured by helium pycnometry, ranged between 2.91 to 3.44 g/mL for series A and between 3.24 to 4.53 g/mL for series B. Each series demonstrated a linear increase in density with addition of La_2O_3 (Figure 7.2a). Error bars are shown only when larger than the size of the point. This increase was more pronounced for series B than series A, as demonstrated by the greater slope for the linear fit of series B (Table 7.3).

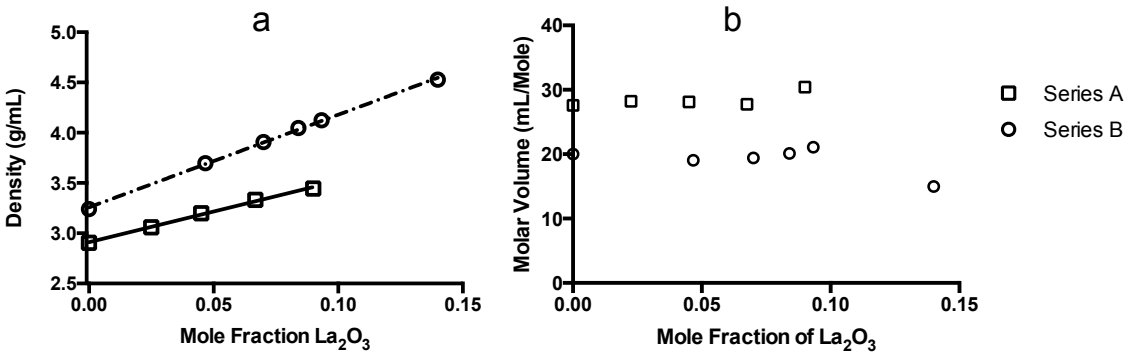

Figure 7.2: The effect of mole fraction La_2O_3 on (a) density and (b) molar volume for glass series A (squares) and B (circles). Standard deviations are shown only when greater than the point size.

Table 7.3: Mathematical description of the impact of La_2O_3 addition on Density, T_g and CT Radiopacity

Property	Series A	**R^2**	Series B	**R^2**
Density (g/mL)	$\rho=6.0\chi+2.1$	0.997	$\rho=9.2\chi+3.3$	0.999
T_g (°C)	$T=514*\chi+490$	0.951	$T=1086*\chi+570$	0.979
Radiopacity (HU)	$Y=1800+7254(1-e^{-11.9\chi})$	0.998	$Y=2310+8818(1-e^{-11\chi})$	0.986

There was a large difference in density between the La_2O_3 free glasses: A.1 (2.91 g/mL) and B.1 (3.24 g/mL). The molar volume of each glass, Figure 7.2b, was calculated using the measured density and the molar mass taken from the compositions outlined in Table 7.1. Molar volume ranged between 27.6 to 30.4 mL/mole for series A and between 20.0

to 15.0 mL/mole for series B. No trend was observed with increasing the mole fraction of La_2O_3. It appears that both series A and B glasses are relatively insensitive to changes in molar volume with increasing La_2O_3 content except for B.6, which had the lowest molar volume and the highest La_2O_3 content.

7.4.1.4 Differential Scanning Calorimetry

T_g ranged from 479 to 543 °C for series A and from 580 to 733 °C for series B. In both glass series, T_g increased linearly with addition of La_2O_3 (Figure 7.3). Error bars are plotted for all data points, but in many cases the error bars are contained within the size of the point. The La_2O_3 free glass in series B has a much higher T_g than the La_2O_3 free glass in series A. Also, the increase in T_g with La_2O_3 addition is more pronounced in series B than the series A, indicated by a greater slope (Table 7.3).

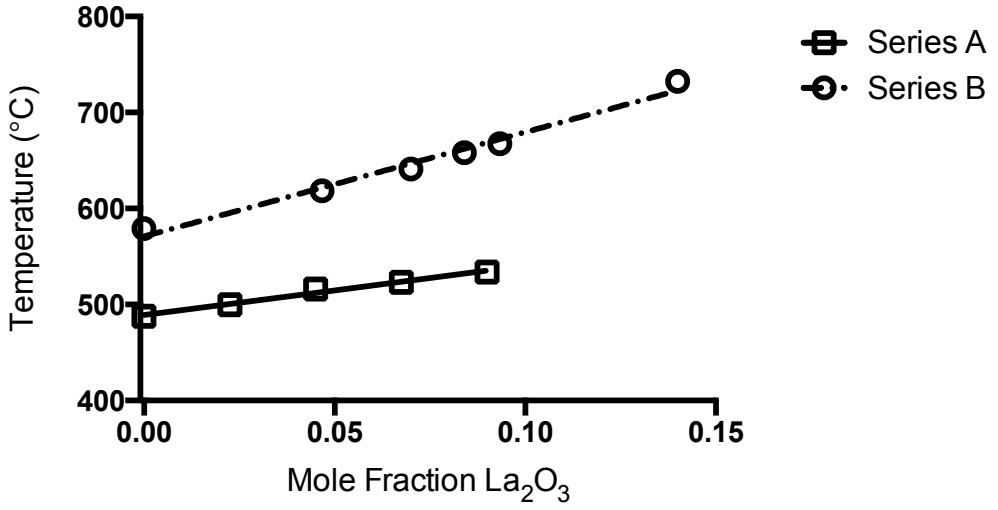

Figure 7.3: The effect of mole fraction La_2O_3 on the glass transition temperature for glass series A (squares) and B (circles). Standard deviations are shown only when greater than the point size.

7.4.2 Structural Evaluation of Glasses

7.4.2.1 ^{29}Si MAS-NMR

The ^{29}Si MAS-NMR spectra for all synthesized glasses are shown in Figure 7.4 with peak positions recorded in Table 7.4. All spectra show small spinning sidebands at approximately 5 kHz separations from the main peak. Generally the peak position shifts towards the positive direction with addition of La_2O_3 (Table 7.4). For glass series A (Figure 7.4a), changes in peak position are caused by a shift in the peak position at half height for both the upfield and downfield side of the peak while the width at half height remains constant with the addition of La_2O_3 (Table 7.4). For series B (Figure 7.4b), the peak position at half height is constant on the downfield side but the upfield side of the peak shifts in the positive direction. This reduces the width at half height, leading to the shift in the peak position at maximum.

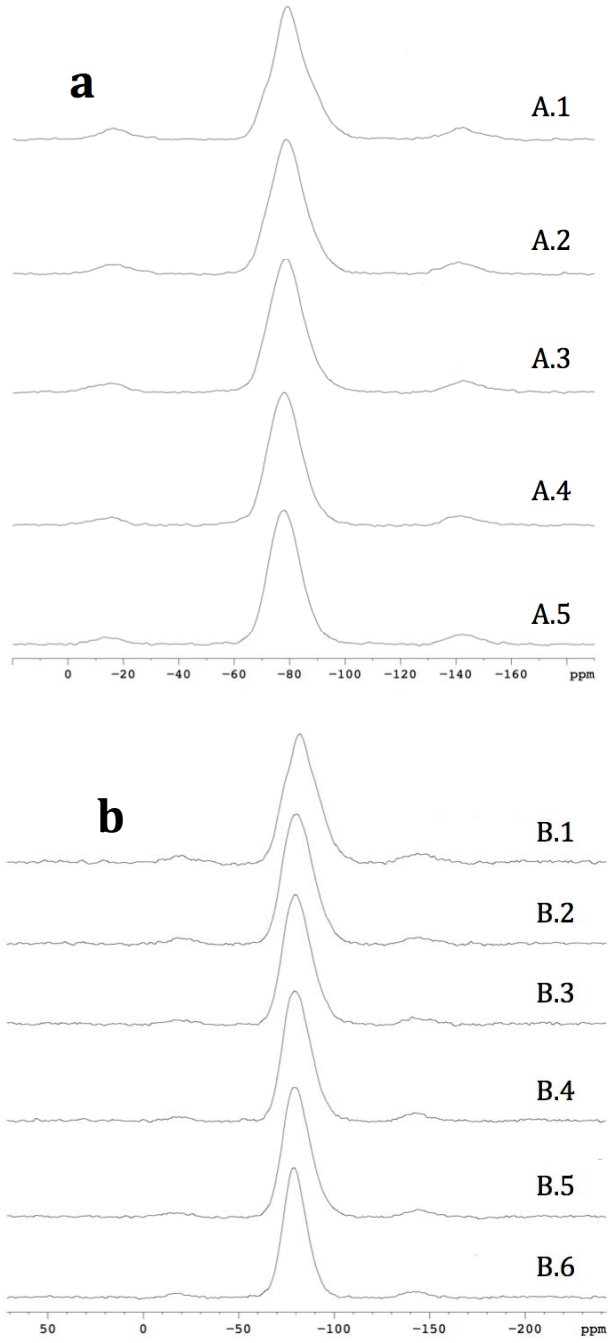

Figure 7.4: ^{29}Si MAS-NMR of each glass in series A (a) and series B (b) series. The mole fraction La_2O_3 increases from A.1 to A.5 and from B.1 to B.5.

Table 7.4: Summarized ^{29}Si MAS-NMR spectra for glass series A and B

		Peak Position (ppm)			**Width at Baseline**	**Width at Half Height**
		Half Height		Maximum		
		Upfield	Downfield			
A	A.1	-87	-73	-79	35	14
	A.2	-86	-72	-79	34	14
	A.3	-86	-72	-80	35	14
	A.4	-85	-71	-78	34	14
	A.5	-85	-71	-78	32	14
B	B.1	-93	-72	-82	46	21
	B.2	-90	-72	-81	40	18
	B.3	-89	-72	-80	40	17
	B.4	-89	-72	-80	37	17
	B.5	-89	-72	-79	39	17
	B.6	-87	-72	-79	34	15

7.4.2.2 Brow and Bunker Model

The theoretical glass structure was evaluated based on the Brow and Bunker model described in section 7.3.3.2 and is independent of glass series since both series A and B contain the same elements. Silicon has a formal charge of +4 and adopts a four coordinate state (Si(4)), therefore donates +1 to each oxygen bond. Zinc with a formal charge of +2 can adopt both tetrahedral and octahedral coordinate states (Zn(4), Zn(6)) donating either +0.5 or +0.33 to each oxygen bond, respectively. Lanthanum has a formal charge of +3

and can adopt 4, 5 or 6 coordination states (La(4), La(5), La(6)) donating either +0.75, 0.6 or 0.5 to each oxygen bond, respectively. Sodium will act as network modifier and was not included in the calculations, however in cases where oxygen carries a net negative charge Na^+ is assumed to coordinate with that oxygen. The model shows that all cation coordination states are allowed when oxygen is coordinated twice. 2Si(4) would be the most stable since this combination completely satisfies the bonding requirements of oxygen. In all other cases the residual charge on oxygen is negative and are allowed since Na^+ is present. When oxygen is coordinated three times the most stable states are expected to be Si(4)-2Zn(4), Si(4)-2La(6) or Si(4)-Zn(4)-La(6) since these states completely satisfy oxygen's bonding requirements based on the model utilized. It may be possible for Si(4)-La(5)-La(6) and Si(4)-2 La(5) to occur, however it would be unlikely due to the small positive residual charge.

7.4.3 Quantification of Therapeutic Inorganic Ion Release After Exposure to Simulated Physiological Conditions

For clarity, the ion release results for glass series A will be presented first followed by series B. Si^{4+}, Zn^{2+} and La^{3+} species were not present in detectable concentrations in any of the extracts prepared from series A, at any time point. Na^+ was released from all glasses in series A (Figure 7.5).

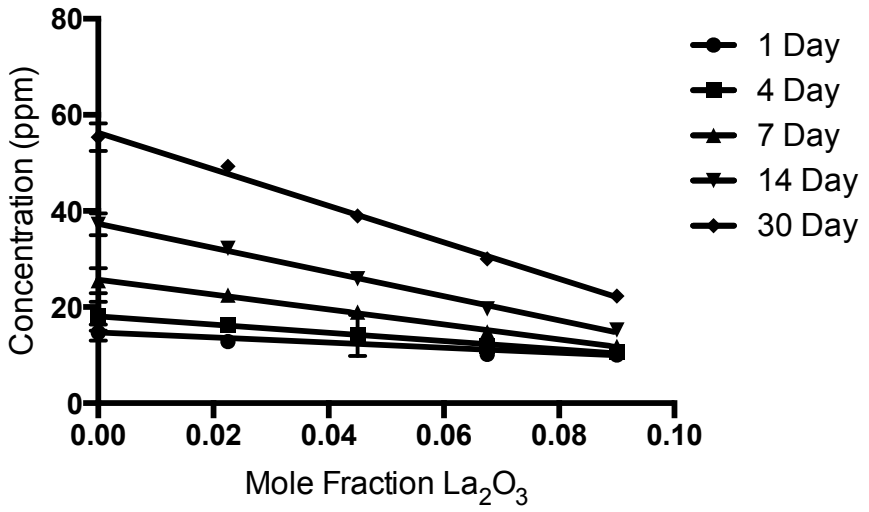

Figure 7.5: Effect of mole fraction of La_2O_3 on sodium release from series A after 1, 4, 7, 14 and 30 days in simulated physiological conditions

Error bars are plotted for all data points, but in many cases the error bars are contained within the size of the data point. From Figure 7.5, addition of La_2O_3 to series A resulted in a linear reduction of Na^+ release as a function of time, with the associated regression analyses provided in Table 7.5.

Table 7.5: Linear fit of sodium release from the glasses from series A

	1 Day	4 Day	7 Day	14 Day	30 Day
Y =	-53.35*X + 14.76	-85.30*X + 18.06	-155.6*X + 25.73	-251.4*X + 37.35	-379.5*X + 56.26
R^2	0.4326	0.8397	0.9538	0.9782	0.9852

Linear regressions of the Na^+ release dependence on mole fraction of La_2O_3 (Table 7.5) demonstrated good fits at all elution times except at 1 day. All series A compositions

demonstrated significantly different Na^+ release from each other at 14 and 30 days. With respect to the temporal release of Na^+ from series A, the following observations were noted:

- Significant increases in Na^+ release was noted, as a function of time, for all series A glasses.
- A.1, A.2 and A.3 demonstrated significant increases in Na^+ release between all time points after 4 days.
- A.4 demonstrated significant increases in Na^+ release between all time points after 7 days.
- A.5 demonstrated significant increases in Na^+ release between all time points after 14 days.

Series B glasses released Na^+, Si^{4+}, Zn^{2+} and La^{3+} (Figure 7.6). Increased elution time resulted in increased release of Na^+, Si^{4+} and Zn^{2+} (Figure 7.6: a, b, c), and decreased La^{3+} release (Figure 7.6: d). Na^+ release from series B (Figure 7.6: a) was more than an order of magnitude lower than that of series A (Figure 7.5).

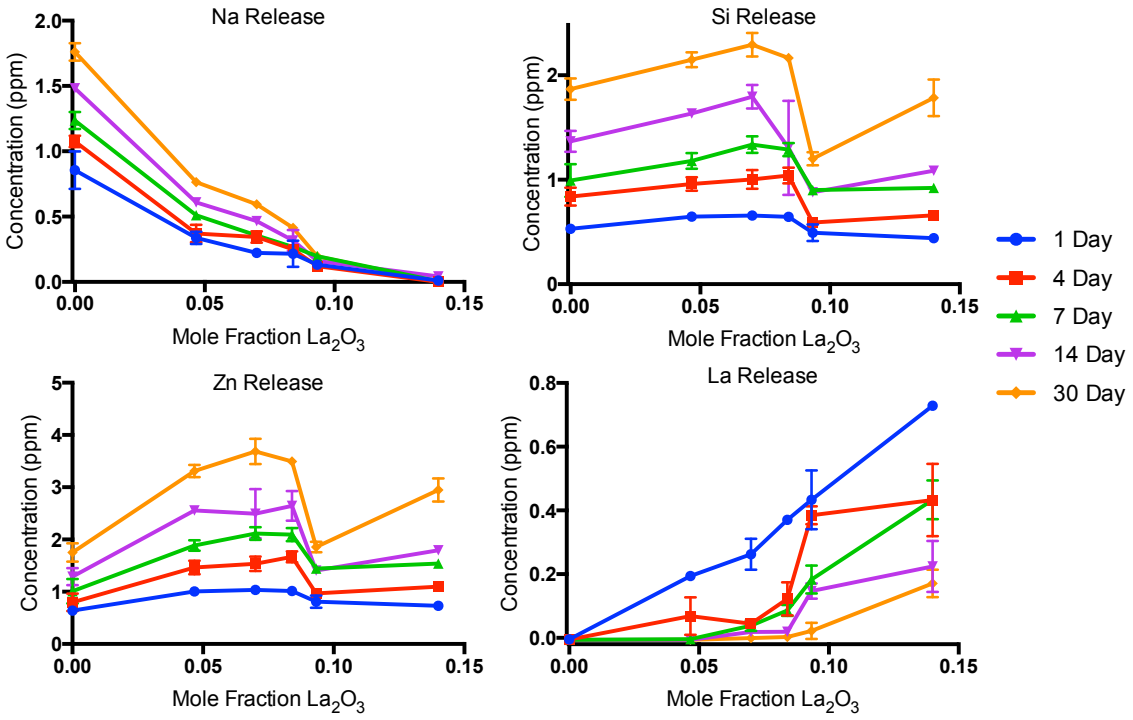

Figure 7.6: Ions released from all glasses from series B as a function of mole fraction La_2O_3: Na, Si, Zn and La. Elution times are as follows: 1 day (blue), 4 day (red), 7 day (green), 14 day (magenta) and 30 day (orange)

As expected there is a reduction in Na^+ release as a function of the increasing La:Na ratio. Counter to the observations of series A, the concentration of Si^{4+} and Zn^{2+} increased with time for all La_2O_3 containing formulations. Past a 1:1 ratio of La:Na there appears to be a stabilization of the glass with respect to Si^{4+} and Zn^{2+} ion release. Unexpectedly, the concentration of La^{3+} ions detected in the supernatant is observed to decrease, as a function of time.

7.4.4 Evaluation of Clinically Relevant Parameter: CT Radiopacity

There was an exponential relationship observed between La_2O_3 addition and increased radiopacity for both glass series (Figure 7.7).

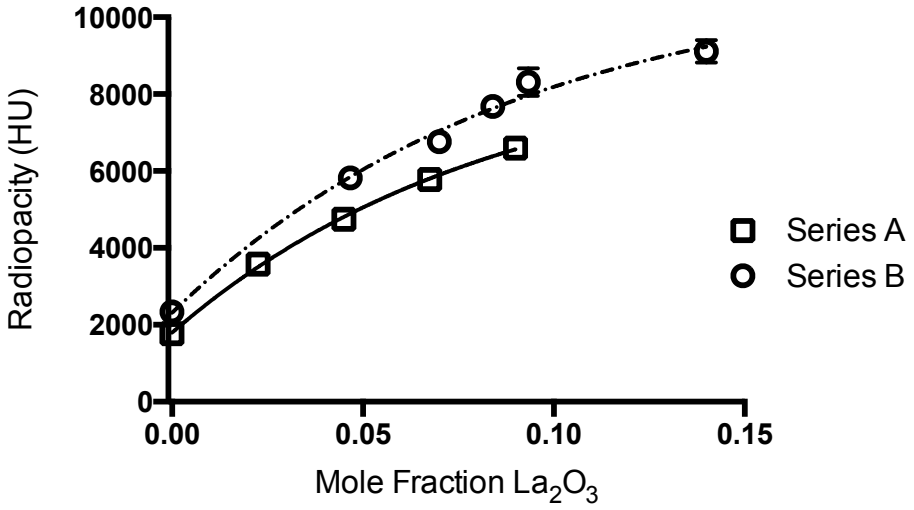

Figure 7.7: Effect of mole fraction La_2O_3 on the CT Radiopacity for glass series A and B

The mathematical models for both series are shown in Table 7.3. The radiopacity of series A ranged between 1770 ± 33 and 6590 ± 89 HU. Series B ranged between 2340 ± 54 and 9120 ± 290 HU. The La_2O_3 free glasses A.1 and B.1 have the lowest radiopacity in their respective series and addition of La_2O_3 causes an increase in radiopacity. Glasses in the series B had higher radiopacity values than the glasses in series A, with similar La_2O_3 additions.

7.5 Discussion

The role of lanthanum on composition-structure-property-function relationships, with

respect to the potential application of these materials as radiopaque, TII delivery systems for transarterial embolization was evaluated for two different glass series. Clues about glass structure can be inferred from changes in physical properties such as density and T_g. Both glass series show linear increases in density and T_g upon addition of La_2O_3 into the glass network in place of either ZnO or Na_2O (Figure 7.2a and 7.3, respectively). Based on the slope of the linear regressions (Table 7.3) La_2O_3 has a greater impact on these characteristics for series B glasses. It is generally accepted that the addition of network modifiers causes an increase in density since it is thought that they occupy interstitial spaces between the network formers [245]. However, the fact that the molar volume (Figure 7.2b) does not change appreciably with increasing La_2O_3 mole fraction shows that the mass effect of La_2O_3 is the principle cause for increased density rather than a change in the structure of the silica network. For the highest La_2O_3 mole fraction studied (i.e., glass B.6 with mole fraction of La_2O_3 0.14), the molar volume drops slightly, which indicates that the glass network has contracted slightly.

Comparing Al^{3+} to La^{3+}, it is expected that the two ions would behave similarly since they have identical charges. In a Na_2O-Al_3O_2-Si_2O glass system Falenty and Webb varied the ratio of Na_2O/Al_3O_2 and demonstrated that increased Al_2O_3 mole fraction resulted in a decrease in T_g, an increase in density and a decrease in molar volume [246]. This is different from the data presented here suggesting that La_2O_3 behavior differs from Al_2O_3. In a CaO-Al_2O_3-SiO_2 glass, Takahashi et al. showed that increasing the Al_2O_3/CaO ratio caused the T_g to increase, density to decrease and molar volume to increase in a glass series where the mole fraction of SiO_2 was constant at 0.5 [247]. This behavior is again

different from the glasses studied herein, which supports the idea that lanthanum behaves differently than aluminum.

Taken in isolation, the increase in T_g with La_2O_3 addition suggests network polymerization. This conflicts with the density data that implies lanthanum is behaving as a network modifier, which typically results in depolymerization of the network. It is not clear, based on these experiments alone, if changes in density and T_g are, in fact, an indication of a change in structure of the glass network. It is possible that the tendency of lanthanum to adopt high coordination numbers, possibly by coordinating to bridging Si-O-Si oxygen atoms, compensates for the introduction of higher charge carriers upon replacing Na_2O or ZnO with La_2O_3, thereby keeping the molar volume constant while still causing a linear increase of T_g.

The ^{29}Si MAS-NMR spectra in Figure 7.4 are typical of silicon in a four coordinate state: a chemical shift of -65 ppm for Q^0 to -110 ppm for Q^4 structures [18, 160, 248]. Peak maxima for all glasses range between -82 to -78 ppm (Table 7.4). Similar changes in peak position have been reported in a number of other glass systems containing lanthanum and other rare earth elements [242, 243, 249]. Peak position reflects the silica bonding environment, where Q^n refers to the number of bridging oxygen atoms surrounding a Si center. Generally higher Q^n leads to greater shielding of the central Si tetrahedron and results in a lower chemical shift. However, this shift strongly depends on the bridging partner and counter ions. Additionally, the line broadening due to structural variations in the glass makes it very difficult to elucidate the Si network structure because

the signals from different sites significantly overlap. In order to identify the effect of lanthanum addition on glass structure it is important to identify the structures present in the glasses. The peak position of the lanthanum-free glasses are -79 ppm (A.1) and -82 ppm (B.1) (Table 7.4), and both glasses display shoulders on the high and low field sides of the ^{29}Si NMR spectra, which are not present in any of the glasses containing lanthanum (Figure 7.4). The peak position for A.1 is more positive, deshielded (i.e. more fragmented), than B.1, suggesting that the increased zinc and reduced sodium content in B.1 may provide for a more polymerized Si network. In an attempt to assign structures to these glasses, it is helpful to look at the chemical shifts of minerals with known structures. Magi et al. identified the chemical shifts for the following sodium silicate minerals with known Si Q^n speciation: $Na_6Si_2O_7$ (Q^1) -68.4 ppm, Na_2SiO_3 (Q^2) -76.8 ppm, and $Na_4Si_4O_{10}$ (Q^3) -94.4 ppm, which shows that as Q^n increases from Q^1 to Q^3, the ^{29}Si chemical shift shifts in the negative direction [250]. Using sodium zincosilicates, Camblor and Davis show that the chemical shift shifts in the negative direction as Q^n increases from Q^0 to Q^3 in the following compounds: Na_2ZnSiO_4 (Q^0, -66.5 ppm), $Na_2ZnSi_2O_6$ (Q^2, -83.8 ppm) and $Na_4Zn_2Si_7O_{18}$:wH_2O (Q^2, -80.2 ppm and Q^3, -91.8, -95.3 and -93.3 ppm)[251]. Based on this work, it is clear that Si centers with the same Q^n speciation can have different chemical shifts, which is due to changes in the next nearest neighbor and differences in bond angle and lengths between adjacent silica tetrahedrons. All of these factors plus the inherent disorder of these same factors in glasses complicates the assignment of ^{29}Si peak positions from MAS NMR. Stebbins identified the peak positions for Q^4, Q^3 and Q^2 structures in sodiumsilicate glasses ($Na_2Si_2O_5$) using static and MAS NMR with the following positions: -100 ppm, -88.5 ppm and -78 ppm,

respectively [252]. Specifically for glasses A.1 and B.1, which contain only Na, Zn and Si, the peak position at maximum is located between the chemical shifts for Q^2 structures from Na_2SiO_3 [250] and $Na_2ZnSi_2O_6$ [251], which indicates that the dominate structures are Q^2 species, as expected from the compositions. The peak positions at half height on the low ppm side are -87 (A.1) and -93 (B.1) ppm; the peak positions at half height on the high ppm side are -73 (A.1) and -72 (B.1) ppm (Table 7.4). Considering the low ppm side first, the NMR signal at -87 ppm (A.1) could be generated from a mixture of Q^2 structures similar to those from $Na_4Zn_2Si_7O_{18}$:wH_2O and $Na_2ZnSi_2O_6$ where the -93 ppm signal (B.1) is more likely due to a combination of Q^3 structures similar to $Na_4Zn_2Si_7O_{18}$:wH_2O [251] and $Na_4Si_4O_{10}$ [250]. The high ppm side of the NMR spectra for A.1 (-73 ppm) and B.1 (-72 ppm) is likely due to the same structures since the chemical shifts are so similar and are likely due to Si with a mixture of Q^2 and Q^1 structures similar to $Na_4Zn_2Si_7O_{18}$:wH_2O (Q^2), Na_2SiO_3 (Q^2) and $Na_6Si_2O_7$ (Q^1).

The peak position at maximum for series A and B exhibited a subtle shift to higher frequencies, implying possible increased fragmentation and/or disruption of the silica network upon introduction of La_2O_3. The shift in peak position is greater in series B than series A and since the peak shifts are not very large it is unlikely that lanthanum dramatically alters the Q^n speciation of the Si network. The shift in peak position of series A is symmetrical since the width at half height is constant (Table 7.4). Series B glasses show peak narrowing due to the upfield side of the peak shifting in the positive direction while the downfield side remains constant, which indicates that the more shielded Si species (Q^3) are preferentially affected by La_2O_3 addition. In alkali-silicate glasses with a

constant NBO/tetrahedral ratio, Schaller et al. observed the opposite behavior with La_2O_3 addition. The Q^4/Q^3 ratio increased without a subsequent increase in Q^2 species, which they attributed to network polymerization and production of free oxygen species (O^{-2}) that are associated with La^{3+} [243]. In borosilicates, Angeli et al. observed a negative shift in the peak position in the ^{29}Si MAS NMR, network polymerization, and peak broadening, with increased La_2O_3 [253]. In this same study, Angeli et al., ^{17}O MAS NMR spectra revealed an increased variability in the next nearest neighbor sites for Si and no free oxygen anions were observed. The nearest and next nearest neighbors surrounding lanthanum were investigated using extended x-ray fine absorption structure (EXFAS), which showed that approximately 6 NBO surrounds each lanthanum when in the presence of sodium and calcium causing mixed cation clustering. The authors indicate that peak broadening in the ^{29}Si NMR is due to the many variations of cation clusters of the next nearest neighbors to Si and not to polymerization of the Si network [253]. In the context of the current study, La_2O_3 addition to glass series A does not alter the nature of the silica network since there is very little change in ^{29}Si peak position or symmetry. As La_2O_3 is substituted into the glass at the expense of ZnO, series A, mixed cation clustering may occur where some portion of sodium previously modifying the silica network may now be associated with La_2O_3. In the case of the glass series B, the ^{29}Si peak is more shielded than in series A and narrows from the more highly shielded Si centers (Table 7.4) as La_2O_3 replaces Na_2O in the glass formulation.

In an attempt to evaluate the likelihood of possible structures occurring in the glasses, the components that make up each glass series were modeled following the methods of Brow

and Bunker [220]. Since oxygen is allowed to be coordinated up to four times, this model provides more flexibility in the arrangement of the network as compared to Zachariasen's model [148]. Although allowed by the model, it is very unlikely that oxygen would be coordinated four times because the allowed states require La-O-La or Zn-O-Zn bonds, which break the extended Loewenstein rule developed by Camblor and Davis [251] and this holds with the work of Angeli et al., where ^{17}O NMR did not show La-O-La structures in a lanthanum containing borosilicates [253]. Oxygen coordinated three times has many allowable configurations; the most likely being structures ones containing Si(4) and any combination of two Zn(4) and/or La(6) since the formal charge on oxygen is completely neutralized. The most likely of these would be Si(4)-Zn(4)-La(6), since this is consistent with the extended Loewenstein rule. From a compositional perspective, it may very well be possible to have La-O-Zn structures where relatively large amounts of both La and Zn are present. This probability further increases when large amounts of Na are present to charge compensate La-O-Zn structures. Linati et al. have shown that it is possible for oxygen to coordinate three times since Zn_2SiO_4 is composed of 2Zn(4) and one Si(4) that share an oxygen, which supports the model's prediction that three coordinated oxygen may exist in glasses containing Si-La-Zn-Na [254]. When oxygen is coordinated twice, all of the combinations modeled are allowed, but only 2Si(4) completely satisfies oxygen's bonding requirements. In every other case sodium is required to compensate for the remaining negative charge on oxygen. Taking all of this data together, the glasses studied herein most likely contain a combination of two- and three-fold coordinated oxygens associated with zinc and lanthanum that is charge

compensated by sodium. This supports the general Q^2 structure as determined from the ^{29}Si MAS NMR.

To further substantiate the existence of two- and three-fold coordinated oxygens associated with zinc and lanthanum, charge compensated by sodium within series A and B, it is instructive to examine the La-Si literature. Using EXFAS to examine the lanthanum structure in sodium and calcium containing borosilicate glasses, Molières et al. determined that lanthanum is surrounded by six non-bridging oxygens with a mixture of sodium and calcium, indicating that lanthanum adopts an octahedral coordination [242]. However, it is possible for lanthanum to adopt higher coordination states. In lanthanum alumosilicates apatite systems Kahlenberg and Krüger showed that lanthanum coordinates to 7-8 oxygen atoms [255] and in borosilicate glasses lanthanum coordination changes from 6 to 9 after exposure to water [242]. Coordination of Zn^{2+} in a ZnO-Na_2O-SiO_2 series of glasses was shown to be tetrahedral when there was a high percentage of SiO_2 (75 mole %), however when the SiO_2 content was low (< 50 mole %) the presence of octahedral zinc sites were observed [256]. In crystalline zinc-silicates, tetrahedral coordination of zinc is stabilized by high field strength cations and octahedral coordination is stabilized by lower field strength cations [257], therefore tetrahedral zinc is the more likely configuration in this glass system due to the presence of the high field strength lanthanum. The Brow and Bunker model shows that the majority of allowed states require compensation via a network modifier. Therefore, series A and B glasses will most likely form lanthanum and zinc charge compensated clusters within there respective networks. Evaluating the ^{29}Si NMR data in light of the Brow and Bunker

model suggests that sodium, which typically modifies the silica network, is reallocated to form mixed cation clusters with both lanthanum and zinc. In this way, some portion of NBOs due to sodium would be replaced by NBOs due to mixed cation clusters containing lanthanum and zinc. From the perspective of the Si network, there may not be a net change in the number of NBO and therefore little change would be observed in the ^{29}Si NMR. Viewing the T_g data along side the ^{29}Si NMR spectra, which shows little change in the ratio of BO to NBO, it is unlikely that increased T_g is due to changes in the silica bonding arrangement and more likely due to changes in the bonding arrangement around lanthanum and zinc.

Glass structure has a major impact on ion dissolution kinetics in simulated physiological environments. Generally, glasses comprising a large portion of network modifying agents have an increased NBO/BO ratio and tend to release more ions than glasses composed of mainly network forming agents [258, 259]. Based on this information, the glasses in series A and B were anticipated to be susceptible to degradation when exposed to water. Surprisingly, glasses in series A only released Na^+, and a linear reduction in Na^+ release with increasing La^{3+} composition (Figure 7.5) was observed as a function of time. This suggests that lanthanum is not behaving as a traditional network modifier, but rather polymerizes the network by sequestering sodium from a modifying role and further supports the idea of mixed cation clustering. There is evidence to support such an assertion, in La_2O_3 enriched borosilicate glass series, Molières et al. attributed network stabilization to the formation of highly anionic environments around lanthanum, which must be charge compensated by network modifiers, effectively limiting hydrolysis [242].

This would increase the network connectivity but not change the ^{29}Si NMR (Figure 7.4) significantly and is an allowed state from the Brow-Bunker model. The unexpected stability of A.1 to hydrolytic degradation may be attributed to zinc behaving as a network former, when charge compensated by sodium. Replacing ZnO with La_2O_3 in series A causes further stabilization, similar to that observed by Molières et al. by lanthanum and sodium forming cation clusters.

Glasses in series B released Si^{4+}, Zn^{2+}, Na^{+} and La^{3+} (Figure 7.6), although an order of magnitude less Na^{+} than series A glasses. The reduced ion release indicates that B.1 is a more stable glass than A.1, likely due to the reduced amount of network modifier (Na_2O) and the higher amount of ZnO. Linati et al. demonstrated that ZnO addition to a bioactive glass increased its durability due to ZnO copolymerizing with SiO_2 thereby behaving as a network former [254], which explains the reduction in total ion release from series B glasses. In series B, increased La_2O_3 loading initially resulted in an increase in ion release for Si^{4+}, Zn^{2+} and La^{3+}; however, when the glass contained more La_2O_3 than Na_2O, ion release for Si^{4+} and Zn^{2+} was reduced, suggesting a potential switch in the function of lanthanum in the glass. In boroaluminosilicate, Zheng et al. noted that when the Al/Na mole fraction was below 1, aluminum was present in the glass in a tetrahedral coordination. When the Al/Na mole fraction was greater than 1 some portion of aluminum converted to 5-fold coordination [260], which would stabilize the glass from hydrolytic degradation. The reduction in Si^{4+} and Zn^{2+} release from series B occurs when the La/Na ratio was greater than 1, which may indicate that there is a switch in the coordination state of lanthanum when sodium is unavailable to charge compensate. Zn^{2+}

and Si^{4+} release curves have almost identical dependence on the mole fraction of La_2O_3 in the glass, suggesting that zinc and silica are bound together within the glass structure and are therefore released together. Na^+ release decreased with La_2O_3 addition, unsurprisingly since Na_2O was replaced with La_2O_3. As expected, increased La_2O_3 mole fraction resulted in increased La^{3+} release, but the temporal release showed that the initial La^{3+} concentrations for each glass decreased with time. It is unclear what happens to the released La^{3+} in the series B. It may form a layer on the surface of the glass particles similar to the borosilicate glasses investigated by Molières et al. who noted that lanthanum, coordinated 9 times, was enriched at the interface with extract media [242]. Substitution of lanthanum into soda-zinc-silicates causes little change in the structural arrangement of the Si network, by ^{29}Si NMR, but it does greatly impact density and T_g. The role of lanthanum does not appear to be as simple as network modifier or network former in the traditional sense of producing BO or NBO. It appears that lanthanum may be able to produce more NBO while simultaneously increasing the stability of the glass against hydrolytic degradation. It is clear from the data that the zinc-silicate systems studied herein are not suitable for the vectored delivery of lanthanum for the treatment of HCC. However, the observed stabilization of the glass network, by the inclusion of La_2O_3 may unlock a mechanistic approach for the controlled degradation of glassy systems that currently exhibit insufficient persistence under physiological conditions.

The CT radiopacity (Figure 7.7) of these potential embolic materials increased with La_2O_3 addition: glass series A ranged between 1700-6600 HU and series B ranged between 2300-9100 HU. For similar La_2O_3 additions series B had higher corresponding

radiopacity values. This is most likely due to the greater amount of ZnO in series B, which has been shown to impact radiopacity [19] . All compositions except A.1 and B.1 had radiopacity values higher than 2520 HU, which is the radiopacity of 50:50 strength contrast Isovue® 370, a common contrast agent used in interventional radiology [19]. As yet, an ideal radiopacity has not been identified in the literature, so it is difficult to identify an exact radiopacity for DEB-TACE procedures. However, Kehoe et al. demonstrated that radiopaque zinc-silicate microspheres with a radiopacity of 7050 HU [225] are visible during a TAE procedure and provide for post procedure imaging in Yucutan miniswine [20]. In the current study, glasses in series B were able to achieve similar radiopacity values as Kehoe et al. [225] and are therefore expected to provide clinically relevant radiopacity levels that will provide for intra-procedural visualization. Advancement in particle visualization will help make it possible to provide real-time, intra-procedure feed back to physicians in order to personalize embolization procedures [11]. Addition of La_2O_3 to the glass composition offers predictable control over radiopacity. A range of radiopacities can be achieved by addition of La_2O_3, although each addition causes a subsequent increase in the density, which Kehoe et al. have indicated could be a limitation of these materials because it could make particle deliverability difficult using the current methods [18].

7.6 Study Limitations

As with any scientific study, limitations exist and the authors would like to acknowledge the following limitations:

- The effect of La_2O_3 addition on the glass structure was not evaluated in a ZnO-free system, which may provide some information concerning possible interactions between zinc and lanthanum in silicate glasses. Substitution of La_2O_3 for ZnO in series A was not stoichiometric. The mole fraction of ZnO was replaced with an equal mole fraction of La_2O_3. In series B, substitution of La_2O_3 for Na_2O, although stoichiometric, the total charge in the glass was not constant.

- All direct structural information came from the ^{29}Si NMR spectra, which only provides information about the local ^{29}Si environment, which is very difficult to elucidate with featureless spectra. It may be beneficial to perform ^{17}O MAS NMR studies along with EXFAS, enabling direct investigation into the bonding environment around oxygen, zinc and lanthanum.

- The study assumes the following charges for ionic species detected using ICP-OES: Na^+, Zn^{2+}, La^{3+} and Si^{4+}.

7.7 Conclusion

Two different series of zinc-silicate glasses were successfully synthesized and characterized. Lanthanum does not appear to alter the Si network significantly in either glass series, based on ^{29}Si MAS NMR. A linear increase in density and T_g with La addition has been attributed to the greater molecular weight of La_2O_3 than Na_2O or ZnO. La_2O_3 increases the stability of the glass to hydrolytic degradation in simulated physiological environment, which caused a reduction in ion release. Based on the

structural, physical and chemical evaluation, it appears that lanthanum may adopt a higher coordination state in the glasses, which facilitates mixed cation clustering, thereby preventing hydrolytic degradation. Predictable increases in radiopacity were observed with increased La_2O_3 content; however, the poor ion releasing ability of glass series A and B precludes using these glasses for localized TII delivery for DEB-TACE. Knowing that lanthanum has the ability to retard ion release it is a good target element for incorporation into highly degradable glasses, thus increasing their biocompatibility by providing a mechanism for controlling their degradation properties.

Chapter 8: Stimulation of Apoptotic Pathways in Liver Cancer Cells: An Alternative Perspective on the Biocompatibility and Utility of Biomedical Glasses

Nancy Kilcup[1*], Sean Gaynard[2*], Ulrike Werner-Zwanziger[3], Elena Tonkopi[4,5], Jessica Hayes[2], Daniel Boyd[1,4,6]

[1]School of Biomedical Engineering, 5981 University Avenue, Dentistry Building, Dalhousie University, PO BOX 15000, Halifax, NS, Canada, B3H 4R2

[2]Regenerative Medicine Institute, Bioscience Research Building, National University of Ireland Galway, Galway, Ireland

[3]Department of Chemistry and Institute for Research in Materials, 6274 Coburg Road Dalhousie University, PO BOX 15000, Halifax, NS, Canada, B3H 4R2

[4]Department of Diagnostic Imaging and Interventional Radiology, QEII Health Sciences Centre, Victoria General Hospital, Victoria Building, 3rd Floor, North Wing, 1276 South Park Street, PO BOX 9000, Halifax, NS, Canada, B3H 2Y9

[5]Department of Diagnostic Radiology, Dalhousie University, 1276 South Park Street, PO BOX 9000, Halifax, NS, Canada, B3H 2Y9

[6]Department of Applied Oral Sciences, 5981 University Avenue, Dentistry Building, Dalhousie University, PO BOX 15000, Halifax, NS, Canada, B3H 4R2

Corresponding Authors:

Dr. Jessica Hayes & Dr. Daniel Boyd.

jessica.hayes@nuigalway.ie / d.boyd@dal.ca

**** Joint first authors***

This manuscript was written by the candidate (Nancy Kilcup) under the supervision of Dr. Daniel Boyd, who provided guidance and assistance to all aspects of the work. Ms. Kilcup proposed, designed and conducted all of the experiments described, with the exception of the flow cytometry panels provided in Chapter Eight, which was designed and performed in collaboration with Seán Gaynard at the National University of Ireland Galway. Dr. Ulrike Werner-Zwanziger provided critical support, training, assistance, and manuscript review concerning the solid state NMR evaluations for Chapter Eight. Dr. Elena Tonkopi conducted the data collection for the CT radiopacity measurements and provided assistance with the manuscript preparation regarding CT radiopacity experiment. As co-first author of the manuscript in Chapter Eight, Ms. Kilcup prepared the manuscript with significant assistance from Seán Gaynard and his supervisor Dr. Jessica Hayes. All co-authors reviewed the respective manuscripts and provided critical feedback.

8.1 Abstract

A host of research opportunities with innumerable clinical applications are open to biomedical glasses if one considers their potential as therapeutic inorganic ion (TII) delivery systems. Generally, applications have been limited to repair and regeneration of hard tissues while compositions are largely constrained to the original bioactive glass developed in the 1960's. However, in oncology applications the therapeutic paradigm shifts from repair to targeted destruction. With this in mind, the composition-structure-property-function relationships of vanadium containing zinc-silicate glasses ($0.51SiO_2$-$0.29Na_2O$-$(0.20-X)ZnO$-XV_2O_5, $0 \leq X \leq 0.09$) were characterized in order to determine their potential as TII delivery systems. Increased V_2O_5 mole fraction resulted in a linear decrease in density and T_g. ^{29}Si MAS NMR peak maxima shifted upfield while ^{51}V MAS NMR peak maxima was independent of V_2O_5 content and overlapped well with the spectra $NaVO_3$. Increase V_2O_5 mole fraction caused an increase ion release. When human liver cancer cells, HepG2, were exposed to these ions they demonstrated a concentration dependent cytotoxic response, mediated by apoptosis. This work demonstrates that the zinc-silicate system studied herein is capable of delivering TIIs at concentrations that induce apoptotic cell death and provide a simple means to control TII delivery.

8.2 Introduction.

The range of applications for glass-based biomaterials is obvious when one considers both (i) the definition of 'biocompatibility' (defined by Black as the ability of a material to perform with the appropriate host *and* material response in a particular application[145]) and (ii) the increasing evidence that controlled release of inorganic ions can mediate a broad range of specific host responses[261]. Complementary to this perspective, glass networks provide almost limitless permutations of composition, structure and property that can be engineered to control the physiological degradation such that appropriate levels of therapeutic inorganic ions (TIIs) are released [23, 169].

The potential of glass networks to provide controlled release of TIIs has been long recognized. However, research has been largely circumscribed by the almost exclusive and ubiquitous development of bioactive glass systems designed for applications in bone repair and regeneration that are still largely based on the original bioglass formulation Na_2O-CaO-P_2O_5-SiO_2[24]. Consequently, this limits the potential applicability of biomedical glasses, while concurrently constraining the compositional palettes under development and investigation. The scope and applicability of biomedical glasses created for clinical utility beyond hard tissue repair is rich in research opportunities for innumerable clinical applications.

One area where TII release may yield substantial benefit is in oncology, particularly in the field of transarterial chemoembolization (TACE). Interventional radiologists perform TACE using fluoroscopic guidance to treat hypervascularized tumors (e.g. hepatocellular

carcinoma and metastatic colorectal cancer in the liver) after detailed angiographic assessment of the tumor vasculature. Briefly, and at the most fundamental level, a TACE procedure involves transcatheter delivery of chemotherapy directly into the blood vessels supplying a tumor followed immediately by embolic particles, thereby occluding the vessels and trapping the chemotherapy within the tumor vasculature[8]. This approach results in tumor tissue infarction and localized chemotherapy delivery[262, 263].

Currently there are two major drawbacks to this procedure. The first is that the embolic particles, based on polyvinyl alcohol or trisacryl gelatin, are radiolucent and therefore cannot be visualized using fluoroscopy; consequently physicians are unable to directly monitor embolic microspheres during the procedure[11]. The second is that the systemic concentration of the chemotherapy increases dramatically post procedure[116], indicating that a significant fraction of the chemotherapy does not remain sequestered in the tumor vasculature and therefore does not provide optimal localized delivery. The inability to visualize particles during embolization "preclude[s] ideal spatial delivery" and limits the accurate assessment of the terminal locations for the embolic beads[11]. It has been pointed out[11], that the provision of an intrinsically radiopaque embolic microsphere for TACE would (i) define the true spatial distribution of embolic materials in a target tissue, (ii) provide real-time intra-procedural feedback, (iii) optimize, personalize and improve TACE techniques and, (iv) consequently standardize material choice and procedural technique with a high degree of confidence. To overcome these limitations, 'visible' (i.e. radiopaque) glass microspheres have been developed for embolization procedures [19]. These glass spheres are multicomponent in nature and permit direct intra-procedural

feedback, thereby ameliorating the limitations of existing technologies.

To address the issue of rapid release of the chemotherapy, drug loadable embolic particles with extended release properties have been developed[110]. However, as these particles are based on polymer hydrogels, they are radiolucent and therefore suffer from the same visibility limitations as other polymer based embolic agents. Also, the existing particles must be drug-loaded immediately prior to the procedure, requiring significant coordination between the pharmacy and the oncology team [12, 13]. Once loaded the microspheres have a limited shelf life of up to 24 hours[264]. More importantly, drug loading causes changes to the particles physical properties: the particle size and water content decrease and particles become resistant to compression[93]. A compounding problem is that once the drug is released in vivo further changes to these same physical properties may occur, which is currently unknown, and could contribute to suboptimal therapy [124]. Glass systems offer the ability to overcome these limitations since they can be provided “drug preloaded” with TIIs, eliminating the loading step and the associated alterations in physical properties. Critically, the vectored delivery of TIIs from glass networks for oncology represents the next evolution of this concept and to realize this, the composition-structure-property relationships of glass networks comprising potentially therapeutic agents must be evaluated.

Vanadium based salts and organometallic compounds possess excellent properties against particular cancers and cancer cell lines, including reduced tumor growth and prevention of metastatic growth[212]. The mechanisms for this are largely unknown, however the

following has been identified. Soluble ammonium monovanadate (NH_4VO_3) causes apoptosis in MCF7 breast cancer cell lines[215] whilst elsewhere sodium metavanadate ($NaVO_3$(aq)) can prevent cell proliferation in the human prostate cancer cell line (PC-3) by production of reactive oxygen species (ROS)[214]. In order to expand the compositional palette and applications of biomedical glasses, this paper considers the composition-structure-property-function relationships for a series of new glass compounds containing Zn-Si-Na-V as it pertains to materials response (release of therapeutic load) and host response (apoptotic cell death in cancer cells) with a view to expanding the field of biomedical glass discovery and innovation for TACE.

8.3 Materials and Methods

8.3.1 Glass Synthesis and Processing

Glasses were synthesized as per Table 8.1. All glasses contain the same amount of SiO_2 and Na_2O with V_2O_5 substituting for ZnO across the series. The vanadium free glass (VG0) was synthesized by weighing out the appropriate mass of each reagent: silicon dioxide (SiO_2), sodium carbonate (Na_2CO_3), zinc oxide (ZnO) and vanadium pentoxide (V_2O_5) (analytical grade reagents, Sigma-Aldrich, Canada) using an analytical balance. Powders were homogenously mixed in a plastic container for 1 hour using a mechanical mixer, packed into a platinum crucible (50 mL) and fired at 1520 °C (Carbolite High Temerature Box Furnace RK-33859-03, Cole Parmer) for 1 hour, quench cooled in room temperature water and dried overnight at 120 °C. Due to the safety concerns arising from the use of V_2O_5, all vanadium-containing glasses (VG1-VG4) were synthesized at a specialist facility by Ceredine Viox, (Seattle, WA) using an identical protocol to that used

for VG0. All glass frits were ground using agate planetary ball mill (Pulverisette 7, Laval Labs Inc., Canada) and sieved to retrieve particles with the following sizes: <45 μm and 150-300 μm.

Table 8.1: Composition of vanadium containing glasses based on oxide mole fraction

Glass Name	SiO_2	Na_2O	ZnO	V_2O_5
VG0	0.51	0.29	0.20	0
VG1	0.51	0.29	0.1775	0.0225
VG2	0.51	0.29	0.155	0.045
VG3	0.51	0.29	0.1325	0.0675
VG4	0.51	0.29	0.11	0.09

8.3.2 Physical and Chemical Characterization of Glasses

The particle size distributions and amorphous nature of the glasses were determined for the purposes of reproducibility and repeatability. In order to establish composition-property relationships, helium pycnometery and differential scanning calorimetry were used to evaluate the density and glass transition temperature (T_g) for each glass.

8.3.2.1 Particle Size Analysis

Particle size distribution was evaluated using a Mastersizer 3000 (Malvern Instruments, Canada). Background measurements of deionized water were used to zero the instrument. Obscuration value was set between 5-8%. The particle size was measured (n=5) using both a blue (λ = 470 nm) and red (λ = 632.8 nm) laser with values reported as the mean diameter (μm) D_{90}, D_{50} and D_{10}, which are particle diameters at 90, 50 and 10%

cumulative size, respectively.

8.3.2.2 X-Ray Diffraction

A Bruker D-8 Discover diffractometer equipped with a Vantec-500 area detector and a Cu target X-ray tube was used for X-Ray Diffraction (XRD) measurements. Each powder sample, particle size <45 μm, was pressed into a square, hollow steel wafers and scanned between $10° \leq 2\theta \leq 95°$ with a step size $2\theta = 0.02$.

8.3.2.3 Helium Pycnometry

The density of each glass (n=10) was determined using helium pycnometry (AccuPyc 1340, Micromeritics) and reported as the average ± standard deviation (SD). A zero pressure calibration was performed on a 1 mL aluminum chamber insert, which was used for all measurements, followed by a volume calibration using a stainless steel sphere with a known volume of 0.718512 mL. The applied fill pressure was 19.500 psig and the equilibration rate was 0.002 psig/min. Glass samples (<45 μm) were added to the sample chamber until it was approximately ¾ full and the mass was recorded. Before beginning the measurement all samples were put through a fill/purge cycle 10 times in order to remove any trapped air.

8.3.2.4 Differential Scanning Calorimetry

Differential scanning calorimetry (DSC) was performed using a Netzsch Luxx 409 PC to study the thermal properties of each glass. Glasses were heated at 10 °C/min from 30 to 1000 °C. Powder samples (n=3, <45 μm) were weighed into a platinum crucible having a

mass no greater than 40 mg. The T_g, taken to be the temperature at the inflection point for the step change in the heat flow curve, was determined using Proteus Analysis software (VERSION 5.1.1) and is reported as the average ± SD.

8.3.3 ^{29}Si and ^{51}V Nuclear Magnetic Resonance Spectroscopy

^{29}Si NMR: ^{29}Si magic angle spinning (MAS) nuclear magnetic resonance (NMR) studies were carried out on a Bruker Avance NMR spectrometer with a 9.4 T magnet (79.51 MHz ^{29}Si Larmor frequency) using a probe head for 4 mm rotor diameters. The specimens (VG0-VG4, particle size <45 μm) were packed into the rotor and spun at 5.00 kHz. 200 scans were accumulated with single pulse excitation using a pulse length of 5.24 μs at 28 kHz rf Field strength. The recycle delays were chosen to be five times the spin lattice relaxation times as determined by inversion recovery sequences. Spin lattice relaxation times range between 15 and 26 s. The chemical shift scale was referenced externally against Kaolin as secondary chemical shift standard at 91.34 ppm (center between doublet) relative to tetramethylsilane.

^{51}V NMR: ^{51}V MAS NMR studies were carried out on a Bruker Avance NMR spectrometer with a 16.4 T magnet (184.19 MHz ^{51}V Larmor Frequency) and on a Bruker Avance DSX spectrometer with a 9.4 T magnet (105.27 MHz ^{51}V Larmor Frequency) using probe heads for 2.5 mm rotor diameters. Glass samples, VG1-VG4 (particle size <45 μm), V_2O_5 (used as provided, analytical grade, Sigma-Aldrich, Canada) and $NaVO_3$ (used as provided, analytical grade, Sigma-Aldrich, Canada) were packed into the rotor and spun between 10.0 and 27.0 kHz. The shown spectra were taken in the 16.4T

instrument at 27 kHz spinning frequency. Up to 400 scans (1600 scans for VG1) were accumulated every 1 second with single pulse excitation using pulse length of 0.61 μs at 100 kHz rf-field strength. The pulse lengths on the 9.4T spectrometer was 2.0 μs with otherwise the same conditions. The chemical shift scale was referenced externally against saturated aqueous $NaVO_3$ solution at -578 ppm.

8.3.4 Quantification of Therapeutic Inorganic Ion Release After Exposure to Simulated Physiological Conditions

The 150-300 μm particles were selected for extract production since this range is commonly used during TACE procedures[244]. Glass extract specimens (1% w/v) were produced by immersing 0.1 g of each glass (n=3) in 10 mL of sterile tissue culture water (Sigma-Aldrich, Canada) in 15 mL falcon tubes for 1, 4, 7, 14 and 30 days [230]. Each specimen was stored at 37 °C in a shaking water-bath (Stuart Sb40, Techne Inc., USA), and agitated at 2Hz (longitudinal movement). After each storage period, individual extracts derived from each glass composition were sterile filtered into sterile 15 mL Falcon tubes through sterile 0.20 μm filter (Sarstedt, Canada) to remove the glass particulates; all samples were stored at 4 °C for subsequent analysis. Si, Na, Zn and V ions released into tissue culture water were quantified using inductively coupled plasma optical emission spectroscopy (ICP-OES) with a Perkin Elmer Optima 8000. The ion concentrations of each extract specimen were determined in triplicate (i.e. n=3 concentration measurements for each extract produced), which were then averaged. To measure the Si and Zn release, extracts derived from VG0-VG4 glasses were diluted 1/10 using 2% HNO_3. To measure Na and V, extracts from VG0-VG2 were diluted (1/10) and

VG3 and VG4 were diluted 1/100. Calibration curves were generated using standards prepared from Perkin Elmer primary standards, supplied in 2% HNO_3 and diluted in 2% HNO_3.

8.3.5 Examining HepG2 Cellular Responses to Glass Dissolution By-Products

Cell viability along with a mechanistic examination of cell death were determined using cell titer blue assay and flow cytometry assays as follows:

8.3.5.1 Cell Culture Conditions

The HepG2 (*American Type Culture Collection)* liver hepatocellular carcinoma cell line was generously gifted to the authors by the Materials Research Institute at the Athlone Institute of Technology. HepG2 cells were cultured (Passage 13) at 37 °C in 5% CO_2 in low glucose DMEM supplemented with 10% FBS and 1% Pen/Strep (Gibco 21885-025, Sigma F7524, Gibco 15140-122) respectively[265]. Cells were subcultured at 80-90% confluency at a density of $1x10^6$/T175. HepG2 cells were seeded at a density of $2.5x10^4$cells/cm^2 in 24-well plates for 24 hrs prior to the start of experiments to allow cells to adhere. Media was then removed and replaced with fresh media containing glass extracts at the following dilutions: 1:1, 1:2, 1:5 and 1:10 (glass extract: media). The glass extracts were produced and evaluated as in section 8.3.4 using six replicates (n=6). Cells were then cultured with glass extract dilutions for 48 hrs. All groups were compared to a viable cell control (undiluted media) and a dead cell control (media + 20 % DMSO). As an additional control, tissue culture water (i.e. the extract vehicle for glass degradation) was added to media using the same dilutions as described for glass extract dilution.

8.3.5.2 Cell Titer Blue (CTB) Assay

To assess cell viability (CV), media was removed from cultures and fresh media containing 10 % CTB *(G8080, Promega)* was added to the cultures for 4 hrs and were incubated at 37°C, 5% CO_2. Media was collected in eppendorf tubes and aliquoted into 96-well plates and the absorbance measured in triplicate at 560/590 nm on a Perkin Elmer Victor 1420 plate reader. CV was calculated as a percentage of the viable cell control using the following formula: % CV = 100 – (100*(((Abs Viable Cells) – (Abs Sample)) / (Abs Viable Cells)). Media containing 10 % CTB alone without cells was used as the negative control.

8.3.5.3 Flow Cytometery

8.3.5.3.1 Apoptosis Assay

To assess mechanism of cell death, Annexin V/7AAD staining *(BDBiosciences 559763)* was carried out using the same experimental design as described above using the 1:10 dilution. After cells were exposed to the extracts for 6, 24 and 48 hrs, media from each well was collected to capture any dead/non-adherent cells. The remaining cells were trypsinized and pooled with the previously removed dead/non-adherent cells. Cells were stained according to manufacturer's protocol and analyzed using the BD Accuri C6 as follows: Cells were washed twice in cold 0.1 M PBS and re-suspended in 1X annexin V binding buffer at a concentration of $1x10^6$ cells/mL. Then, 100 µL of cell suspension was transferred to a 5 mL FACS tube after which 2.5 µL of annexin V-PE and 5 µL 7-AAD-PerCP-Cy5.5 was added to the sample. Samples were gently vortexed for 5 seconds and

incubated for 15 minutes at room temperature in the dark. Finally, 400 µL of 1X annexin binding buffer was added to each sample and samples were analyzed by flow cytometry within 1 hr of staining. As controls, cells cultured in complete medium alone were used as a negative apoptosis control, cells incubated in medium containing 20% DMSO were used as a positive apoptosis control and medium diluted 1:10 unconditioned water:medium was used as a vehicle control. Representative images of the gaiting strategy used for the apoptosis assay are presented in supplemental Figure S1.

8.3.5.3.2 Caspase 3/7 and Caspase 8 Assay

Similar to experiments above, caspase 3/7 *(Invitrogen V35118)* and caspase 8 *(Invitrogen V35119)* detection using flow cytometry was carried out to distinguish between intrinsic and extrinsic pathways of apoptosis. After cells were exposed to the extracts for 6, 24 and 48 hrs, media from each well was collected to capture any dead/non-adherent cells. The remaining cells were trypsinized and pooled with the previously removed dead/non-adherent cells. Cells were stained according to manufacturer's protocol and analyzed using the BD Accuri C6. Briefly, cells were resuspended in culture media at $1x10^6$ cells/mL after which 300 µL of the sample was transferred to a 5 mL FACS tube. Subsequently, 10 µL of 30X FLICA (Fluorescent Labeled Inhibitor of Caspases) working solutions of either Caspase 3/7 or Caspase 8 were added to cell suspension and samples were mixed by flicking the tube. Samples were then incubated in the dark for 60 mins at 37 °C, 5 % CO_2. Samples were mixed every 20 mins during staining. Then 2 mL of 1X wash buffer was added to each tube and cells were pelleted by centrifugation at 300 g for 5 minutes. The supernatant was discarded and cells were re-suspended in 1 mL of 1X

wash buffer. Cells were pelleted by centrifugation again and samples were resuspended in 400 µL of 1X wash buffer and assessed by flow cytometry at 488/530nm. Controls were also assessed as described in 8.3.5.3.1. Representative images of the gaiting strategy used for the caspase assays are presented in supplemental Figure S2.

8.3.6 Computed Tomography Radiopacity

Quantitative CT radiopacity measurements of each glass (150-300 µm, n=5) were determined by taking axial CT scans (1 mm slice thickness, pitch=0.5, 140 kVp) through glass vials using a Somatom Definition Flash Scanner (Siemens Healthcare, Erlangen, Germany). All measurements were performed on the 150-300 µm particle size range and radiopacity was reported in Hounsfield Units (HU) ± SD.

8.3.7 Statistics

One-way and two-way analysis of variance (ANOVA) using a Tukey post-hoc evaluation was utilized where appropriate and error bars on all graphs represent standard deviation about the mean. Data was considered significant when $p \leq 0.05$. All calculations were done using Prism 6 for Mac OS X (GraphPad Software Inc., La Jolla, USA)

8.4 Results

8.4.1 Physical and Chemical Characteristics of Zinc-Silicate Glasses with V_2O_5 Additions

For completeness, particle size distributions for all glass compositions are shown in Table 8.2. All glasses were confirmed as amorphous, with no identifiable crystalline species, via XRD measurements of glass powders VG0-VG4 (data not shown).

Table 8.2: Particle size analysis of vanadium-based glasses

	Less than 45 µm			**150-300 µm**		
	D90	D50	D10	D90	D50	D10
VG0	55.9	28.9	11.7	438	291	189
VG1	57.8	31.3	13.9	451	296	189
VG2	67.1	33.3	12.3	459	298	190
VG3	67.7	33.8	13.2	465	305	195
VG4	65.7	34.6	15.6	458	294	185

The density of the zinc-silicates under investigation ranged between 2.905±0.002 and 2.682±0.004 g/mL; a linear decrease in density, and corresponding increase in molar volume was observed with increasing V_2O_5 in the glass formulation (Figure 8.1a). T_g ranged between 489.4±2.7 and 383.1±2.4 °C; a linear decrease was observed with addition of V_2O_5 (Figure 8.1b). Error bars are plotted for all data points, but in many cases error bars are contained within discrete data points.

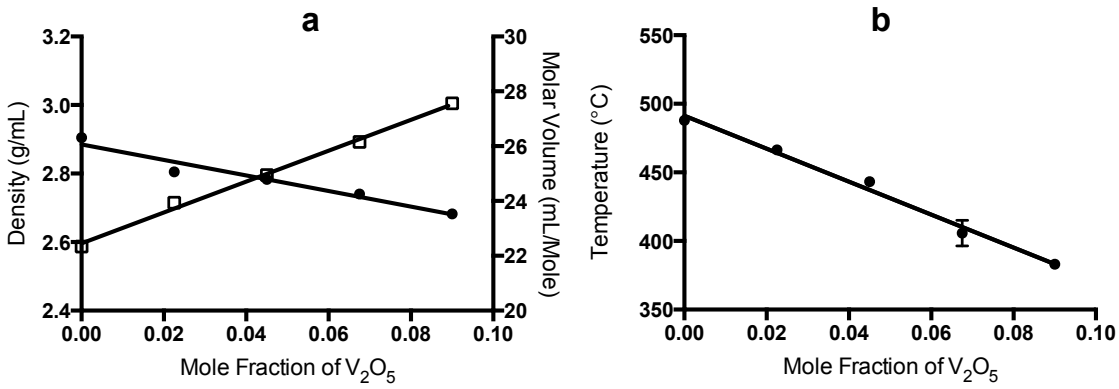

Figure 8.1: (a) Density (circles) and Molar Volume (squares) (R^2=0.951 and 0.995, respectively) and (b) T_g (R^2=0.980) of glasses plotted as a function of mole fraction V_2O_5.

8.4.2 Characteristics of the ^{29}Si and ^{51}V Network Environments

Figures 8.2 shows the ^{29}Si MAS NMR spectra for all the glasses. All spectra show small spinning sidebands well separated from the main peaks at their isotropic shifts. The maxima of the ^{29}Si peaks shift upfield (-79 ppm for VG0 to -91 ppm for VG4) with the addition of V_2O_5 to the glass formulation.

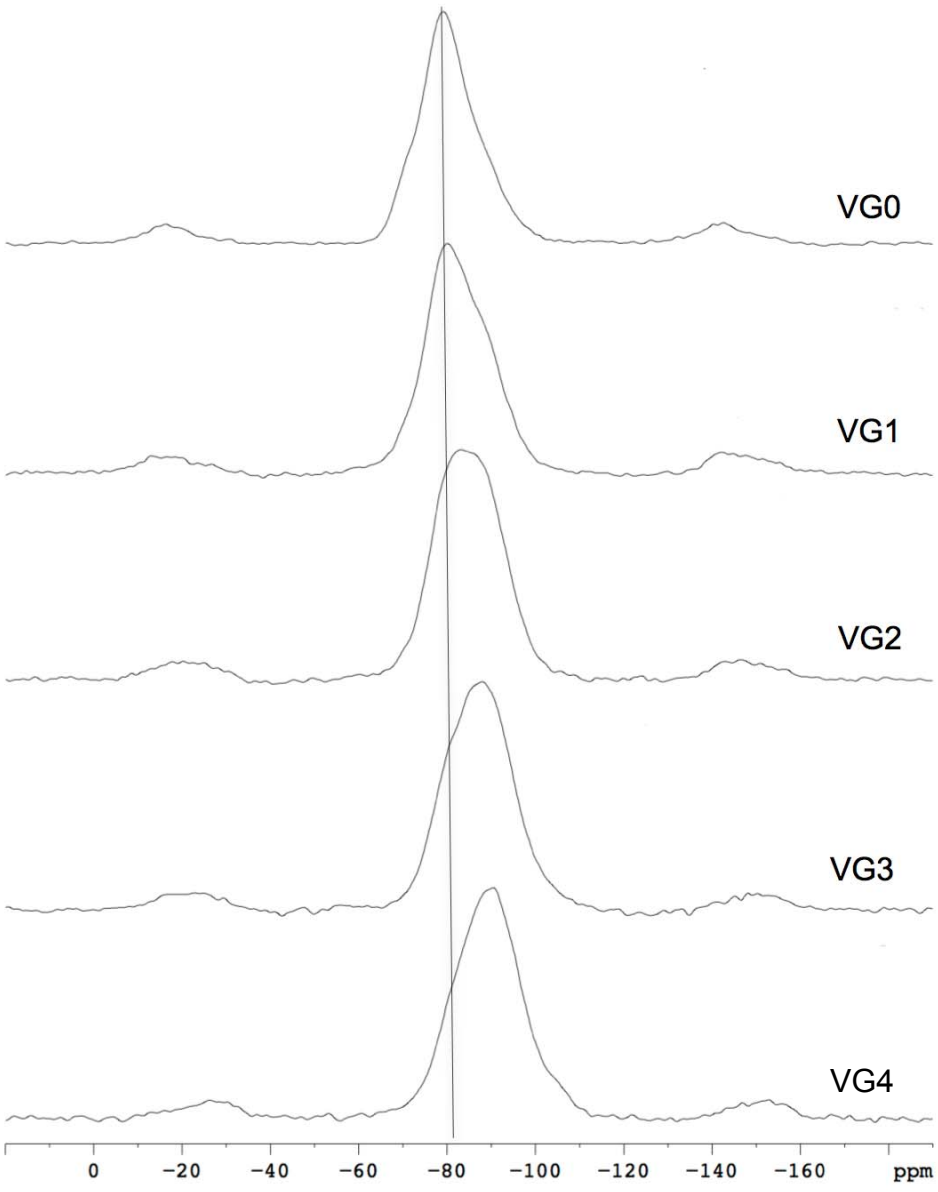

Figure 8.2: ^{29}Si MAS NMR spectra of all experimental glasses. Line indicates the peak position for the V_2O_5 free glass (VG0) and passes through the peaks at their isotropic shifts of all glasses. All other maxima are identified as spinning sidebands.

Figures 8.3 shows the ^{51}V MAS NMR spectra, for all V_2O_5 containing glasses. The shifts of the ^{51}V peaks and their line width remain constant with the addition of V_2O_5 to the glass system.

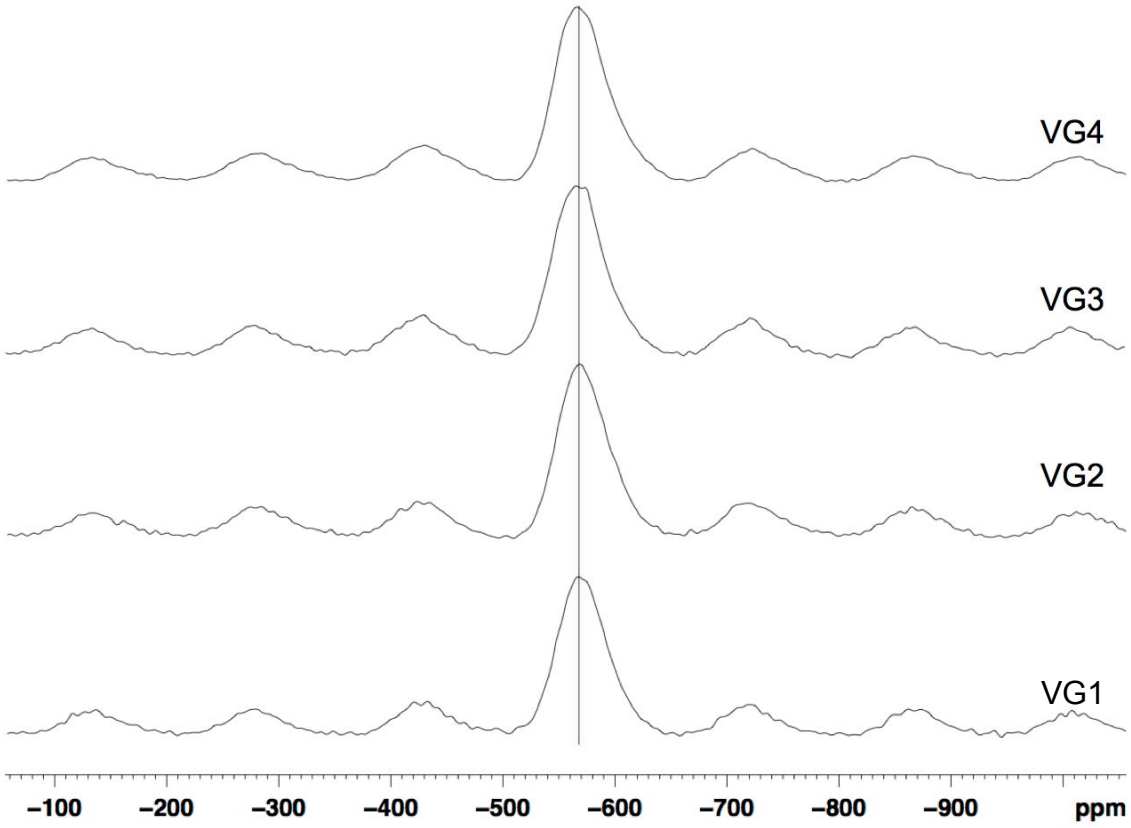

Figure 8.3: ^{51}V MAS NMR spectra of all experimental glasses containing vanadium. Line indicates the peak position for VG1 and passes through the peaks at their isotropic shifts. All other maxima are identified as spinning sidebands.

Figure 8.4 compares the ^{51}V NMR spectra for vanadium pentoxide (V_2O_5), sodium metavanadate ($NaVO_3$) and a representative glass (VG4). The spectrum of V_2O_5 shows only one resonance at -618.0 ppm with associated spinning side bands. The ^{51}V NMR

spectrum of $NaVO_3$ features two major and one minor resonance at -517.2, -579.3 and -552.7 ppm, respectively, with associated spinning side bands. The peak width of VG4 permits the inclusion of structures similar to both $NaVO_3$ and V_2O_5. The peak maxima of VG4 at -566 ppm correlates with the peak position of $NaVO_3$ suggesting VG4 shares structural similarities with $NaVO_3$.

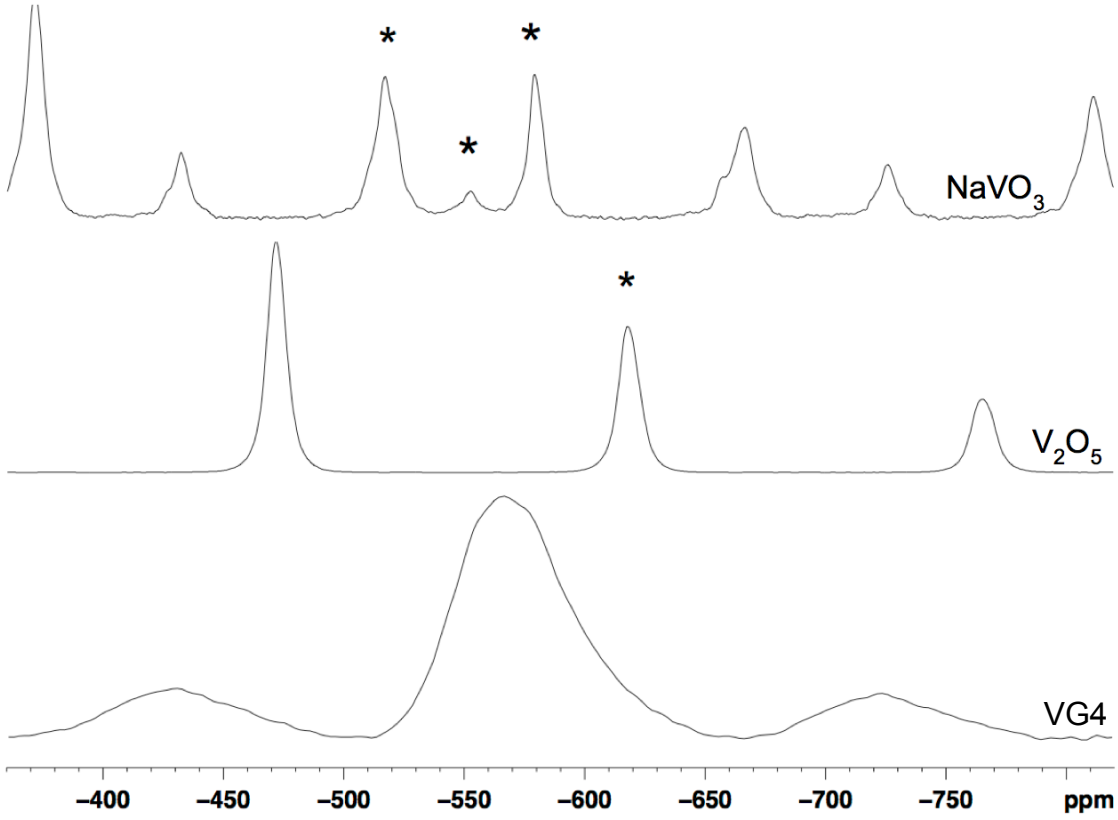

Figure 8.4: ^{51}V MAS NMR spectra of sodium metavanadate ($NaVO_3$), vanadium pentoxide (V_2O_5) and VG4 glass. Stars indicate the peaks at the isotropic chemical shifts for the crystalline samples V_2O_5 and $NaVO_3$ samples.

8.4.3 The Temporal Dissolution Characteristics of Zinc-Silicate Glasses as a Function of V_2O_5 Addition

The temporal release of dissolution by-products (Si, Na, Zn and V) from the zinc-silicates system was quantified at 1, 4, 7, 14, 30 days (Figure 8.5). VG3 and VG4 (i.e. those formulations with the highest V_2O_5 content) provide for the highest concentrations of all ions at each time point ($p < 0.0001$). With respect to VG3 and VG4, it is striking that Na and V share similar release profiles; importantly, the concentration of each ion increases as a function of time ($p < 0.0001$). VG0 (vanadium free), VG1 and VG2 provide for no detectable release of Zn or V, and provide limited Na and Si release (two orders of magnitude lower than VG4).

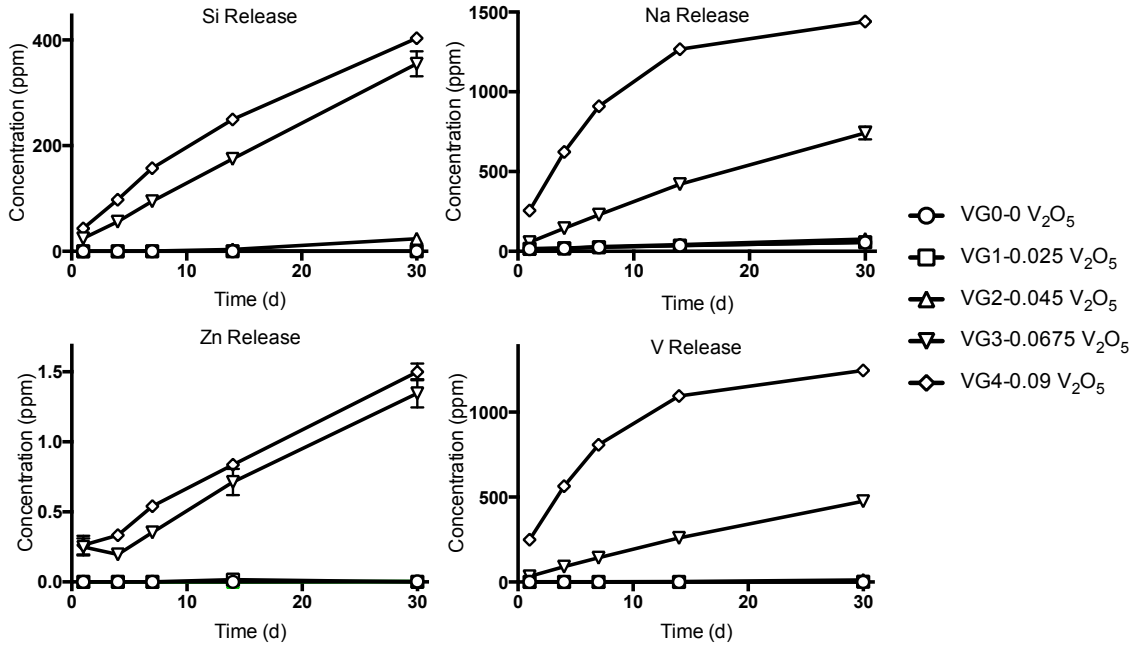

Figure 8.5: Ion release profiles for Si, Na, Zn and V from extracts derived from glass compositions VG0-VG4 after 1, 4, 7, 14 and 30 days in extract media.

Due to the apparent paired release of Na and V in VG3 and VG4 (Figure 8.5) and in order to estimate the efficiency of this zinc-silicate system to release a therapeutic payload, the ratio of the actual V/Na ions released was plotted as a function of the theoretical maximum V/Na ratio determined from the composition of the glass. Figure 8.6 identifies that an exponential relationship exists with regard to loading and release efficiency providing a potential mechanism to control dose based on initial composition.

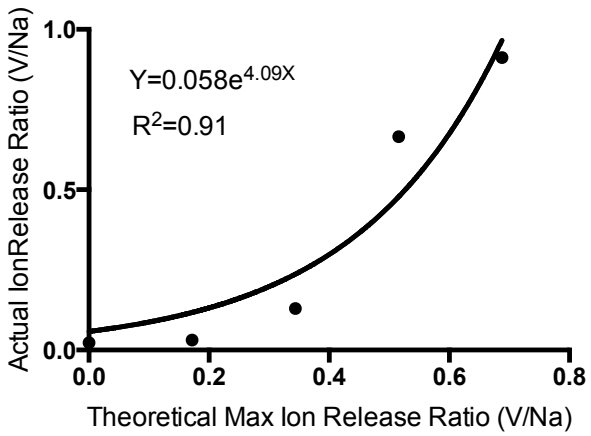

Figure 8.6: The effect of the theoretical maximum V/Na ion release ratio on the actual release ratio for each glass composition at 30 days.

8.4.4 *In Vitro* Biological Evaluation of Dissolution By-Products From Zinc-Silicate Glasses

8.4.4.1 Concentration Dependent Cell Viability

Figure 8.7 shows (i) the effect of the V/Na ratio in solution (as derived from respective extracts) on CV and (ii) the effect of extract dilution on CV. A significant modulation of

CV is observed as both a function V/Na ratio and dilution: broadly, CV ranged from 9% to 98% (Figure 8.7). All dilutions tested demonstrated decreased CV with increasing V/Na ratio. At the 1:1 dilution, (i.e. those extracts with the highest concentration of ions) this decrease was best estimated by an exponential function (Table 8.3). For all other dilutions the decrease in CV was modeled using linear functions. The equations of best fit are shown in Table 8.3 with associated R^2 values. For completeness, media diluted with tissue culture water was used as an additional control; the CV for this control was observed to be in range of 90 to 103% (data not shown). Furthermore the CV observed for the tissue culture water dilutions were not statistically different from the media control.

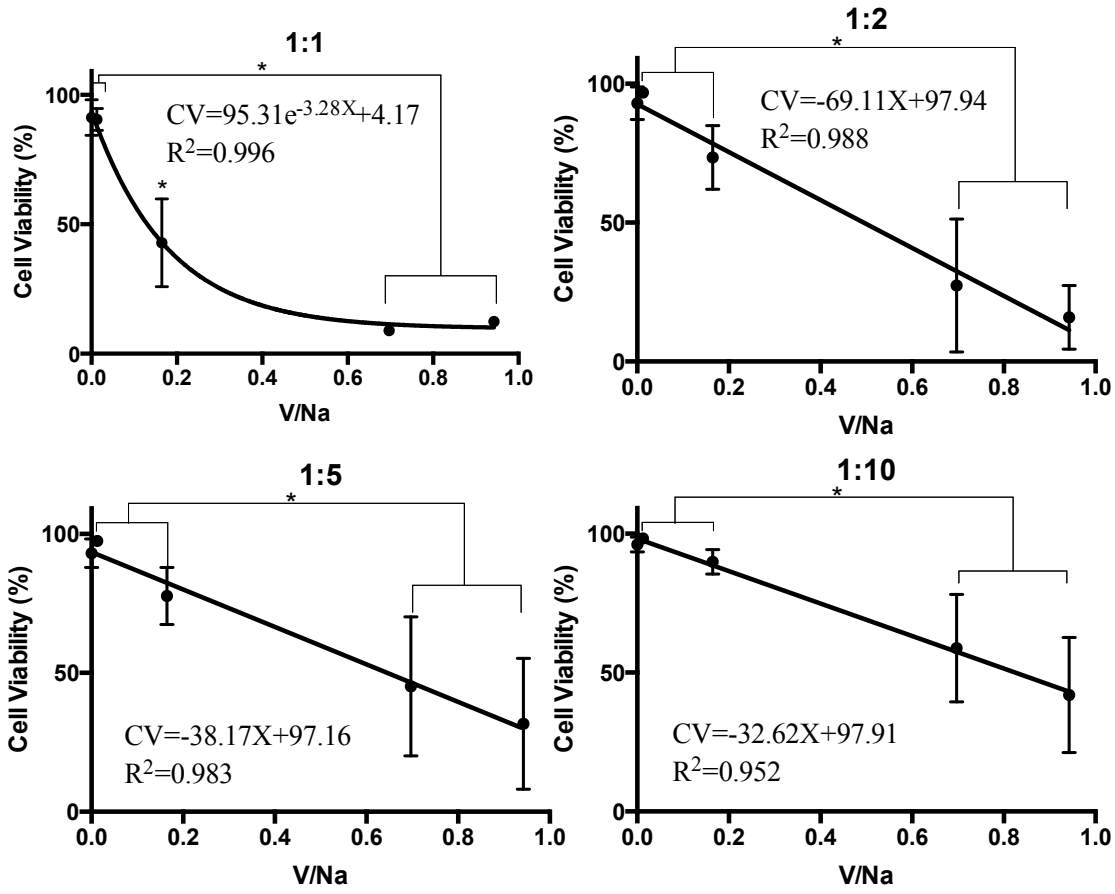

Figure 8.7: Compositional dependence of cell viability of HegG2 cells incubated with glass extracts derived from the 30 day time point at different dilutions (1:1, 1:2, 1:5 and 1:10) for 48 hours, assessed by a cell titer blue assay

8.4.4.2 Determination of the Mechanism of Induced Cell Death After Exposure to Zinc-Silicate Extracts as a Function of the V/Na ratio

To determine the mechanism by which the dissolution by-products induced cell death, HepG2 cells were exposed to the extracts, at a 1:10 dilution, for 6, 24 and 48 hours (Figure 8.8). For clarity, this dilution was selected in order to avoid a rapid cytotoxic response associated with high ion concentrations in extracts, which may mask or limit the ability to determine the mechanistic pathway of cell death. Cells were fluorescently

labeled and evaluated using flow cytometry to determine the population that was alive, undergoing early apoptosis and undergoing late apoptosis/necrosis (Figure 8.8). Representative 7AAD/Annexin V staining of HepG2 cells incubated with glass extracts at 24 hours are shown in Supplemental Figure S3.

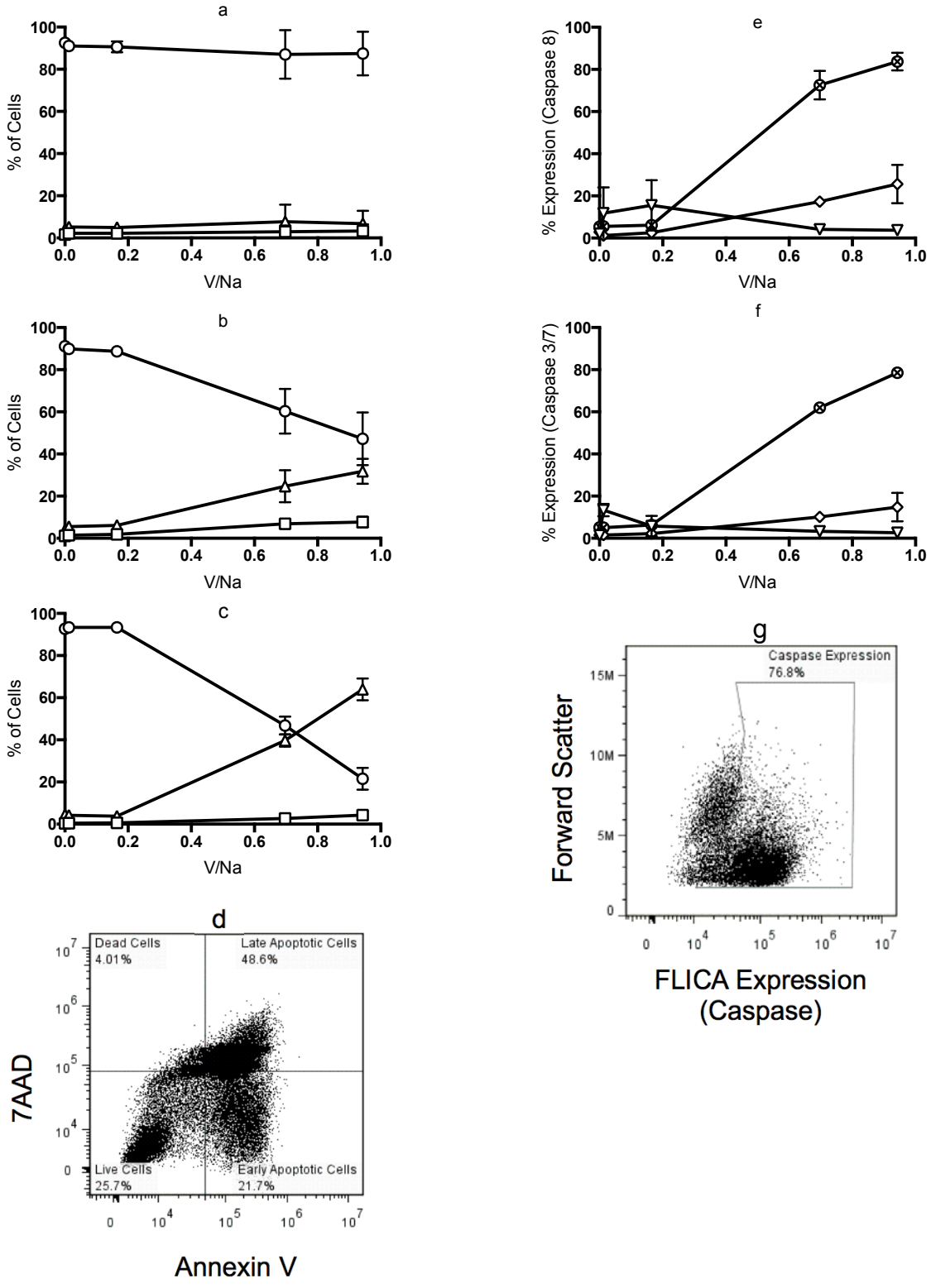

Figure 8.8: (a-d) Assessment of cell death mechanism of HepG2 cells after exposure to 30 day extracts at a 1:10 dilution for (a) 6 h, (b) 24 h and (c) 48 h showing cells in live

(○), early apoptotic (□) and late apoptotic (△) states, plotted against V/Zn ratio. Panel (d) is an example of the raw data after 24 h of exposure to the VG4 glass extracts. (e-g) Assessment of apoptotic pathways in HepG2 cells after exposure to 30 day extracts at a 1:10 dilution. Evaluation of the percent expression of (e) caspase 8 and (f) caspase 3/7 in HepG2 cells after exposure to extracts for 6 h (▽), 24 h (◇) and 48 h (⊗) and was plotted as a function of V/Na ratio. Panel (g) is an example of the raw data at 24 h of exposure to the VG4 glass extracts.

Figure 8.8 (a-c) clearly illustrates that increases in V/Na induces an apoptotic response that is both time dependent and concentration dependent. At 48 hours VG4 shows the greatest increase in cells undergoing apoptosis ($p < 0.0001$). Taken with Figures 8.5 and 7.6 these data show the potential for VG3 and VG4 to provide vectored delivery of therapeutic inorganic ions to mediate apoptosis in HepG2 cells.

8.4.4.2.1 Apoptosis Induced Cell Death Mechanism, Caspase 8 and Caspase 3/7 After Exposure to Zinc-Silicate Extracts as a Function of the V/Na Ratio

The percent expression of caspase 8 (Figure 8.8e) and 3/7 (Figure 8.8f) (determined at 6, 24 and 48 hrs) was plotted as a function of V/Na ratio. There was a time dependent increase in the expression of caspase 8 and 3/7 for glass extracts derived from VG3 and VG4. With respect to the expression of caspase 8 at 48 hours, there was no statistically significant difference between VG3 and VG4. In addition, the following statistical differences ($p<0.0001$) were noted: VG4>VG2 and VG3>VG2. At 48 hours the percent expression of caspase 3/7 increased with increasing V/Na whereby VG4>VG3>VG2

($p<0.0001$). Representative FLICA expression (caspase) of HepG2 cells incubated with glass extracts at 24 hours are shown in Supplemental Figure S4.

8.4.4.3 Compositional Dependence of CT Radiopacity on V_2O_5 Formulated Zinc-Silicates

To assess the clinical utility of the glasses synthesized the CT radiopacity of each composition was measured. Addition of V to the glass caused a reduction in CT radiopacity, Figure 8.9. CT radiopacity ranged between 1770±33 for VG0 and 1070±27 HU for VG3. There appears to be a small increase in radiopacity between VG3 and VG4. Error bars are plotted for all data points, but in many cases error bars are contained within the size of the point.

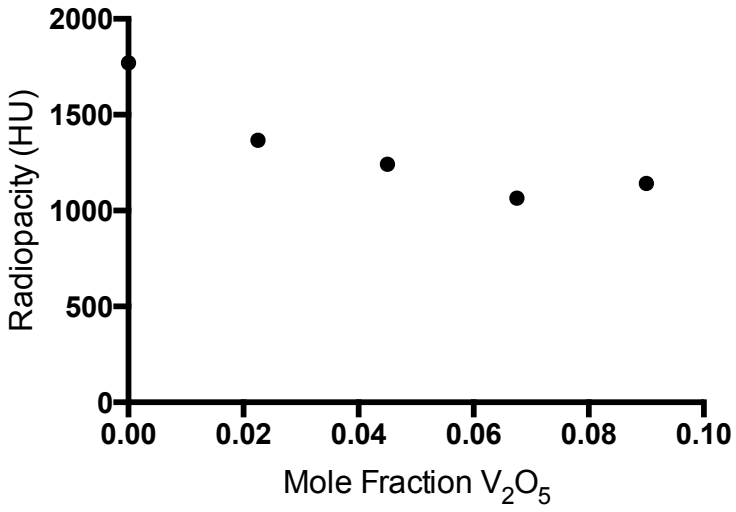

Figure 8.9: CT radiopacity as a function of the mole fraction of V_2O_5 in each glass

8.5 Discussion

The compositional palette of bioactive glasses has been largely constrained to the original bioglass formulations, and their applications have been biased toward hard tissue augmentation. However, the paradigm is changing. The potential applications for new glass systems are driving the formulation of new materials and contiguous experimental designs at the forefront of natural sciences and engineering[138, 266]. One area of particular interest is the potential use of therapeutic glasses in oncology. To date, efforts in this regard have been primarily associated with selective internal radiation delivered from durable Y_2O_3-Al_2O_3-SiO_2 microspheres[266, 267]. However, designing *biocompatible and degradable* glass networks, capable of selectively delivering payloads of TIIs, may enable significant advances in materials technology and treatment modalities in oncology.

It is clear from the literature that the term '*biocompatibility*' is ubiquitously associated with repair and regeneration. Considering Black's definition of the term[145], and the emerging philosophy that "we should aim to develop synthetic materials that establish key interactions with cells in ways that unlock the body's innate powers of organization and self-repair" [146], it becomes clear that an alternative paradigm exists. From the perspective of biomaterials in oncology, targeted destruction of tumor tissue is, by definition, the appropriate *host response* for a biocompatible material[263, 267]. Therefore, the challenge is to engineer a *'material response'* that provides a simple but powerful mechanism to encode cancer cells to self-destruct. It is in this regard that the controlled release of TIIs may yield significant clinical benefits. Within this philosophical

framework, the selective leaching of vanadium containing ions from glass networks may provide a simple approach to activate apoptotic processes in cancer cells, as vanadium compounds have been shown to arrest the cell cycle and/or exert cytotoxic effects through DNA damage and plasma membrane lipoperoxidation[212, 215]. From a materials response standpoint, this approach (i.e. the deployment of vanadium leaching glasses) is supported by the hydrolytically unstable nature of V-O-Si bonds[268], which may provide for targeted and preferential loco-regional release of vanadium ions under physiological conditions within a tumor.

Designing a glass capable of delivering a therapeutic payload of vanadium ions depends on understanding the composition-structure-property-function relationships within its contiguous glass system. Clues about glass structure can be inferred from changes in physical properties like density, molar volume and T_g. It was observed that the addition of V_2O_5, a network former, to the glass (substituting for ZnO) resulted in linear decreases in both density and T_g with a concomitant linear increase in molar volume (Figure 8.1). These data suggest that V_2O_5 substitutions cause an opening of the glass network, which may enhance the ion release characteristics of a glass, on the assumption that the network structure remains unchanged as a function of the substitution[245]. The ^{29}Si MAS NMR spectra (Figure 8.2) indicate that Si is in a fourfold oxygen coordinated state[18, 160, 248] and, contrary to physical data, addition of V_2O_5 causes polymerization of the Si-O-Si network. The chemical shift of ^{29}Si moves from -87 in to -98 ppm as V_2O_5 increases, which is an observation consistent with the work of Luca et al.[269]. Such polymerization suggests sequestration and/or removal of network modifying agents and

non-bridging oxygens away from the local silica environment within the glass network. At first glance, this is a surprising result given that (i) the Na_2O content remains constant across the glass series and, (ii) the oxygen load increases as the V_2O_5:ZnO increases. Contrastingly, V_2O_5 loading causes no observable change in peak position for the ^{51}V MAS NMR spectra (Figure 8.3), suggesting that the vanadium structures present in the network are independent of concentration up to 0.09 mole fraction of V_2O_5.

To elucidate the structural environment of vanadium in the network, the spectra of $NaVO_3$ and V_2O_5 were collected and compared to VG4 (Figure 8.4). The crystal structure of solid α-$NaVO_3$ reveals that α-$NaVO_3$, consists of chains of VO_4 tetrahedra, each corner sharing with two other tetrahedrons[270]. The corner sharing V-O bonds have a distance of 1.8 Å, which are slightly longer than the terminating V-O bonds with 1.6 Å[270, 271]. O.B. Lapina et al. describe this structure as "VO_4 type Q^2 " following the nomenclature familiar from ^{29}Si NMR classifications, i.e., the upper index indicates the number of bridging bonds of a tetrahedron[272]. In contrast, Lapina et al. classify β-$NaVO_3$ as "$VO_{5/6}$ with axial symmetry" because it consists of 5-coordinated vanadium units. The crystal structure of β-$NaVO_3$ reveals that vanadium is coordinated to two non-bridging oxygens (bond length 1.70 Å and 1.63 Å) and to three bridging oxygens, two with a vanadium-oxygen bond lengths of 1.91 Å and one with 1.97 Å length[264]. Each of these bridging oxygen atoms are coordinated to three different vanadium sites. This structure creates chains of VO_5 units each edge sharing with two other VO_5 units along the chain[273]. Hayakawa et al. identified the isotropic chemical shifts of α-$NaVO_3$ with linear corner-shared VO_4 units, and β-$NaVO_3$ with edge-shared VO_5 pyramids units at -

576 ppm and -515 ppm respectively[274], consistent with the spectra observed in this study (-579 and -517 ppm). For completeness, V_2O_5 consists of linear double chains of VO_4 tetrahedra, with one short bond 1.585 Å and three corner shared bonds to neighboring tetrahedra with longer bonds, specifically 1.780 Å to the parallel strand tetrahedron and 1.878 Å to both tetrahedra along the chain[275]. As such, the structures of the V_2O_5 could be classified as " VO_4 type Q^3", even though Lapina et al. classify the structure as $VO_{5/6}$ by counting the O-V distance of 2.79 Å to neighboring double chains as a bond[272]. Eckert and Wachs reported that V_2O_5 had chemical shift of -609 ppm[276], which is in agreement to the isotropic shift frequency of the V_2O_5 measured in this study at -618 ppm, considering the magnetic field strength dependent isotropic quadrupole shift. Importantly, there is excellent separation between the NMR peaks associated with $NaVO_3$ and V_2O_5 structures, thereby providing a means to identify the possible structures in the glasses. The peak position for the vanadium containing glasses all fall between -569 and 563 ppm, which is similar to the peak position of corner shared tetrahedral VO_4 units of α-$NaVO_3$. Taking the ^{29}Si and ^{51}V MAS NMR data together indicate that polymerization of the Si network could be due to the formation of VO_4 tetrahedrons similar to those found in $NaVO_3$. Schematically, this is achieved by breaking V-O-V bonds from the V_2O_5 structure (Q^3 type) to form two vanadium tetrahedra with two terminating oxygens (Q^2 type) by insertion of oxygen, which is taken from two Si tetrahedra with terminating oxygens thereby creating a Si-O-Si bridge. Formally, this structural transformation upon increase of the V_2O_5 concentration in the glasses (replacing ZnO) can be written as

$$2\ Q^2(Si) + 2\ Q^3(V) \rightarrow 2\ Q^3(Si) + 2\ Q^2(V)$$

The additional non-bridging oxygens on the vanadium tetrahedra are charge compensated by sodium cations, thus forming an amorphous $NaVO_3$ like structure though sequestration of Na from the Si environment. Mekki et al. confirmed the presence of V-O-Na structures from XPS from the O 1s spectra[277], which supports the idea that Na is being sequestered from the Si network allowing it to undergo polymerization.

Glass structure has a major impact on ion dissolution kinetics. Highly polymerized glasses contain a large portion of interconnected network forming agents and tend to be less susceptible to degradation than glasses composed of mainly network modifying agents[258, 259]. Based on the composition-structure-property relationships outlined in this work it is possible to modulate the release of the therapeutic payload of vanadium ions from the glass network. From Figure 8.5, it is clear that large amounts of ions were released from the zinc-silicates once the mole fraction of V_2O_5 was greater than or equal 0.045 (VG3 and VG4). Therefore, increasing the V_2O_5 content in the glass results in glasses that are more susceptible to dissolution, likely arising from (i) the solubility of $NaVO_3$[278] and/or (ii) the hydrolytic instability of Si-O-V bonds[268]. The efficiency of this ion release was evaluated from a plot of the ratio of V/Na ions released from the glass verses the ratio of V/Na ions in the glass. An exponential dependence was observed (Figure 8.6) indicating a mechanism for the controlled release of the therapeutic payload from the glass. Succinctly, the Si network becomes more polymerized upon addition of V_2O_5 yet simultaneously becomes more susceptible to selective leaching of vanadium in simulated physiological conditions. Interestingly, the similarity in the ion release profiles of Na and V suggests that these elements are associated in the glass corroborating the

conclusions from the ^{51}V and ^{29}Si MAS NMR data (Figures 8.3 and 8.4). In order to assess the therapeutic efficacy (i.e. appropriate host response) of the vanadium payload, glass extracts were utilized against HepG2 cells. Cells had a concentration dependent cytotoxic response at (i) each dilution level and (ii) with increasing the V/Na ratio (Figure 8.7): demonstrating the possibility to modulate both the material and host responses for optimized and personalized dosing. Vanadium is likely mediating the observed cytotoxic response given that all other ions are present in levels known to be non-toxic[23]. Only at the 1:1 dilution level did VG2 glass extracts demonstrated a cytotoxic response, which may indicate the existence of a threshold between the concentrations of vanadium and sodium extracted (30 days) from VG1 (V:1.4 and Na:56 ppm) and VG2 (V:12 and Na:77 ppm). When adjusted for the 1:1 dilution HepG2 cells are (i) sensitive to vanadium concentrations above of 0.7 ppm, as there was as significant difference in CV between VG1 and VG2 and (ii) are insensitive to increases in vanadium concentrations above 238 ppm, as there was no significant difference in CV between VG3 and VG4. For completeness, the authors note that a limitation of this work is that the exact speciation remains to be ascertained.

Apoptosis involves a biologically orchestrated sequence of events that results in the elimination of cells without releasing harmful substances within the adjacent tissue(s). In contrast, necrosis is characterized by a loss in membrane integrity and uncontrolled release of cell death products into the extracellular space, which induces a local inflammatory response and in extreme cases can clinically result in the need for necrotic tissue debridement. Therefore, in a therapeutic context apoptosis is desirable. In fact

apoptosis-inducing therapy is increasingly attractive for anti-cancer strategies and is generally considered safe and efficacious[279]. The data suggests that the cytotoxic response of HepG2 cells in response to vanadium-containing glass extracts is mediated via the apoptotic pathway, demonstrable by the time- and dose-dependent progression of HepG2 through early- and late-stage apoptosis (Figure 8.8: a-c). This is supported by the work of Luo et al, which has implicated Fas-Associated protein with Death Domain (FADD), a pivotal component of death receptor-mediated extrinsic apoptosis in vanadium-induced cell death[280]. The enrichment of caspase-8 would further support the involvement of the death-receptor mediated extrinsic apoptotic pathway, which was significantly increased in VG3 and VG4 samples (Figure 8.8: e,f). However, it is noted that the intrinsic and extrinsic apoptotic pathways can be linked by caspase-8-mediated Bid cleavage and subsequent translocation of truncated Bid to the mitochondria to initiate intrinsic apoptosis[281] and positive feedback via caspase-8 in the extrinsic pathway, and thus warrants further investigation. Furthermore, Wu and colleagues have recently shown that sodium orthovanadate effectively induced apoptosis in hepatocellular carcinoma cells potentially via the mitochondrial pathway[282]. Differences relating to the precise mechanism of vanadium-induced cell death are not uncommon in the literature with increasing focus being lent to the role of autophagy and necroptosis[282-284]; however the potential of vanadium as an apoptosis-inducing therapy is widely recognized and is further supported here[212, 285, 286].

As yet, an ideal radiopacity for TAE particles has not been identified in the literature, so it is difficult to specify an appropriate value. All glasses have radiopacity values below

50:50 strength contrast agent Isovue® 370 which prohibits intra-procedural visualization of particle spatial and temporal distribution. The clinical utility of vanadium-loaded glasses was evaluated using CT radiopacity (Figure 8.9). Generally, increased mole fraction of V_2O_5 caused radiopacity to decrease, likely due to V having a lower atomic number than Zn [287]. CT radiopacity ranged between 1770±33 and 1070±27 HU, which is lower than 50:50 strength contrast agent Isovue® 370 of 2520 HU, a useful benchmark for radiopacity [19] and may preclude *temporal* observation during embolic delivery. Nevertheless, Kilcup et al. suggest that radiopacity values comparable to those obtained herein may provide a method to evaluate the *spatial* distribution of particles using either cone beam CT immediately post embolization, or with conventional CT scan during follow-up[26]. Using mice, Meng et al. show that subcutaneously implanted microspheres with radiopacity values approximately equal to 4250 HU were visible using X-ray[288]. Lee et al. demonstrated that tantalum containing nanoparticles with radiopacity values below 1000 HU when suspended in water caused enhanced visibility of blood vessels, spleen and liver in a rat using CT imaging[289]. Clearly there is a wide range of radiopacity values that can be used for monitoring the *spatial* distribution of embolic particles, and the glasses designed in this study fall within this range.

8.6 Study Limitations

As with any scientific study, limitations exist and the authors would like to acknowledge the following limitations:

- The effect of V_2O_5 on the glass structure was not evaluated in a ZnO free system. The substitution of V_2O_5 for ZnO was not stoichiometric. The mole fraction of ZnO was replaced with an equal mole fraction of V_2O_5.
- The study assumes the following charges for ionic species detected using ICP-OES: Na^{+}, Zn^{2+}, V^{5+} and Si^{4+}.
- The glass extracts contain all of the released ions not just specifically vanadium and therefore it is not possible to evaluate the effect of vanadium ions, individually.

8.7 Conclusion

This study reflects a changing paradigm in biomedical glass design philosophy. Traditionally these glasses are designed to trigger repair and regeneration processes in host tissue. However, in an oncology application the opposite is desired. To test this philosophy vanadium containing zinc-silicate glasses were synthesized where V_2O_5 replaced ZnO in the composition. Increasing the V_2O_5 content caused the silica network to polymerize, which unexpectedly caused a simultaneous increase in TII release. Solid state ^{51}V NMR demonstrated that vanadium was present in the network as sodium metavanadate like structures, indicating that sodium was sequestered from the silica network and likely caused the polymerization. Since sodium metavanadate is highly soluble, it is probable that these structures are susceptible to hydrolytic degradation and therefore are the source of the increased TII release. HepG2 cells exposed to these extracts demonstrated concentration dependent cytotoxic responses, where increased TII concentration resulted in significantly greater cell death. Using flow cytometry, it was

determined that the mechanism of cell death was via an extrinsic apoptosis pathway activated by caspase 8. Biomedical glasses offer a unique ability to mediate host-material responses the delivery of TIIs, which can be controlled through simple compositional changes.

Author Contributions:

All authors contributed substantially to this work.

Acknowledgements:

The authors acknowledge the facilities and technical assistance of the Flow Cytometry Core Facility at NUI Galway, a facility that is funded by NUI Galway and the Irish Government's Programme for Research in Third Level Institutions, Cycle 5, National Development Plan 2007-2013.

We are also grateful for the financial assistance of the Natural Sciences and Engineering Research Council of Canada (NSERC) Discovery Grant # 386022 and the Canadian Foundation for Innovation and Nova Scotia Research and Innovation Trust Project # 27170.

8.8 Supplementary Figures

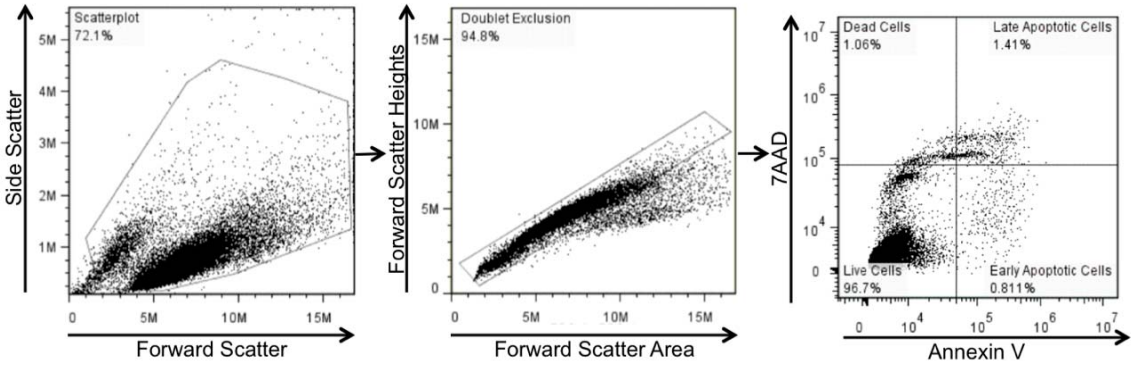

Supplemental Figure S1: Representative image of gating strategy for flow cytometric analysis of apoptosis of HepG2 cells exposed to glass extracts

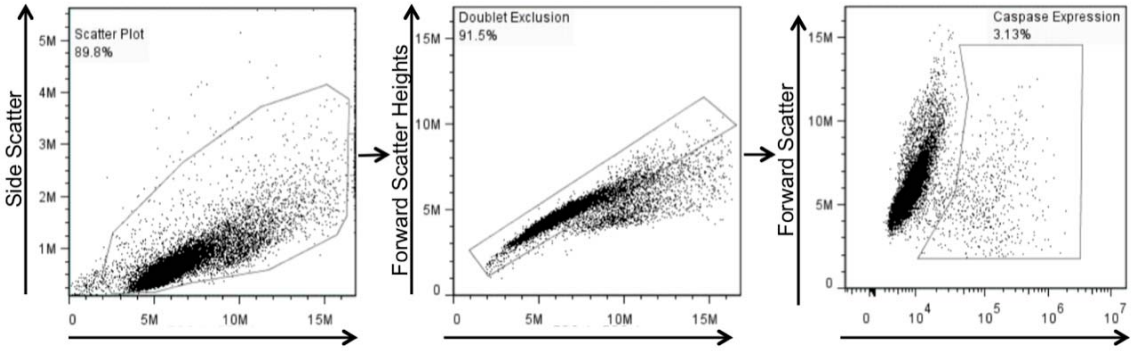

Supplemental Figure S2: Representative image of gating strategy for flow cytometric analysis of caspase expression of HepG2 cells exposed to glass extracts

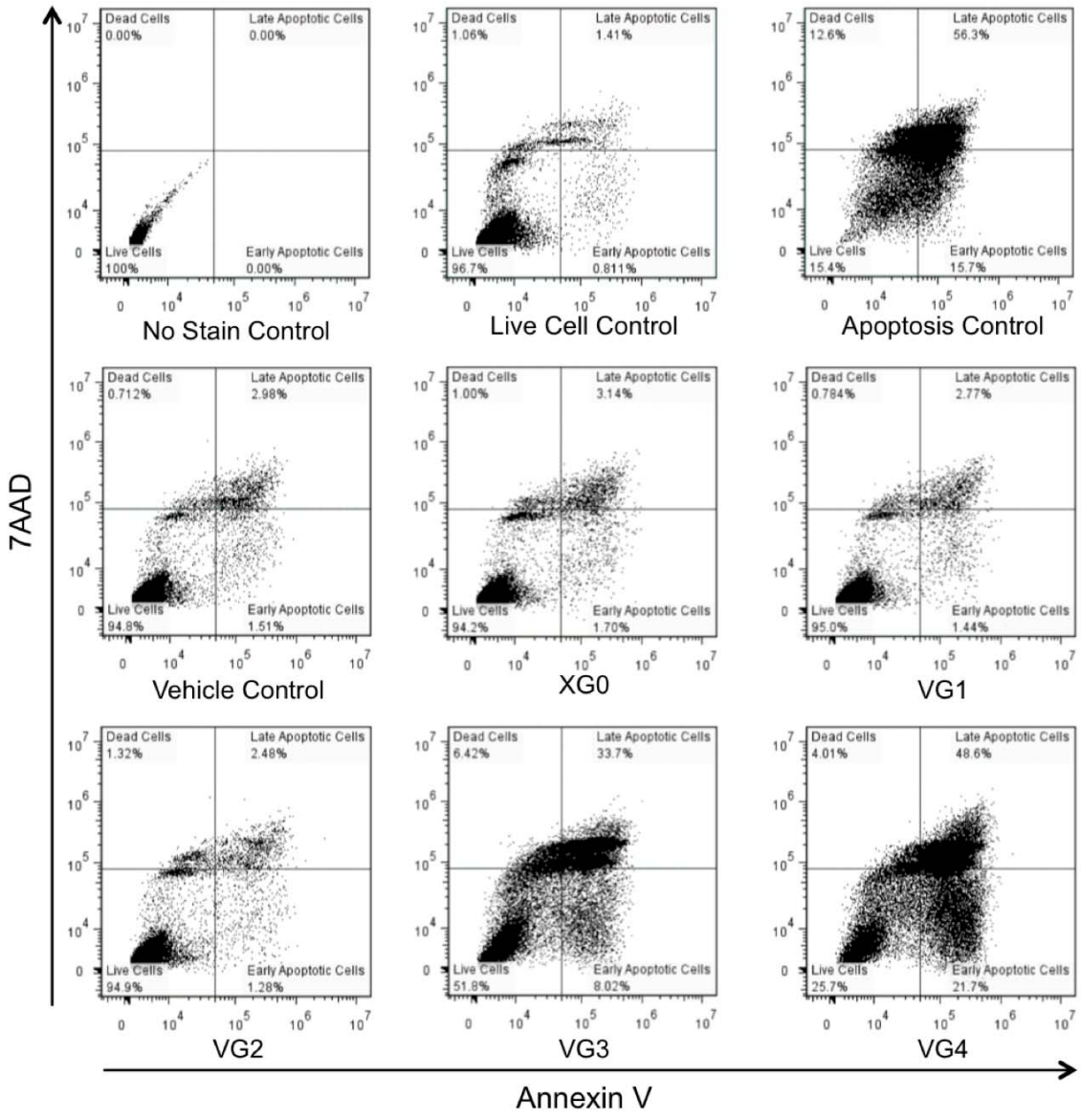

Supplemental Figure S3: Representative 7AAD/Annexin V staining of HepG2 cells incubated with glass extracts for 24 hours

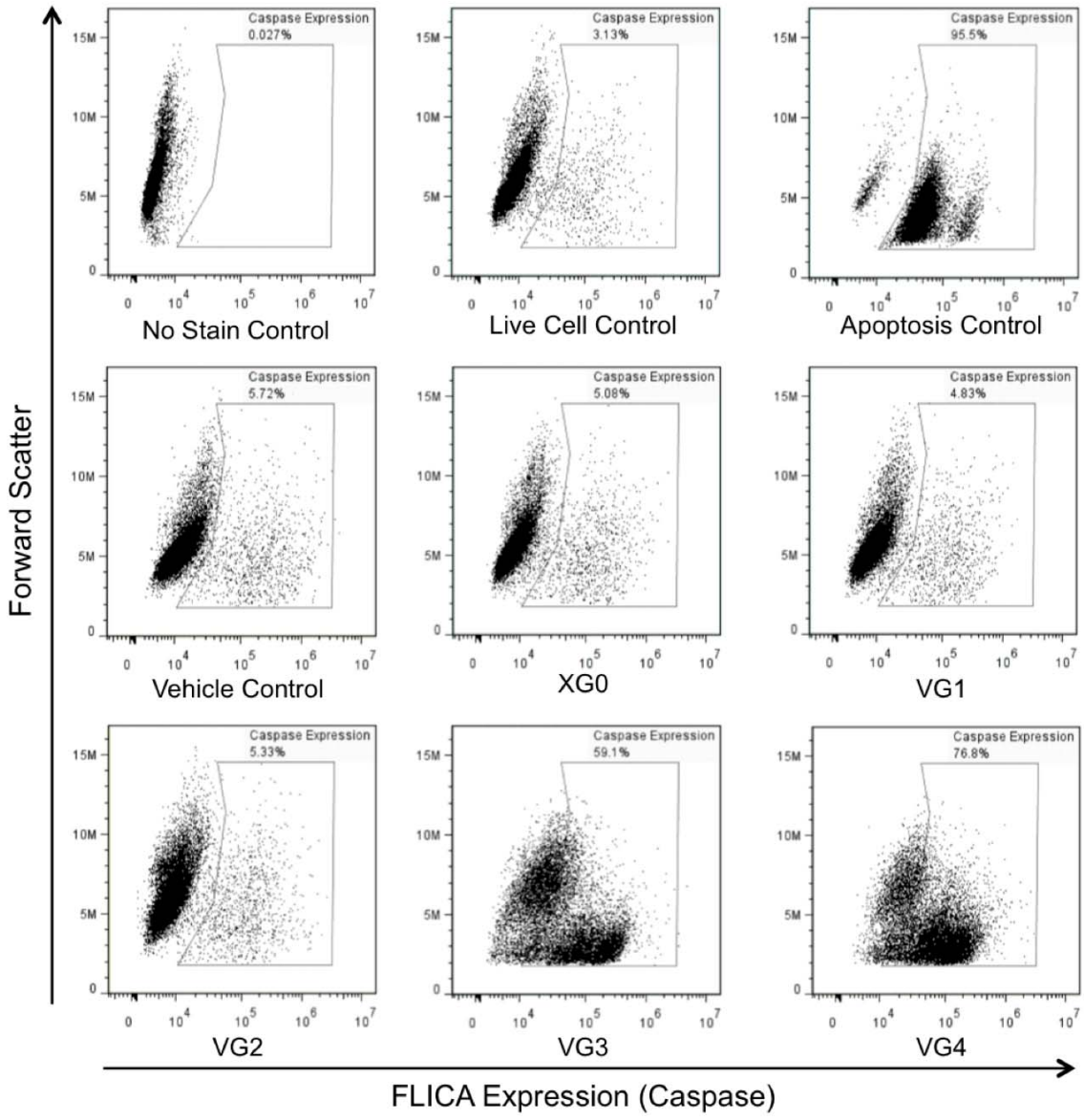

Supplemental Figure S4: Representative FLICA expression (Caspase) of HepG2 cells incubated with glass extracts for 24 hours

Chapter 9: Conclusions and Future Work

Hepatocellular carcinoma is difficult to treat due to the fact that patients are generally diagnosed once the disease has progressed to a point when curative treatments are contraindicated [54, 55]. For the majority of patients the only options are palliative therapy, of which DEB-TACE has emerged as the gold standard [5-7]. Currently materials used for DEB-TACE therapy are limited by two factors. The first is that particles are radiolucent, which has contributed to the ongoing procedural variability. Also, since physicians are unable to determine the temporal and spatial distribution within the target tissues procedures cannot be optimized for specific patients, limiting quantitative evaluation of treatment efficacy [11]. The second is that none of these particles are provided in a drug-preloaded state. As a result, particles must be loaded just prior to the procedure, which is logistically challenging and reduces shelf life [12-14].

The first original contribution of this work is entitled, *Composition-property relationships for radiopaque composite materials: pre-loaded drug-eluting beads for transarterial chemoembolization*, and was published in the Journal of Biomaterials Applications [26]. Three different constituents: DOX (therapeutic agent), Zn-Si glass (radiopacifying agent) and PLGA (embolic agent), were combined via a DOE approach to produce a radiopaque embolic particle drug-preloaded with DOX. The unique contributions of this work were (a) the application of DOE to understanding the complex composition-property relationships in a composite biomaterials, (b) the synthesis of radiopaque drug-preloaded embolic microspheres that provided for sustained release of DOX and (c) the discovery that DOX lost its cytotoxicity after seven days. The DOE

approach utilized in this study identified both first and second order interactions between the independent composition factors. Important composition-property relationships were established concerning radiopacity and density, which facilitated the synthesis of an optimized embolic agent capable of controlled release of DOX via a response surface methodology. Stage one of the work demonstrated that density was affected only by the amount of Zn-Si glass, not the PLGA, and ranged between 1.28-1.67 $g.cm^{-3}$. The radiopacity was dependent of both the PLGA and Zn-Si glass content, and ranged between 211-1450 HU. The radiopacity values were all lower than half strength contrast media (2455 HU), a commonly used radiopacifying agent in DEB-TACE procedures. All cell viabilities were between 91-106% and could not be modeled using DOE. In stage two of this work an optimized composition (23 wt% PLGA and 60 wt% glass) was predicted from the model. The optimized composition was subsequently synthesized and had a corresponding density of 1.63 ± 0.001 $g.cm^{-3}$, radiopacity of 1930 ± 44 HU and cell viability of 89±7.6 %. This composition was loaded with DOX between 0-1.4 % (wt% of PLGA) to yield radiopaque composite drug eluting beads that were capable of sustained release of DOX over seven days.

From this work it is clear that addition of Zn-Si glass to PLGA has dramatic impact on the radiopacity of the composite embolic microspheres. These measurements were performed using CT with vials of stationary particles rather than using fluoroscopy with flowing particles. From a procedural visibility perspective, it is more critical to evaluate visibility using fluoroscopy in order to establish the true clinical utility of these composites in a DEB-TACE procedure. CT evaluations are simple to perform and

provide crucial information on radiopacity of the material. However, within the literature there is no data available concerning a relationship between CT radiopacity and fluoroscopic visibility for embolic particles. A study designed to establish this relationship is necessary in order to provide guidance for developing radiopaque embolic agents. DOE is well suited for this type of study.

Another valuable next step towards developing drug-loaded composite embolic microspheres would be to establish the limits of drug loading. The study included in this work was designed as a drug loading feasibility study for a new composite system: maximum drug loading and release capabilities were not evaluated. This information is indispensable for clinical design and in order to provide particles with appropriate therapeutic levels of DOX. An important observation taken during the solvent extraction process was that the media became red while the particles formed, indicating that DOX was lost during synthesis. This indicates that the solvent extraction method may not be appropriate for manufacturing these embolic agents due to potential drug loss during particle formation. To overcome this limitation a spray-drying method may prove beneficial to minimizing loss of drug during synthesis [290]. Moreover, spray drying may prove beneficial in controlling particle size distribution and improving the drug loading/release properties [290, 291]. To establish the ability of spray-dried particles to deliver active DOX, an *in vivo* model similar to that used by Sharma et al. [16] may provide better data concerning the clinical viability of this system. However, this type of *in vivo* study should only be undertaken once an optimized radiopaque drug-loaded formulation has been identified based on the proposed studies above.

A critical finding from this work was that eluted DOX (released over seven days) from the composite embolic microspheres lost its cytotoxic effect on HepG2 cells. From the biological perspective, the *in vitro* assessment of drug elution into tissue culture water does not represent the physiological environment well and for that reason those types of studies only provide anecdotal evidence for clinical utility. It is concerning that DOX did not remain cytotoxic to HepG2 cells up to seven days, which may be due to the fact that DOX is susceptible to degradation once in solution [234, 235]. This raises a bigger question: what if DOX degrades once it has been loaded into hydrogel particles (i.e. those particles in widespread use today)? *In vitro* studies of drug-loaded microspheres exclusively evaluate drug loading and release properties but *not* drug activity [93, 101, 110]. *In vivo* studies of DOX-loaded microspheres quantify the DOX concentration and penetration depth in tissues [80, 112, 113]; however the efficacy of the DOX itself is not measured. Since DOX is known to degrade in water it is possible that hydrogel based microspheres, which are 95 % water (w/w%), may provide conditions favorable to degradation. Extended DOX release may even be irrelevant if degradation occurs before the drug can be released from the microspheres. The composite embolic microspheres developed in this thesis provide an important alternative to hydrogel-based technologies since the drug is suspended in the PLGA matrix and is *not* dissolved in water. This may limit DOX-water interactions until the drug is released from the matrix, perhaps even extending the DOX activity *in vivo*.

Previous attempts to render embolic particles radiopaque and drug-loaded, including the study mentioned above, have focused on the inclusion of multiple constituents so that each component fulfills a specific function. However, the complex and often complicated design of biomaterials has recently been criticized, as it is thought that the complexity is likely limiting the real-world clinical utility of new materials [146]. At an even more fundamental level, it has been proposed that a biomaterial should be designed to trigger host responses, using simple signals, that unlock the body's own ability of self-repair [146]. Evidence that ions released from biomedical glasses can trigger repair and regeneration of tissue is growing, and indicates that controlled release of TII can mediate a broad range of specific host responses [261]. Importantly however, research efforts in this regard have been constrained. Firstly, the development of bioactive glass systems has largely focused on applications in bone repair [24]. Secondly, much of the relevant literature has been restricted to incremental modifications of the compositional palette of the original Bioglass® formulation based on Na_2O-CaO-P_2O_5-SiO_2 [24].

It is clear from the literature that the term '*biocompatibility*' is ubiquitously associated with repair and regeneration, typically in hard tissue applications. However, considering the definition of biocompatibility (the ability of a material to perform with the appropriate **host** *and* **material** response in a particular **application** [145]) in the context of oncology, the paradigm shifts from repair to targeted destruction. Therefore, designing a *biocompatible* and *degradable* glass network capable of selectively delivering payloads of TIIs, may enable significant advances in materials technology and treatment modalities in oncology. From this perspective inorganic glass networks provide almost limitless

permutations of composition, structure, property, and function; each of which may be simultaneously engineered to control temporal and environmental degradation characteristics under physiological conditions [23].

The principles of simplicity and biocompatibility, as outlined above, are critical to the design of the final two studies in this thesis. Simple compositional changes were made to a base zinc-silicate glass system (glass A.1 from Chapter Seven) in order to test how La addition (Chapter Seven) and V addition (Chapter Eight) affect TII release from those glasses. The base zinc-silicate glass A.1 was designed to be susceptible to hydrolytic degradation due to the large mole fraction of Na_2O present in the glass. However, this was not the case. Glass A.1 was hydrolytically stable, only releasing Na in small amounts. Replacing ZnO by La_2O_3 (A series glasses) increased this stability resulting in a reduction in Na release. This prompted the development of glass B.1, which had large mole fraction of ZnO and the same mole fraction of SiO_2 as in A.1 (Chapter Seven). Glass B.1 was also resistant to hydrolytic degradation. Unlike the A series glasses, the B series glasses did release a small amount of all the ions present in the glass (Si, Zn, Na and La) however there was an order of magnitude decrease in Na release compared to the A series glasses. Replacing Na_2O by La_2O_3 (B series glasses) caused a reduction in Si and Zn release indicating. The unique contribution arising from these data is that addition of La_2O_3 resulted in stabilization of the glass network (series A and B glasses) to hydrolytic degradation, and this caused a reduction in ion release. This work is presented in the paper *Unanticipated stabilization of zinc-silicate glasses by addition of lanthanum: implications for therapeutic inorganic ion delivery systems* (under review at with the

Journal of Non-Crystalline Solids). The lack of ion release was unfortunate in the context of testing the potential therapeutic effect of La in oncology. Predictable increases in radiopacity were observed with increased La_2O_3 content; however, the poor ion releasing ability these glasses precludes using them for the localized delivery of the TII La for DEB-TACE. However the ability of La_2O_3 to stabilize the glass network against hydrolytic degradation has the potential to improve the behavior of degradable glasses for hard tissue applications. The success of tissue engineering scaffolds derived from bioactive glasses for hard tissue applications depends on striking a balance between the rate of degradation and the rate of new bone formation [25]. In two studies of identical borosilicate glasses Fu *et al.* determined that increasing the borate composition increased the ion release. Improved implant integration for 3D structures in non-loading bearing sites *in vivo* was attributed this increase in ion release [292]. However, the rapid release of ions from the 3D structures resulted in poor long-term mechanical properties, preventing their use in load bearing application [293]. Knowing that lanthanum has the ability to control ion release, it is a suitable target element for incorporation into highly degradable borate glasses, thus possibly expanding the applications for borate glasses by providing a mechanism for controlling their degradation properties. Kathleen O'Connell, a fellow PhD student, has demonstrated that La addition to a borate glass causes a reduction in the total ion release rate as well as sustained linear release of strontium, another target TII for hard tissue applications.

From the results of the lanthanum study (Chapter Seven) it is clear that addition of lanthanum to the zinc-silicates results in a reduction in the quantity of ions released,

which is undesirable from the perspective of testing the cytotoxicity of La with respect to HepG2 cells. However, this may be due to the interaction of lanthanum with zinc. It is well known that zinc is a network intermediate and can therefore behave as a former or a modifier. Based on the behavior of the two La-free glasses (A.1 and B.1), it appears that zinc stabilizes the network like a network former. In order to confirm the role of zinc, the structure of the glass network needs to be evaluated beyond the silicate network. It may be possible to produce a glass using an oxide that has been doped with an isotope of oxygen that is NMR active (^{17}O). The oxygen environment could then be evaluated using MAS NMR and may shed light on the coordination state of oxygen in the glass. Correlating ion release to oxygen structure may provide a new method for designing glasses with desired properties. From a fundamental perspective, confirming the existence of increased oxygen bonding would require terminology like network connectivity, bridging oxygen and non-bridging oxygen to be refined to reflect this structural possibility.

Other elements that can be evaluated using NMR are ^{139}La and ^{67}Zn. ^{139}La solid state NMR is an emerging area of study. Currently, ^{139}La solid state NMR is technically difficult since ^{139}La has a nuclear spin of 7/2, a large quadrupole moment and spectra are very broad [294]. For these reasons ^{139}La is performed on static samples of crystalline materials [294, 295] and the techniques remains to be sufficiently validated for amorphous systems [296]. ^{67}Zn has a nuclear spin of 5/2 making NMR studies difficult to perform. The quadrupole interaction causes significant peak broadening. The low natural abundance and small magnetic moment confound this problem further [297]. Therefore,

to probe the local structure around La and Zn, it would be appropriate to use multiple spectroscopy techniques i.e. Raman, Fourier transform infrared (FT-IR), EXFAS and X-ray absorption near edge structure (XANES). Combining this data together would provide a better understanding of the nearest and next nearest neighbors for all elements in the glass and may be able to confirm or refute the presence of mixed cation clusters. From an application standpoint, understanding the interactions of lanthanum and zinc with each other and other glass components may provide a means to control and predict glass properties aside from using the network connectivity model.

From the perspective of developing a La-releasing glass from a silicate system, an investigation into inverted glass compositions is a promising avenue for research. Typically inverted glasses have limited use in biomedical applications due to their rapid dissolution, which may compromise performance in hard tissue applications [155]. Current research concerning inverted glass systems is focused on improving melt-handling characteristics and reducing ion release rate [298-301]. It is clear from Chapter Seven that addition of La to a zinc-silicate causes a reduction in the ion release rate. This feature may prove to beneficial in inverted glass systems where ion release is rapid and by facilitate appropriate TII release. Yet, in the context of vectored delivery of La in oncology, increased ion release is a desired outcome and thus a balance will need to be struck between durability and degradability. However, as demonstrated in the work of O'Connell (described above), borate glass degradation can be controlled by addition of La in order to release a different target TII, in particular Sr (*Linear Release of Strontium*

Ions from High Borate Glasses Via Lanthanide/Alkali Substitutions, currently under review at the Journal of Non-Crystalline solids).

In study three (Chapter Eight), *Stimulation of Apoptotic Pathways in Liver Cancer Cells: an Alternative Perspective on the Biocompatibility and the Utility of Biomedical Glasses* (submitted to BioMetals), the behavior of vanadium was dramatically different from lanthanum in similar zinc-silicate glass systems. Addition of vanadium caused the silicate network to polymerize while simultaneously and surprisingly increasing TII release capabilities. Solid-state ^{51}V NMR demonstrated that vanadium was present in the network as sodium metavanadate like structures, indicating that sodium was being sequestered from the silica network and likely resulted in the silicate network polymerization. Since sodium metavanadate is highly soluble, it is probable that these structures are susceptible to hydrolytic degradation and therefore causes the increased TII release. HepG2 cells exposed to these extracts demonstrated concentration-dependent cytotoxic responses, where increased TII concentration resulted in significantly greater cell death. Using flow cytometry, it was determined that the mechanism of cell death was an extrinsic apoptosis pathway activated by caspase 8.

The selective release of sodium and vanadium from the zinc-silicate was a surprising result considering that the silicate network was more highly polymerized with the addition of vanadium. From a structural perspective, the bonding relationship between vanadium and silicon is still unknown. The presence of V-O-Si bonds has not been identified directly and a study evaluating this (the presence or absence of these bonds)

may help to shed light on the mechanism of ion release from these glasses. It would also be interesting to further investigate the behavior of vanadium in the glasses. One obvious question to ask is whether different alkali metals affect the vanadium structure; i.e. would vanadium still enter the glass network in a metavanadate like structure with the different alkali metals? Evaluation of the ion release properties of zinc-silicates with different alkali metals may provide more information concerning the mechanism of vanadium release.

It was disappointing that the radiopacity of the vanadium containing glasses was lower than standard non-ionic contrast agents (2455 HU [26]). It may be possible to improve the radiopacity of these glasses by addition of elements known to positively impact this property. Lanthanum is an excellent candidate since it dramatically increases the radiopacity of the zinc-silicates with similar compositions to the vanadium-containing glasses, as shown in Chapter Seven. Comparing the behavior of La and V in the same zinc-silicate system reveals that V sequesters Na from the Si network causing polymerization, while La does not appear to alter the Si network. It has been hypothesized that La forms mixed cation clusters, most likely with Zn. Considered together, these two results suggest that V may preferentially interact with Na while La preferentially interacts with Zn. The obvious question becomes: how do V and La interact with each other? If these elements maintain similar behaviors in a glasses containing La-V-Zn-Na-Si, it may be possible to improve radiopacity while maintaining the ion release properties. Even if La causes a reduction in ion release, an optimum composition may exist that still allows for selective vanadium ion release and improved radiopacity.

The vanadium-containing glasses demonstrated dose dependent cytotoxic responses in HepG2 cells. Yet the *in vivo* efficacy of this system is unknown. Further testing is warranted to determine if these glasses have the ability to deliver cytotoxic concentrations of vanadium *in vivo*. An excellent model system is the VX2 tumor in rabbits, which is know to have similar vascular anatomy as human HCC, and is regularly used to evaluate experimental TAE therapies [103, 115, 302, 303]. The VG3 or VG4 glasses appear to be the most promising systems as they releases the most significant quantities of vanadium *in vitro*.

It appears that TII releasing glasses are better suited for treating solid tumors than hematological cancers since local TII delivery would facilitate accumulation of high TII concentrations in the solid tumor. In the case of hematological cancers, malignant cells are present throughout the entire body this necessitates systemic therapy not localized therapeutic delivery. From the perspective of DEB-TACE therapy, this thesis presents two unique and successful methods (Chapter Six and Chapter Eight) for providing radiopaque embolic materials capable of delivering a therapeutic agent at cytotoxic levels. However the broader implications of this work to bioactive glass design are obvious when one considers these glasses as delivery systems for TIIs. In the context of bioactive glass design, this work contributes to the new and innovative developments in applications beyond tissue repair and regeneration. Developing bioactive glass therapies for oncology applications forces a dramatic shift in the philosophy of therapy. Previously, the goal of bioactive glasses design was primarily centered on promoting repair and

regeneration of tissues. In this thesis, and in the context of oncology therapy, the primary treatment goal is to halt and destroy the growth of cancerous tissues. There is a periodic table full of elements previously disregarded for inclusion into bioactive glasses due to their toxic nature. It is exactly this toxic nature and their ability to cause tissue damage that makes these elements potential candidates for inclusion in bioactive glasses designed for use in oncology applications.

References

1. Ferlay J, S.I., Ervik M, Dikshit R, Eser S, Mathers C, Rebelo M, Parkin DM, Forman D, Bray, . *Cancer Incidence and Mortality Worldwide: IARC CancerBase No. 11*. GLOBOCAN 2012 v1.0 2013 [cited 2014 July 2]; Available from: http://globocan.iarc.fr.

2. Altekruse, S.F., K.A. McGlynn, and M.E. Reichman, *Hepatocellular carcinoma incidence, mortality, and survival trends in the United States from 1975 to 2005.* J Clin Oncol, 2009. **27**(9): p. 1485-91.

3. Salgia, R. and A.G. Singal, *Hepatocellular carcinoma and other liver lesions.* Med Clin North Am, 2014. **98**(1): p. 103-18.

4. Yau, T., et al., *Evolution of systemic therapy of advanced hepatocellular carcinoma.* World J Gastroenterol, 2008. **14**(42): p. 6437-41.

5. Dufour, J.F., et al., *Intermediate hepatocellular carcinoma: current treatments and future perspectives.* Ann Oncol, 2013. **24 Suppl 2**: p. ii24-9.

6. Lammer, J., et al., *Prospective randomized study of doxorubicin-eluting-bead embolization in the treatment of hepatocellular carcinoma: results of the PRECISION V study.* Cardiovasc Intervent Radiol, 2010. **33**(1): p. 41-52.

7. Huang, K., et al., *Doxorubicin-eluting Bead versus Conventional Transarterial Chemoembolization for the Treatment of HCC: a Meta-Analysis.* J Gastroenterol Hepatol, 2013.

8. Lewandowski, R.J., et al., *Transcatheter intraarterial therapies: rationale and overview.* Radiology, 2011. **259**(3): p. 641-57.

9. Martin, R., et al., *Safety and efficacy of trans arterial chemoembolization with drug-eluting beads in hepatocellular cancer: a systematic review.* Hepato-gastroenterology, 2012. **59**(113): p. 255-60.

10. Saralidze, K., et al., *Radiopaque microspheres for improved transarterial chemical embolization (TACE).* J Control Release, 2011. **152 Suppl 1**: p. e74-5.

11. Sharma, K.V., et al., *Development of "Imageable" Beads for Transcatheter Embolotherapy.* Journal of Vascular and Interventional Radiology, 2010. **21**(6): p. 865-876.

12. Lee, K.H., et al., *Doxorubicin-loaded QuadraSphere microspheres: plasma pharmacokinetics and intratumoral drug concentration in an animal model of liver cancer.* Cardiovascular and Interventional Radiology, 2010. **33**(3): p. 576-82.

13. Lewis, A.L., et al., *DC bead: In vitro characterization of a drug-delivery device for transarterial chemoembolization.* Journal of Vascular and Interventional Radiology, 2006. **17**(2): p. 335-342.

14. Bruix, J., et al., *Transarterial embolization versus symptomatic treatment in patients with advanced hepatocellular carcinoma: results of a randomized, controlled trial in a single institution.* Hepatology, 1998. **27**(6): p. 1578-83.

15. Lewis, A.L. and M.R. Dreher, *Locoregional drug delivery using image-guided intra-arterial drug eluting bead therapy.* Journal of Controlled Release, 2012. **161**(2): p. 338-350.

16. Dreher, M.R., et al., *Radiopaque drug-eluting beads for transcatheter embolotherapy: experimental study of drug penetration and coverage in swine.* J Vasc Interv Radiol, 2012. **23**(2): p. 257-64 e4.

17. Lu, X.J., et al., *Research of novel biocompatible radiopaque microcapsules for arterial embolization.* Int J Pharm, 2013. **452**(1-2): p. 211-9.

18. Kehoe, S., et al., *Mixture designs to assess composition-structure-property relationships in SiO(2)-CaO-ZnO-La(2)O(3)-TiO(2)-MgO-SrO-Na(2)O glasses: potential materials for embolization.* J Biomater Appl, 2013. **28**(3): p. 416-33.

19. Kehoe, S., et al., *Predicting the thermal responses and radiopacity of multicomponent zinc–silicate bioglasses: A focus on ZnO, La2O3, SiO2 and TiO2.* Journal of Non-Crystalline Solids, 2012. **358**(23): p. 3388-3395.

20. Kehoe, S., R. Abraham, and D. Boyd, *Unilateral renal artery embolization in Yucutan miniswine with imageable embolic microspheres.* Journal of Vascular and Interventional Radiology. **26**(2): p. S79-S80.

21. Kehoe, S., N. Kilcup, and D. Boyd, *Evaluation of cytotoxicity for novel composite embolic microspheres: Material optimization by response surface methodology.* Materials Letters, 2012. **86**(0): p. 13-17.

22. Lakhkar, N.J., et al., *Bone formation controlled by biologically relevant inorganic ions: role and controlled delivery from phosphate-based glasses.* Adv Drug Deliv Rev, 2013. **65**(4): p. 405-20.

23. Hoppe, A., N.S. Guldal, and A.R. Boccaccini, *A review of the biological response to ionic dissolution products from bioactive glasses and glass-ceramics.* Biomaterials, 2011. **32**(11): p. 2757-74.

24. Hench, L.L. and J.M. Polak, *Third-generation biomedical materials.* Science, 2002. **295**(5557): p. 1014-+.

25. Hench, L.L., I.D. Xynos, and J.M. Polak, *Bioactive glasses for in situ tissue regeneration.* J Biomater Sci Polym Ed, 2004. **15**(4): p. 543-62.

26. Kilcup, N., et al., *Composition-property relationships for radiopaque composite materials: pre-loaded drug-eluting beads for transarterial chemoembolization.* J Biomater Appl, 2015. **30**(1): p. 93-103.

27. El-Serag, H.B. and K.L. Rudolph, *Hepatocellular carcinoma: epidemiology and molecular carcinogenesis.* Gastroenterology, 2007. **132**(7): p. 2557-76.

28. Davis, G.L. and W.L. Roberts, *The healthcare burden imposed by liver disease in aging Baby Boomers.* Curr Gastroenterol Rep, 2010. **12**(1): p. 1-6.

29. Calle, E.E., et al., *Overweight, obesity, and mortality from cancer in a prospectively studied cohort of U.S. adults.* N Engl J Med, 2003. **348**(17): p. 1625-38.

30. Duan, X.F., et al., *Obesity, adipokines and hepatocellular carcinoma.* Int J Cancer, 2013. **133**(8): p. 1776-83.

31. El-Serag, H.B., T. Tran, and J.E. Everhart, *Diabetes increases the risk of chronic liver disease and hepatocellular carcinoma.* Gastroenterology, 2004. **126**(2): p. 460-8.

32. Donadon, M., et al., *New paradigm in the management of liver-only metastases from colorectal cancer.* Gastrointest Cancer Res, 2007. **1**(1): p. 20-7.

33. Abdalla, E.K., et al., *Improving resectability of hepatic colorectal metastases: expert consensus statement.* Ann Surg Oncol, 2006. **13**(10): p. 1271-80.

34. Minocha, J., R. Salem, and R.J. Lewandowski, *Transarterial chemoembolization and yittrium-90 for liver cancer and other lesions.* Clin Liver Dis, 2014. **18**(4): p. 877-90.

35. Binefa, G., et al., *Colorectal cancer: from prevention to personalized medicine.* World J Gastroenterol, 2014. **20**(22): p. 6786-808.

36. Schutte, K., J. Bornschein, and P. Malfertheiner, *Hepatocellular carcinoma--epidemiological trends and risk factors.* Dig Dis, 2009. **27**(2): p. 80-92.

37. Patel, M., et al., *Hepatocellular carcinoma: diagnostics and screening.* Journal of Evaluation in Clinical Practice, 2010: p. no-no.

38. Pazgan-Simon, M., et al., *Diagnostic challenges in primary hepatocellular carcinoma: case reports and review of the literature.* Case Rep Oncol Med, 2015. **2015**: p. 878763.

39. Baffy, G., E.M. Brunt, and S.H. Caldwell, *Hepatocellular carcinoma in non-alcoholic fatty liver disease: an emerging menace.* Journal of Hepatology, 2012. **56**(6): p. 1384-91.

40. Silverthorn, D.U., *Digestion*, in *Human Physiology: An Intergrated Approach*, D.U. Silverthorn, Editor. 1998, Prentice -Hall Inc: New Jersey. p. 592-95.

41. Silverthorn, D.U., *Integrative Physiology III: Exercise*, in *Human Physiology: An Integrated Approach*, D.U. Silverthorn, Editor. 1998, Prentice-Hall Inc: New Jersey. p. 684-86.

42. Silverthorn, D.U., *Endocrine Control of Metabolism and Growth*, in *Human Physiology: an Integrated Approach* 1998, Prentice Hall: New Jersey, USA. p. 623.

43. Attwa, M.H. and S.A. El-Etreby, *Guide for diagnosis and treatment of hepatocellular carcinoma.* World J Hepatol, 2015. **7**(12): p. 1632-51.

44. Huether, S., *Structure and Function of the Digestive System*, in *Understanding Pathophysiology*, S.M. Huether, K, Editor. 2008, Mosby Elsevier: St. Louis, Missouri. p. 925-30.

45. Tortora, J. and M. Nielsen, *The Digestive System*, in *Principles of Human Anatomy*. 2009, John Wiley and Sons, Inc. p. 800-801.

46. Thorgeirsson, S.S. and J.W. Grisham, *Molecular pathogenesis of human hepatocellular carcinoma.* Nature genetics, 2002. **31**(4): p. 339-46.

47. Virshup, D.M.M., K.L., *Biology of Cancer and Tumor Spread*, in *Understanding Pathophysiology*, S.M. Huether, K., Editor. 2004, Mosby Elsevier St. Louis, MO. p. 228-31.

48. Tanaka, S. and S. Arii, *Current status of molecularly targeted therapy for hepatocellular carcinoma: basic science.* International journal of clinical oncology / Japan Society of Clinical Oncology, 2010. **15**(3): p. 235-41.

49. Marrero, J.A. and T. Welling, *Modern diagnosis and management of hepatocellular carcinoma.* Clin Liver Dis, 2009. **13**(2): p. 233-47.

50. Lucey, M.R., et al., *Minimal criteria for placement of adults on the liver transplant waiting list: a report of a national conference organized by the American Society of Transplant Physicians and the American Association for the Study of Liver Diseases.* Transplantation, 1998. **66**(7): p. 956-62.

51. Pugh, R.N.H., et al., *Transection of the oesophagus for bleeding oesophageal varices.* British Journal of Surgery, 1973. **60**(8): p. 646-649.

52. Addissie, B.D. and L.R. Roberts, *Classification and Staging of Hepatocellular Carcinoma: An Aid to Clinical Decision-Making.* Clin Liver Dis, 2015. **19**(2): p. 277-294.

53. Llovet, J.M. and J. Bruix, *Novel advancements in the management of hepatocellular carcinoma in 2008.* J Hepatol, 2008. **48 Suppl 1**: p. S20-37.

54. El-Serag, H.B., et al., *The continuing increase in the incidence of hepatocellular carcinoma in the United States: an update.* Annals of internal medicine, 2003. **139**(10): p. 817-23.

55. Stefaniuk, P., J. Cianciara, and A. Wiercinska-Drapalo, *Present and future possibilities for early diagnosis of hepatocellular carcinoma.* World journal of gastroenterology : WJG, 2010. **16**(4): p. 418-24.

56. Llovet, J.M. and J. Bruix, *Systematic review of randomized trials for unresectable hepatocellular carcinoma: Chemoembolization improves survival.* Hepatology, 2003. **37**(2): p. 429-42.

57. Yang, J.D. and L.R. Roberts, *Epidemiology and management of hepatocellular carcinoma.* Infectious disease clinics of North America, 2010. **24**(4): p. 899-919, viii.

58. Ramakrishna, G., et al., *Role of cellular senescence in hepatic wound healing and carcinogenesis.* European Journal of Cell Biology, 2012. **91**(10): p. 739-747.

59. Kumar, M. and D. Panda, *Role of supportive care for terminal stage hepatocellular carcinoma.* J Clin Exp Hepatol, 2014. **4**(Suppl 3): p. S130-9.

60. Okada, S., *Chemotherapy in hepatocellular carcinoma.* Hepato-gastroenterology, 1998. **45 Suppl 3**: p. 1259-63.

61. Schwartz, J.D. and A.S. Beutler, *Therapy for unresectable hepatocellular carcinoma: review of the randomized clinical trials-II: systemic and local non-embolization-based therapies in unresectable and advanced hepatocellular carcinoma.* Anti-cancer drugs, 2004. **15**(5): p. 439-52.

62. Llovet, J.M., et al., *Sorafenib in advanced hepatocellular carcinoma.* The New England journal of medicine, 2008. **359**(4): p. 378-90.

63. Gaya, A., et al., *The use of temozolomide in recurrent malignant gliomas.* Cancer Treat Rev, 2002. **28**(2): p. 115-20.

64. Oronsky, B.T., et al., *The scarlet letter of alkylation: a mini review of selective alkylating agents.* Translational oncology, 2012. **5**(4): p. 226-9.

65. Ang, S.F., et al., *Activity of thalidomide and capecitabine in patients with advanced hepatocellular carcinoma.* American journal of clinical oncology, 2012. **35**(3): p. 222-7.

66. Walko, C.M. and C. Lindley, *Capecitabine: a review.* Clin Ther, 2005. **27**(1): p. 23-44.

67. Di Maio, M., et al., *Hepatocellular carcinoma: systemic treatments.* Journal of clinical gastroenterology, 2002. **35**(5 Suppl 2): p. S109-14.

68. Slichenmyer, W.J. and D.D. Von Hoff, *New natural products in cancer chemotherapy.* J Clin Pharmacol, 1990. **30**(9): p. 770-88.

69. Ohtsubo, K., et al., *Advanced hepatocellular carcinoma treated effectively with irinotecan via hepatic arterial infusion followed by proton beam therapy.* Journal of infection and chemotherapy : official journal of the Japan Society of Chemotherapy, 2009. **15**(5): p. 316-21.

70. McCance, K.B., P, *Cancer Epidemiology, Manifestations, and Treatment*, in *Understanding Pathophysiology*, S. Huether, Editor. 2004, Mosby Elsevier: St. Louis, Missouri. p. 257-62.

71. Gramenzi, A., et al., *Yttrium-90 radioembolization vs sorafenib for intermediate-locally advanced hepatocellular carcinoma: a cohort study with propensity score analysis.* Liver Int, 2015. **35**(3): p. 1036-47.

72. Lewandowski, R.J., et al., *A comparative analysis of transarterial downstaging for hepatocellular carcinoma: chemoembolization versus radioembolization.* Am J Transplant, 2009. **9**(8): p. 1920-8.

73. Associates, A.T. *About the Liver*. Health Topics 2012 [cited 2012 October 14, 2012]; Available from: http://www.arizonatransplant.com/healthtopics/liver.html.

74. Ottawa, U.o. *The Liver*. Histology [cited 2012 November 12, 2012]; Available from: http://www.courseweb.uottawa.ca/medicine-histology/english/gastrointestinal/Liver.htm.

75. Patel, J., *Liver Tumors (Hepatocellular Carcinoma)*, in *Transcatheter Embolization and Therapy*, D. Kessel, ; Ray, C, Editor. 2010, Springer: London, UK. p. 185.

76. *Hepatocellular Carcinoma (Liver Cancer):Therapy*. Gastroentorology and Hepatology 2011 [cited 2012 November 16]; Available from: http://www.hopkins-gi.org/Upload/200710291022_14392_000.jpg.

77. I, D. *Chemoembolization*. 2015 [cited 2015 May 29, 2015]; Available from: http://www.dedesioannis.com/en/tumor-chemoembolization/.

78. Rand, T., et al., *Arterial embolization of unresectable hepatocellular carcinoma with use of microspheres, lipiodol, and cyanoacrylate.* Cardiovascular and Interventional Radiology, 2005. **28**(3): p. 313-318.

79. Idee, J.M. and B. Guiu, *Use of Lipiodol as a drug-delivery system for transcatheter arterial chemoembolization of hepatocellular carcinoma: a review.* Crit Rev Oncol Hematol, 2013. **88**(3): p. 530-49.

80. Varela, M., et al., *Chemoembolization of hepatocellular carcinoma with drug eluting beads: efficacy and doxorubicin pharmacokinetics.* J Hepatol, 2007. **46**(3): p. 474-81.

81. Habib, A., et al., *Locoregional Therapy of Hepatocellular Carcinoma.* Clin Liver Dis, 2015. **19**(2): p. 401-420.

82. Gates, V.L., et al., *Radioembolization with Yttrium-90 microspheres: review of an emerging treatment for liver tumors.* Future oncology (London, England), 2007. **3**(1): p. 73-81.

83. *TheraSphere® Yttrium-90 Glass Microspheres*. [cited 2012 November 24]; Package Insert].

84. Ahmadzadehfar, H., et al., *The Significance of Tc-99m-MAA SPECT/CT Liver Perfusion Imaging in Treatment Planning for Y-90-Microsphere Selective Internal Radiation Treatment.* Journal of Nuclear Medicine, 2010. **51**(8): p. 1206-1212.

85. Edeline, J., et al., *Yttrium-90 microsphere radioembolization for hepatocellular carcinoma.* Liver Cancer, 2015. **4**(1): p. 16-25.

86. Salem, R., et al., *Radioembolization Results in Longer Time-to-Progression and Reduced Toxicity Compared With Chemoembolization in Patients With Hepatocellular Carcinoma.* Gastroenterology, 2011. **140**(2): p. 497-507.e2.

87. Pitton, M.B., et al., *Randomized comparison of selective internal radiotherapy (SIRT) versus drug-eluting bead transarterial chemoembolization (DEB-TACE) for the treatment of hepatocellular carcinoma.* Cardiovasc Intervent Radiol, 2015. **38**(2): p. 352-60.

88. Boily, G., et al., *Transarterial embolization therapies for the treatment of hepatocellular carcinoma: CEPO review and clinical recommendations.* HPB (Oxford), 2015. **17**(1): p. 52-65.

89. Peixoto, L.S., et al., *Synthesis of poly(vinyl alcohol) and/or poly(vinyl acetate) particles with spherical morphology and core-shell structure and its use in vascular embolization.* Macromolecular Symposia, 2006. **243**: p. 190-199.

90. Gnanou, Y. and M. Fontanille, *Organic and Physical Chemistry of Polymers*. 2008, Hoboken, N.J.: Wiley-Interscience.

91. Lyoo, W.S. and H.W. Lee, *Synthesis of high-molecular-weight poly(vinyl alcohol) with high yield by novel one-batch suspension polymerization of vinyl acetate and saponification.* Colloid and Polymer Science, 2002. **280**(9): p. 835-840.

92. Limited, B.U. *DC Bead*. 2012 [cited 2012 April 10]; Available from: http://www.biocompatibles.com/products/dcbead.

93. Lewis, A.L., et al., *Doxorubicin eluting beads - 1: effects of drug loading on bead characteristics and drug distribution.* J Mater Sci Mater Med, 2007. **18**(9): p. 1691-9.

94. Asfaw, B.T., et al., *Embolic compositions*. 2001, Google Patents.

95. Malagari, K., *Drug-eluting particles in the treatment of HCC: chemoembolization with doxorubicin-loaded DC Bead.* Expert review of anticancer therapy, 2008. **8**(10): p. 1643-50.

96. Grosso, M., et al., *Transarterial chemoembolization for hepatocellular carcinoma with drug-eluting microspheres: preliminary results from an Italian multicentre study*. Cardiovascular and Interventional Radiology, 2008. **31**(6): p. 1141-9.

97. Jiaqi, Y., et al., *[A new embolic material: super absorbent polymer (SAP) microsphere and its embolic effects]*. Nihon Igaku Hoshasen Gakkai zasshi. Nippon acta radiologica, 1996. **56**(1): p. 19-24.

98. Tanimoto, D., et al., *Observation of Intravascular Changes of Superabsorbent Polymer Microsphere (SAP-MS) with Monochromatic X-Ray Imaging.* Cardiovascular and Interventional Radiology, 2010. **33**(5): p. 1016-1021.

99. Biondi, M., et al., *New Insights into the Mechanisms of the Interactions Between Doxorubicin and the Ion-Exchange Hydrogel DC Bead T for Use in Transarterial Chemoembolization (TACE)*. Journal of Biomaterials Science-Polymer Edition, 2012. **23**(1-4): p. 333-354.

100. Lewis, A.L. and R.R. Holden, *DC Bead embolic drug-eluting bead: clinical application in the locoregional treatment of tumours.* Expert Opinion on Drug Delivery, 2011. **8**(2): p. 153-169.

101. Liu, D.M., et al., *Optimization of doxorubicin loading for superabsorbent polymer microspheres: in vitro analysis.* Cardiovascular and Interventional Radiology, 2012. **35**(2): p. 391-8.

102. Huppert, P., T. Wenzel, and H. Wietholtz, *Transcatheter arterial chemoembolization (TACE) of colorectal cancer liver metastases by irinotecan-eluting microspheres in a salvage patient population.* Cardiovasc Intervent Radiol, 2014. **37**(1): p. 154-64.

103. Tanaka, T., et al., *Pharmacokinetics and antitumor efficacy of chemoembolization using 40 microm irinotecan-loaded microspheres in a rabbit liver tumor model.* J Vasc Interv Radiol, 2014. **25**(7): p. 1037-1044 e2.

104. *INSTRUCTIONS FOR USE: DC Bead Drug Delivery Embolisation System*. 2012 [cited 2012 November 22]; Available from: http://assets.biocompatibles.com/products/uploads/Files/instructions/dcbead/DC Bead IFU - English.pdf.

105. *HepaSphere™ Microspheres (With Doxorubicin) IFU- Canada (English/French)*. 2011 [cited 2015 May 5]; Available from: http://www.merit.com/products/media.aspx?type=ifu&id=327961.

106. Jordan, O., et al., *Comparative Study of Chemoembolization Loadable Beads: In vitro Drug Release and Physical Properties of DC Bead and Hepasphere Loaded with Doxorubicin and Irinotecan.* Journal of Vascular and Interventional Radiology, 2010. **21**(7): p. 1084-1090.

107. Malagari, K., et al., *Transarterial chemoembolization of unresectable hepatocellular carcinoma with drug eluting beads: results of an open-label study of 62 patients.* Cardiovasc Intervent Radiol, 2008. **31**(2): p. 269-80.

108. Muller, H.J., et al., *The influence of liver metastases on the pharmacokinetics of doxorubicin---a population-based pharmacokinetic project of the CESAR-APOH.* Int J Clin Pharmacol Ther, 2003. **41**(12): p. 598-9.

109. Lefrak, E.A., et al., *A clinicopathologic analysis of adriamycin cardiotoxicity.* Cancer, 1973. **32**(2): p. 302-14.

110. Gonzalez, M.V., et al., *Doxorubicin eluting beads-2: methods for evaluating drug elution and in-vitro:in-vivo correlation.* J Mater Sci Mater Med, 2008. **19**(2): p. 767-75.

111. Kos, S., et al., *Elution characteristics of doxorubicin-loaded microspheres differ by drug-loading method and microsphere size.* J Vasc Interv Radiol, 2011. **22**(3): p. 361-8.

112. Namur, J., et al., *Drug-eluting beads for liver embolization: concentration of doxorubicin in tissue and in beads in a pig model.* Journal of vascular and interventional radiology : JVIR, 2010. **21**(2): p. 259-67.

113. Namur, J., et al., *Embolization of hepatocellular carcinoma with drug-eluting beads: doxorubicin tissue concentration and distribution in patient liver explants.* Journal of Hepatology, 2011. **55**(6): p. 1332-8.

114. Spies, J.B., *Uterine artery embolization for fibroids: understanding the technical causes of failure.* J Vasc Interv Radiol, 2003. **14**(1): p. 11-4.

115. Gupta, S., et al., *Hepatic arterial embolization with doxorubicin-loaded superabsorbent polymer microspheres in a rabbit liver tumor model.* Cardiovascular and Interventional Radiology, 2011. **34**(5): p. 1021-30.

116. Malagari, K., et al., *Chemoembolization of hepatocellular carcinoma with HepaSphere 30-60 mum. Safety and efficacy study.* Cardiovasc Intervent Radiol, 2014. **37**(1): p. 165-75.

117. Malagari, K., et al., *Prospective Randomized Comparison of Chemoembolization with Doxorubicin-Eluting Beads and Bland Embolization with BeadBlock for Hepatocellular Carcinoma.* Cardiovascular and Interventional Radiology, 2010. **33**(3): p. 541-551.

118. Meza-Junco, J., et al., *Locoregional radiological treatment for hepatocellular carcinoma; Which, when and how?* Cancer Treatment Reviews, 2012. **38**(1): p. 54-62.

119. Song, M.J., et al., *Comparative study between doxorubicin-eluting beads and conventional transarterial chemoembolization for treatment of hepatocellular carcinoma.* Journal of Hepatology, 2012. **57**(6): p. 1244-1250.

120. Xie, Z.B., et al., *Systematic review comparing the safety and efficacy of conventional and drug-eluting bead transarterial chemoembolization for inoperable hepatocellular carcinoma.* Hepatol Res, 2015. **45**(2): p. 190-200.

121. Huang, K., et al., *Doxorubicin-eluting beads versus conventional transarterial chemoembolization for the treatment of hepatocellular carcinoma.* J Gastroenterol Hepatol, 2014. **29**(5): p. 920-5.

122. Bilbao, J.I., et al., *Comparative study of four different spherical embolic particles in an animal model: a morphologic and histologic evaluation.* J Vasc Interv Radiol, 2008. **19**(11): p. 1625-38.

123. Beaujeux, R., et al., *Trisacryl gelatin microspheres for therapeutic embolization .2. Preliminary clinical evaluation in tumors and arteriovenous malformations.* American Journal of Neuroradiology, 1996. **17**(3): p. 541-548.

124. Spies, J.B., et al., *Spherical polyvinyl alcohol versus tris-acryl gelatin microspheres for uterine artery embolization for leiomyomas: Results of a limited randomized comparative study.* Journal of Vascular and Interventional Radiology, 2005. **16**(11): p. 1431-1437.

125. Spies, J.B., *What Evidence Should We Demand before Accepting a New Embolic Material for Uterine Artery Embolization?* Journal of Vascular and Interventional Radiology, 2009. **20**(5): p. 567-570.

126. Siskin, G.P., et al., *Pathologic evaluation of a spherical polyvinyl alcohol embolic agent in a porcine renal model.* Journal of Vascular and Interventional Radiology, 2003. **14**(1): p. 89-98.

127. Scientific, B. *PERIPHERAL INTERVENTIONS 2014 Product Catalog* 2014 [cited 2015 July 27, 2015]; Available from: http://www.bostonscientific.com/content/dam/bostonscientific/pi/portfolio-group/resources/ProductCatalog/PI-2014-Product-Catalog-Embolization.pdf/.

128. Vente, M.A.D., B.A. Zonnenberg, and J.F.W. Nijsen, *Microspheres for radioembolization of liver malignancies.* Expert Review of Medical Devices, 2010. **7**(5): p. 581-583.

129. Jones, J.R., *Review of bioactive glass: From Hench to hybrids.* Acta Biomaterialia, 2013. **9**(1): p. 4457-86.

130. Chen, L., H. Shen, and B.I. Suh, *Bioactive dental restorative materials: a review.* Am J Dent, 2013. **26**(4): p. 219-27.

131. Jell, G. and M.M. Stevens, *Gene activation by bioactive glasses.* J Mater Sci Mater Med, 2006. **17**(11): p. 997-1002.

132. Gu, Z., et al., *Application of strontium-doped calcium polyphosphate scaffold on angiogenesis for bone tissue engineering.* J Mater Sci Mater Med, 2013. **24**(5): p. 1251-60.

133. Wu, C., et al., *Hypoxia-mimicking mesoporous bioactive glass scaffolds with controllable cobalt ion release for bone tissue engineering.* Biomaterials, 2012. **33**(7): p. 2076-85.

134. Li, Q.F., X.Q. Ding, and Y.J. Kang, *Copper promotion of angiogenesis in isolated rat aortic ring: role of vascular endothelial growth factor.* J Nutr Biochem, 2014. **25**(1): p. 44-9.

135. Wu, C., et al., *Copper-containing mesoporous bioactive glass scaffolds with multifunctional properties of angiogenesis capacity, osteostimulation and antibacterial activity.* Biomaterials, 2013. **34**(2): p. 422-33.

136. Luo, L., et al., *Effect of cobalt and chromium ions on MMP-1, TIMP-1, and TNF-alpha gene expression in human U937 macrophages: a role for tyrosine kinases.* Biomaterials, 2005. **26**(28): p. 5587-93.

137. Fielding, G.A., W. Smoot, and S. Bose, *Effects of SiO2, SrO, MgO, and ZnO dopants in tricalcium phosphates on osteoblastic Runx2 expression.* J Biomed Mater Res A, 2014. **102**(7): p. 2417-26.

138. Miguez-Pacheco, V., L.L. Hench, and A.R. Boccaccini, *Bioactive glasses beyond bone and teeth: emerging applications in contact with soft tissues.* Acta Biomater, 2015. **13**: p. 1-15.

139. Memon, K., et al., *Radioembolization for primary and metastatic liver cancer.* Semin Radiat Oncol, 2011. **21**(4): p. 294-302.

140. Vallet-Regi, M. and E. Ruiz-Hernandez, *Bioceramics: from bone regeneration to cancer nanomedicine.* Adv Mater, 2011. **23**(44): p. 5177-218.

141. O., H.L.L.A., *An Introduction to Bioceramics*. 1983, Singapore: World Scientific.

142. Hench, L.L. and J. Wilson, *SURFACE-ACTIVE BIOMATERIALS.* Science, 1984. **226**(4675): p. 630-636.

143. Fujishiro, Y., L.L. Hench, and H. Oonishi, *Quantitative rates of in vivo bone generation for Bioglass and hydroxyapatite particles as bone graft substitute.* J Mater Sci Mater Med, 1997. **8**(11): p. 649-52.

144. Valimaki, V.V. and H.T. Aro, *Molecular basis for action of bioactive glasses as bone graft substitute.* Scandinavian Journal of Surgery, 2006. **95**(2): p. 95-102.

145. Black, J., *Biological Performance of Materials*. Fourth Edition ed. 2006, Boca Raton, FL.: CRC Press.

146. Place, E.S., N.D. Evans, and M.M. Stevens, *Complexity in biomaterials for tissue engineering.* Nature materials, 2009. **8**(6): p. 457-70.

147. Varshneya, A.K., *Fundamentals of the Glassy State*, in *Fundamentals of Inorganic Glasses*. 1994, Academic Press Inc: San Diego, CA p. 13-25.

148. Zachariasen, W.H., *The atomic arrangement in glass.* Journal of the American Chemical Society, 1932. **54**: p. 3841-3851.

149. Cooper, A.R., *ZACHARIASEN,WH - THE MELODY LINGERS ON.* Journal of Non-Crystalline Solids, 1982. **49**(1-3): p. 1-17.

150. Sun, K.H., *FUNDAMENTAL CONDITION OF GLASS FORMATION.* Journal of the American Ceramic Society, 1947. **30**(9): p. 277-281.

151. Varshneya, A.K., *Glass Formation Principles*, in *Fundamentals of Inorganic Glasses*. 1994, Academic Press: San Diego, CA. p. 27-59.

152. Dietzel, A., *Relation between surface tension and structure of glass fusions.* Kolloid-Zeitschrift, 1942. **100**(3): p. 368-380.

153. Schaller, T. and J.F. Stebbins, *The structural role of lanthanum and yttrium in aluminosilicate glasses: A Al-27 and O-17 MAS NMR study*. Journal of Physical Chemistry B, 1998. **102**(52): p. 10690-10697.

154. Charpentier, T., P. Kroll, and F. Mauri, *First-Principles Nuclear Magnetic Resonance Structural Analysis of Vitreous Silica.* Journal of Physical Chemistry C, 2009. **113**(18): p. 7917-7929.

155. Hill, R.G. and D.S. Brauer, *Predicting the bioactivity of glasses using the network connectivity or split network models.* Journal of Non-Crystalline Solids, 2011. **357**(24): p. 3884-3887.

156. O'Donnell, M.D., *Predicting bioactive glass properties from the molecular chemical composition: Glass transition temperature.* Acta Biomaterialia, 2011. **7**(5): p. 2264-2269.

157. Hill, R., *An alternative view of the degradation of bioglass.* Journal of Materials Science Letters, 1996. **15**(13): p. 1122-1125.

158. O'donnell, M.D., et al., *Effect of P2O5 content in two series of soda lime phosphosilicate glasses on structure and properties - Part I: NMR.* Journal of Non-Crystalline Solids, 2008. **354**(30): p. 3554-3560.

159. Ananthanarayanan, A., et al., *A Comparative Overview of Glass-Ceramic Characterization by MAS-NMR and XRD.* Critical Reviews in Solid State and Materials Sciences, 2011. **36**(4): p. 229-241.

160. *Chapter 4 29Si NMR*, in *Pergamon Materials Series*, J.D.M. Kenneth and E.S. Mark, Editors. 2002, Pergamon. p. 201-268.

161. O'donnell, M.D. and R.G. Hill, *Influence of strontium and the importance of glass chemistry and structure when designing bioactive glasses for bone regeneration.* Acta Biomaterialia, 2010. **6**(7): p. 2382-2385.

162. O'donnell, M.D., et al., *Effect of P2O5 content in two series of soda lime phosphosilicate glasses on structure and properties - Part II: Physical properties.* Journal of Non-Crystalline Solids, 2008. **354**(30): p. 3561-3566.

163. Doweidar, H., *The density of alkali silicate glasses in relation to the microstructure.* Journal of Non-Crystalline Solids, 1996. **194**(1-2): p. 155-162.

164. Doweidar, H., *Density-structure correlations in silicate glasses.* Journal of Non-Crystalline Solids, 1999. **249**(2-3): p. 194-200.

165. Rahaman, M.N., et al., *Bioactive glass in tissue engineering.* Acta Biomaterialia, 2011. **7**(6): p. 2355-73.

166. Edén, M., *The split network analysis for exploring composition–structure correlations in multi-component glasses: I. Rationalizing bioactivity-composition trends of bioglasses.* Journal of Non-Crystalline Solids, 2011. **357**(6): p. 1595-1602.

167. Aguiar, H., J. Serra, and P. Gonzalez, *A New Quantitative Method to Predict the Bioactive Behavior of Silicate Glasses.* Journal of the American Ceramic Society, 2012. **95**(8): p. 2554-2561.

168. Mneimne, M., et al., *High phosphate content significantly increases apatite formation of fluoride-containing bioactive glasses.* Acta Biomaterialia, 2011. **7**(4): p. 1827-34.

169. Mourino, V., J.P. Cattalini, and A.R. Boccaccini, *Metallic ions as therapeutic agents in tissue engineering scaffolds: an overview of their biological applications and strategies for new developments.* J R Soc Interface, 2012. **9**(68): p. 401-19.

170. Bose, S., et al., *Understanding of dopant-induced osteogenesis and angiogenesis in calcium phosphate ceramics.* Trends Biotechnol, 2013. **31**(10): p. 594-605.

171. Lee, I.H., et al., *Development, characterisation and biocompatibility testing of a cobalt-containing titanium phosphate-based glass for engineering of vascularized hard tissues.* Mater Sci Eng C Mater Biol Appl, 2013. **33**(4): p. 2104-12.

172. Oki, A., et al., *Preparation and in vitro bioactivity of zinc containing sol-gel-derived bioglass materials.* J Biomed Mater Res A, 2004. **69**(2): p. 216-21.

173. Saino, E., et al., *In vitro calcified matrix deposition by human osteoblasts onto a zinc-containing bioactive glass.* Eur Cell Mater, 2011. **21**: p. 59-72; discussion 72.

174. Isaac, J., et al., *Effects of strontium-doped bioactive glass on the differentiation of cultured osteogenic cells.* Eur Cell Mater, 2011. **21**: p. 130-43.

175. Wu, C., et al., *Strontium-containing mesoporous bioactive glass scaffolds with improved osteogenic/cementogenic differentiation of periodontal ligament cells for periodontal tissue engineering.* Acta Biomater, 2012. **8**(10): p. 3805-15.

176. Zhang, J., et al., *Three-dimensional printing of strontium-containing mesoporous bioactive glass scaffolds for bone regeneration.* Acta Biomater, 2014.

177. Koepf-Maier, P., *Complexes of metals other than platinum as antitumour agents.* European Journal of Clinical Pharmacology, 1994. **47**(1): p. 1-16.

178. Rosenber.B, et al., *PLATINUM COMPOUNDS - A NEW CLASS OF POTENT ANTITUMOUR AGENTS.* Nature, 1969. **222**(5191): p. 385-&.

179. Cohen, S.M. and S.J. Lippard, *Cisplatin: From DNA damage to cancer chemotherapy.* Progress in Nucleic Acid Research and Molecular Biology, Vol 67, 2001. **67**: p. 93-130.

180. Stein, A. and D. Arnold, *Oxaliplatin: a review of approved uses.* Expert Opinion on Pharmacotherapy, 2012. **13**(1): p. 125-137.

181. Desoize, B., *Metals and metal compounds in cancer treatment.* Anticancer research, 2004. **24**(3a): p. 1529-44.

182. Huang, R., A. Wallqvist, and D.G. Covell, *Anticancer metal compounds in NCI's tumor-screening database: putative mode of action.* Biochemical pharmacology, 2005. **69**(7): p. 1009-39.

183. Desoize, B., *Cancer and metals and metal compounds: part II--cancer treatment.* Critical reviews in oncology/hematology, 2002. **42**(3): p. 213-5.

184. Frezza, M., et al., *Novel Metals and Metal Complexes as Platforms for Cancer Therapy.* Current Pharmaceutical Design, 2010. **16**(16): p. 1813-1825.

185. Thompson, K.H. and C. Orvig, *Boon and bane of metal ions in medicine.* Science, 2003. **300**(5621): p. 936-9.

186. Huang, B.T., et al., *The early addition of arsenic trioxide versus high-dose arabinoside is more effective and safe as consolidation chemotherapy for risk-tailored patients with acute promyelocytic leukemia: multicenter experience.* Medical Oncology, 2012. **29**(3): p. 2088-2094.

187. Sharma, P., et al., *Perspectives of antimony compounds in oncology.* Acta Pharmacologica Sinica, 2008. **29**(8): p. 881-890.

188. Garbutcheon-Singh, K.B., et al., *Transition Metal Based Anticancer Drugs.* Current Topics in Medicinal Chemistry, 2011. **11**(5): p. 521-542.

189. Patnaik, P., *Handbook of Inorganic Chemicals*. 2003, New York, NY: McGraw-Hill.

190. Lim, S. and S.J. Franklin, *Lanthanide-binding peptides and the enzymes that Might Have Been.* Cellular and molecular life sciences : CMLS, 2004. **61**(17): p. 2184-8.

191. Tonelli, M., N. Pannu, and B. Manns, *Oral phosphate binders in patients with kidney failure.* The New England journal of medicine, 2010. **362**(14): p. 1312-24.

192. Bull, M.D., et al., *Pre-existing oral contrast from lanthanum carbonate: a confounding factor in CT mesenteric angiography.* The British journal of radiology, 2012. **85**(1012): p. e73-5.

193. Wang, K., *The analogy in chemical and biological behaviour between non-essential ions compared with essential ions.* South African Journal of Chemistry-Suid-Afrikaanse Tydskrif Vir Chemie, 1997. **50**(4): p. 232-239.

194. Dai, Y., et al., *Effects of rare earth compounds on growth and apoptosis of leukemic cell lines.* In Vitro Cell Dev Biol Anim, 2002. **38**(7): p. 373-5.

195. Su, X.G., X.N. Zheng, and J.Z. Ni, *Lanthanum citrate induces anoikis of Hela cells.* Cancer Letters, 2009. **285**(2): p. 200-209.

196. Frisch, S.M. and R.A. Screaton, *Anoikis mechanisms.* Curr Opin Cell Biol, 2001. **13**(5): p. 555-62.

197. Shi, P. and Z.W. Huang, *Proteomic detection of changes in protein synthesis induced by lanthanum in BGC-823 human gastric cancer cells.* Biometals, 2005. **18**(1): p. 89-95.

198. Zhang, Z., et al., *Telomerase-Mediated Apoptosis of Chicken Lymphoblastoid Tumor Cell Line by Lanthanum Chloride.* Biological Trace Element Research, 2011. **144**(1): p. 657-667.

199. Heffeter, P., et al., *Multidrug-resistant cancer cells are preferential targets of the new antineoplastic lanthanum compound KP772 (FFC24).* Biochemical pharmacology, 2007. **73**(12): p. 1873-1886.

200. Trumbo, P., et al., *Dietary reference intakes: vitamin A, vitamin K, arsenic, boron, chromium, copper, iodine, iron, manganese, molybdenum, nickel, silicon, vanadium, and zinc.* Journal of the American Dietetic Association, 2001. **101**(3): p. 294-301.

201. Barrio, D.A. and S.B. Etcheverry, *Vanadium and bone development: putative signaling pathways.* Canadian journal of physiology and pharmacology, 2006. **84**(7): p. 677-86.

202. Harland, B.F. and B.A. Harden-Williams, *Is vanadium of human nutritional importance yet?* Journal of the American Dietetic Association, 1994. **94**(8): p. 891-894.

203. Mukherjee, B., et al., *Vanadium--an element of atypical biological significance.* Toxicology letters, 2004. **150**(2): p. 135-43.

204. Smith, D.M., R.M. Pickering, and G.T. Lewith, *A systematic review of vanadium oral supplements for glycaemic control in type 2 diabetes mellitus.* QJM : monthly journal of the Association of Physicians, 2008. **101**(5): p. 351-8.

205. Thompson, K.H., et al., *Vanadium treatment of type 2 diabetes: a view to the future.* Journal of Inorganic Biochemistry, 2009. **103**(4): p. 554-8.

206. Cusi, K., et al., *Vanadyl sulfate improves hepatic and muscle insulin sensitivity in type 2 diabetes.* The Journal of clinical endocrinology and metabolism, 2001. **86**(3): p. 1410-7.

207. Djordjevic, C., *ANTITUMOR-ACTIVITY OF VANADIUM COMPOUNDS.* Metal Ions in Biological Systems, Vol 31, 1995. **31**: p. 595-616.

208. Thompson, H.J., N.D. Chasteen, and L.D. Meeker, *Dietary vanadyl(IV) sulfate inhibits chemically-induced mammary carcinogenesis.* Carcinogenesis, 1984. **5**(6): p. 849-51.

209. Bishayee, A. and M. Chatterjee, *INHIBITORY EFFECT OF VANADIUM ON RAT-LIVER CARCINOGENESIS INITIATED WITH DIETHYLNITROSAMINE AND PROMOTED BY PHENOBARBITAL.* British Journal of Cancer, 1995. **71**(6): p. 1214-1220.

210. Brichard, S.M. and J.-C. Henquin, *The role of vanadium in the management of diabetes.* Trends in Pharmacological Sciences, 1995. **16**(8): p. 265-270.

211. Wang, Q., et al., *Vanadium compounds discriminate hepatoma and normal hepatic cells by differential regulation of reactive oxygen species.* Journal of Biological Inorganic Chemistry, 2010. **15**(7): p. 1087-1097.

212. Evangelou, A.M., *Vanadium in cancer treatment.* Critical Reviews in Oncology Hematology, 2002. **42**(3): p. 249-265.

213. Faure, R., et al., *Arrest at the G2/M transition of the cell cycle by protein-tyrosine phosphatase inhibition: studies on a neuronal and a glial cell line.* J Cell Biochem, 1995. **59**(3): p. 389-401.

214. Liu, T.-T., et al., *Reactive-oxygen-species-mediated Cdc25C degradation results in differential antiproliferative activities of vanadate, tungstate, and molybdate in the PC-3 human prostate cancer cell line.* JBIC Journal of Biological Inorganic Chemistry, 2012. **17**(2): p. 311-320.

215. Ray, R.S., et al., *Vanadium mediated apoptosis and cell cycle arrest in MCF7 cell line.* Chemico-Biological Interactions, 2006. **163**(3): p. 239-247.

216. Matsuyoshi, N., et al., *Cadherin-mediated cell-cell adhesion is perturbed by v-src tyrosine phosphorylation in metastatic fibroblasts.* J Cell Biol, 1992. **118**(3): p. 703-14.

217. Maier, R.H., et al., *The cytotoxic interaction of inorganic trace elements with EDTA and cisplatin in sensitive and resistant human ovarian cancer cells.* In Vitro Cell Dev Biol Anim, 1997. **33**(3): p. 218-21.

218. Durgo, K., et al., *Cytotoxic and genotoxic effects of the quercetin/lanthanum complex on human cervical carcinoma cells in vitro.* Arh Hig Rada Toksikol, 2011. **62**(3): p. 221-7.

219. Shen, L., et al., *Proteomic analysis of lanthanum citrate-induced apoptosis in human cervical carcinoma SiHa cells.* Biometals, 2010. **23**(6): p. 1179-89.

220. Bunker, B.C., R.J. Kirkpatrick, and R.K. Brow, *Local-Structure of Alkaline-Earth Boroaluminate Crystals and Glasses .1., Crystal Chemical Concepts Structural Predictions and Comparisons to Known Crystal-Structures.* Journal of the American Ceramic Society, 1991. **74**(6): p. 1425-1429.

221. Bishayee, A., et al., *Vanadium in the detection, prevention and treatment of cancer: The in vivo evidence.* Cancer Letters, 2010. **294**(1): p. 1-12.

222. Molinuevo, M.S., A.M. Cortizo, and S.B. Etcheverry, *Vanadium(IV) complexes inhibit adhesion, migration and colony formation of UMR106 osteosarcoma cells.* Cancer Chemother Pharmacol, 2008. **61**(5): p. 767-73.

223. Forster, R., et al., *Comparison of DC Bead-irinotecan and DC Bead-topotecan drug eluting beads for use in locoregional drug delivery to treat pancreatic cancer.* Journal of Materials Science: Materials in Medicine, 2010. **21**(9): p. 2683-2690.

224. Kritzinger, J., et al., *Hepatic embolotherapy in interventional oncology: Technology, techniques, and applications.* Clinical radiology, 2012.

225. Kehoe, S., et al., *Effects of gamma-irradiation and accelerated aging on composition-structure-property relationships for radiopaque embolic microspheres.* Journal of Non-Crystalline Solids, 2014. **402**: p. 84-90.

226. Mohamed, F. and C.F. van der Walle, *Engineering biodegradable polyester particles with specific drug targeting and drug release properties.* Journal of Pharmaceutical Sciences, 2008. **97**(1): p. 71-87.

227. Kehoe, S., X.F. Zhang, and D. Boyd, *Composition-property relationships for an experimental composite nerve guidance conduit: evaluating cytotoxicity and initial tensile strength.* Journal of materials science. Materials in medicine, 2011. **22**(4): p. 945-59.

228. Anderson, M.J. and P.J. Whitcomb, *DOE Simplified: Practical Tools for Effective Experimentation*. 2007: Productivity, Incorporated.

229. Park, J.S., et al., *SOX9 gene plus heparinized TGF-beta 3 coated dexamethasone loaded PLGA microspheres for inducement of chondrogenesis of hMSCs.* Biomaterials, 2012. **33**(29): p. 7151-7163.

230. Tsigkou, O., et al., *Differentiation of fetal osteoblasts and formation of mineralized bone nodules by 45S5 Bioglass conditioned medium in the absence of osteogenic supplements.* Biomaterials, 2009. **30**(21): p. 3542-50.

231. Lee, B.H., et al., *In-situ injectable physically and chemically gelling NIPAAm-based copolymer system for embolization.* Biomacromolecules, 2006. **7**(6): p. 2059-64.

232. Peixoto, L.S., et al., *Expanded Core/Shell Poly(vinyl acetate)/Poly(vinyl alcohol) Particles for Embolization.* Macromolecular Materials and Engineering, 2009. **294**(8): p. 463-471.

233. Yu, J.M., et al., *Preparation and characterization of galactosylated glycol chitosan micelles and its potential use for hepatoma-targeting delivery of doxorubicin.* J Mater Sci Mater Med, 2014. **25**(3): p. 691-701.

234. Mayer, M.I., et al., *Stability of cisplatin, doxorubicin, and mitomycin combined with loversol for chemoembolization.* Ann Pharmacother, 2001. **35**(12): p. 1548-51.

235. Chiadmi, F., et al., *Stability of doxorubicin combined with Radioselectan®, a contrast agent, for chemoembolization.* Journal of Clinical Pharmacy and Therapeutics, 2005. **30**(3): p. 255-258.

236. Vogl, T.J., et al., *Liver, gastrointestinal, and cardiac toxicity in intermediate hepatocellular carcinoma treated with PRECISION TACE with drug-eluting beads: results from the PRECISION V randomized trial.* AJR Am J Roentgenol, 2011. **197**(4): p. W562-70.

237. Amesur, N.B., A.B. Zajko, and B.I. Carr, *Chemo-embolization for unresectable hepatocellular carcinoma with different sizes of embolization particles.* Dig Dis Sci, 2008. **53**(5): p. 1400-4.

238. Heffeter, P., et al., *Resistance against novel anticancer metal compounds: differences and similarities.* Drug Resist Updat, 2008. **11**(1-2): p. 1-16.

239. Biersack, B., et al., *Metal complexes of natural melophlins and their cytotoxic and antibiotic activities.* J Inorg Biochem, 2009. **103**(1): p. 72-6.

240. Coon, J. and J.E. Shelby, *Formation and Properties of Sodium Lanthanum Silicate-Glasses.* Physics and Chemistry of Glasses, 1994. **35**(2): p. 47-51.

241. Branda, F., et al., *Structural role of La2O3 in La2O3-CaO-Na2O-SiO2 glasses.* Physics and Chemistry of Glasses, 2001. **42**(6): p. 385-388.

242. Molieres, E., et al., *Chemical Durability of Lanthanum-Enriched Borosilicate Glass.* International Journal of Applied Glass Science, 2013. **4**(4): p. 383-394.

243. Schaller, T., J.F. Stebbins, and M.C. Wilding, *Cation clustering and formation of free oxide ions in sodium and potassium lanthanum silicate glasses: nuclear magnetic resonance and Raman spectroscopic findings.* Journal of Non-Crystalline Solids, 1999. **243**(2-3): p. 146-157.

244. Lencioni, R., P. Petruzzi, and L. Crocetti, *Chemoembolization of hepatocellular carcinoma.* Semin Intervent Radiol, 2013. **30**(1): p. 3-11.

245. Shelby, J.E., *Introduction to Glass Science and Technology*. 2005, Cambridge: Royal Society of Chemistry.

246. Falenty, K. and S.L. Webb, *Shear modulus, heat capacity, viscosity and structural relaxation time of Na2O-Al2O3-SiO2 and Na2O-Fe2O3-Al2O3-SiO2 melts.* Physics and Chemistry of Minerals, 2010. **37**(9): p. 613-634.

247. Takahashi, S., D.R. Neuville, and H. Takebe, *Thermal properties, density and structure of percalcic and peraluminus CaO-Al2O3-SiO2 glasses.* Journal of Non-Crystalline Solids, 2015. **411**: p. 5-12.

248. Stamboulis, A., R.V. Law, and R.G. Hill, *Characterisation of commercial ionomer glasses using magic angle nuclear magnetic resonance (MAS-NMR).* Biomaterials, 2004. **25**(17): p. 3907-3913.

249. Iftekhar, S., et al., *Glass Formation and Structure-Property-Composition Relations of the RE2O3-Al2O3-SiO2 (RE = La, Y, Lu, Sc) Systems.* Journal of the American Ceramic Society, 2011. **94**(8): p. 2429-2435.

250. Magi, M., et al., *SOLID-STATE HIGH-RESOLUTION SI-29 CHEMICAL-SHIFTS IN SILICATES.* Journal of Physical Chemistry, 1984. **88**(8): p. 1518-1522.

251. Camblor, M.A. and M.E. Davis, *Si-29 Mas Nmr-Spectroscopy of Tectozincosilicates.* Journal of Physical Chemistry, 1994. **98**(50): p. 13151-13156.

252. Stebbins, J.F., *Identification of Multiple Structural Species in Silicate-Glasses by Si-29 Nmr.* Nature, 1987. **330**(6147): p. 465-467.

253. Angeli, F., et al., *Influence of lanthanum on borosilicate glass structure: A multinuclear MAS and MQMAS NMR investigation.* Journal of Non-Crystalline Solids, 2013. **376**: p. 189-198.

254. Linati, L., et al., *Qualitative and quantitative structure-property relationships analysis of multicomponent potential bioglasses.* Journal of Physical Chemistry B, 2005. **109**(11): p. 4989-4998.

255. Kahlenberg, V. and H. Kruger, *LaAlSiO5 and apatite-type La-9.71 (Si-0.8 Al0.19O4)(6)O-2 - the crystal structures of two synthetic lanthanum alumosilicates.* Solid State Sciences, 2004. **6**(6): p. 553-560.

256. Hurt, J.C. and C.J. Phillips, *Structural Role of Zinc Oxide in Glasses in System Na2o-Zno-Sio2.* Journal of the American Ceramic Society, 1970. **53**(5): p. 269-&.

257. Calas, G., et al., *Structure-property relationships in multicomponent oxide glasses.* Comptes Rendus Chimie, 2002. **5**(12): p. 831-843.

258. Varshneya, A.K., *Chemical Durability*, in *Fundamentals of Inorganic Glasses*, A.K. Varshneya, Editor. 1994, Academic Press Inc: San Diego, Ca. p. 397-408.

259. Serra, J., et al., *Influence of the non-bridging oxygen groups on the bioactivity of silicate glasses.* Journal of Materials Science-Materials in Medicine, 2002. **13**(12): p. 1221-1225.

260. Zheng, Q.J., et al., *Structure of boroaluminosilicate glasses: Impact of [Al2O3]/[SiO2] ratio on the structural role of sodium.* Physical Review B, 2012. **86**(5).

261. Hoppe, A., V. Mourino, and A.R. Boccaccini, *Therapeutic inorganic ions in bioactive glasses to enhance bone formation and beyond.* Biomaterials Science, 2013. **1**(3): p. 254-256.

262. Dekervel, J., et al., *Transcatheter Arterial Chemoembolization with Doxorubicin-Eluting Superabsorbent Polymer Microspheres in the Treatment of Hepatocellular Carcinoma: Midterm Follow-up.* Journal of Vascular and Interventional Radiology, 2014. **25**(2): p. 248-255.

263. Sharma, A., S. Venkataperumal, and A. Suman, *Transarterial Chemoembolization (Tace) for Hepatocellular Carcinoma - Comparison between Conventional Technique and Drug Eluting Beads.* Hepatology, 2011. **54**: p. 1411A-1411A.

264. Kato, K. and E. Takayama, *Das Entwasserungsverhalten des Natriummetavanadatdihydrats und die Kristallstruktur des [beta]-Natriummetavanadats.* Acta Crystallographica Section B, 1984. **40**(2): p. 102-105.

265. Wang, Z.H., et al., *Functionalized Nonionic Dextran Backbones by Atom Transfer Radical Polymerization for Efficient Gene Delivery.* Macromolecules, 2011. **44**(2): p. 230-239.

266. Baino, F., et al., *Bioactive glasses: Special applications outside the skeletal system.* Journal of Non-Crystalline Solids, (0).

267. Baskar, R., et al., *Cancer and radiation therapy: current advances and future directions.* Int J Med Sci, 2012. **9**(3): p. 193-9.

268. Curran, M.D. and A.E. Stiegman, *Evolution of V(V) species and the formation of V-O-Si bonds during the synthesis of vanadia-silica sol-gel materials.* Journal of Physical Chemistry B, 2000. **104**(35): p. 8338-8345.

269. Luca, V., D.J. MacLachlan, and K. Morgan, *Synthesis and characterization of porous vanadium silicates in organic medium.* Chemistry of Materials, 1997. **9**(12): p. 2720-2730.

270. Marumo, F., et al., *Alpha-Form of Sodium Metavanadate.* Acta Crystallographica Section B-Structural Science, 1974. **B 30**(Jun15): p. 1628-1630.

271. Shaikh, A.M., *Crystal-Chemistry of Vanadate Pyroxenes - Crystal-Structure Refinement, Na Anisotropy and Rigid Body Analysis of the Thermal Vibration in Ferroelectric Navo3.* Ferroelectrics, 1990. **107**: p. 219-224.

272. Lapina, O.B., et al., *Practical aspects of V-51 and Nb-93 solid-state NMR spectroscopy and applications to oxide materials.* Progress in Nuclear Magnetic Resonance Spectroscopy, 2008. **53**(3): p. 128-191.

273. Kato, K. and E. Takayama, *The Dehydration of Sodium Meta-Vanadate Dihydrate and the Crystal-Structure of Beta-Sodium Metavanadates.* Acta Crystallographica Section B-Structural Science, 1984. **40**(Apr): p. 102-105.

274. Hayakawa, S., T. Yoko, and S. Sakka, *V-51 Nmr-Studies of Crystalline Monovalent and Divalent Metal Metavanadates.* Journal of Solid State Chemistry, 1994. **112**(2): p. 329-339.

275. Enjalbert, R. and J. Galy, *A Refinement of the Structure of V2o5.* Acta Crystallographica Section C-Crystal Structure Communications, 1986. **42**: p. 1467-1469.

276. Eckert, H. and I.E. Wachs, *Solid-State V-15 Nmr Structural Studies on Supported Vanadium(V) Oxide Catalysts - Vanadium-Oxide Surface-Layers on Alumina and Titania Supports.* Journal of Physical Chemistry, 1989. **93**(18): p. 6796-6805.

277. Mekki, A., et al., *Structure and magnetic properties of vanadium-sodium silicate glasses.* Journal of Non-Crystalline Solids, 2003. **318**(1-2): p. 193-201.

278. *Physical Constants of Inorganic Compounds*, in *CRC Handbook of Chemistry and Physics* R. West, Editor. 1989: Boca Raton, Florida p. 1.

279. Wang, F., et al., *Apoptosis-Induction is A Novel Therapeutic Strategy for Gastrointestinal and Liver Cancers.* Current Gene Therapy, 2015. **15**(2): p. 193-200.

280. Luo, J., et al., *Activation of JNK by vanadate induces a Fas-associated death domain (FADD)-dependent death of cerebellar granule progenitors in vitro.* J Biol Chem, 2003. **278**(7): p. 4542-51.

281. Zheng, L.H., et al., *Targeting cellular apoptotic pathway with peptides from marine organisms.* Biochimica Et Biophysica Acta-Reviews on Cancer, 2013. **1836**(1): p. 42-48.

282. Wu, Y.H., et al., *Sodium orthovanadate inhibits growth of human hepatocellular carcinoma cells in vitro and in an orthotopic model in vivo.* Cancer Letters, 2014. **351**(1): p. 108-116.

283. Soares, S.S., et al., *Vanadate induces necrotic death in neonatal rat cardiomyocytes through mitochondrial membrane depolarization.* Chemical Research in Toxicology, 2008. **21**(3): p. 607-618.

284. Zhao, Y.B., et al., *Vanadium compounds induced mitochondria permeability transition pore (PTP) opening related to oxidative stress.* Journal of Inorganic Biochemistry, 2010. **104**(4): p. 371-378.

285. Ray, R.S., et al., *Suppression of cell proliferation, DNA protein cross-links, and induction of apoptosis by vanadium in chemical rat mammary carcinogenesis.* Biochimica Et Biophysica Acta-General Subjects, 2004. **1675**(1-3): p. 165-173.

286. Ray, R.S., et al., *Suppression of cell proliferation, induction of apoptosis and cell cycle arrest: Chemopreventive activity of vanadium in vivo and in vitro.* International Journal of Cancer, 2007. **120**(1): p. 13-23.

287. Hotta, M. and K. Yamamoto, *Comparative Radiopacity of Bonding Agents*. Journal of Adhesive Dentistry, 2009. **11**(3): p. 207-212.

288. Meng, W.J., et al., *Preparation and evaluation of biocompatible long-term radiopaque microspheres based on polyvinyl alcohol and lipiodol for embolization.* J Biomater Appl, 2015.

289. Lee, N., et al., *Multifunctional Fe3O4/TaO(x) core/shell nanoparticles for simultaneous magnetic resonance imaging and X-ray computed tomography.* J Am Chem Soc, 2012. **134**(25): p. 10309-12.

290. Wischke, C. and S.P. Schwendeman, *Principles of encapsulating hydrophobic drugs in PLA/PLGA microparticles.* Int J Pharm, 2008. **364**(2): p. 298-327.

291. Mok, H. and T.G. Park, *Water-free microencapsulation of proteins within PLGA microparticles by spray drying using PEG-assisted protein solubilization technique in organic solvent.* Eur J Pharm Biopharm, 2008. **70**(1): p. 137-44.

292. Fu, Q., et al., *Silicate, borosilicate, and borate bioactive glass scaffolds with controllable degradation rate for bone tissue engineering applications. II. In vitro and in vivo biological evaluation.* J Biomed Mater Res A, 2010. **95**(1): p. 172-9.

293. Fu, Q., et al., *Silicate, borosilicate, and borate bioactive glass scaffolds with controllable degradation rate for bone tissue engineering applications. I. Preparation and in vitro degradation.* J Biomed Mater Res A, 2010. **95**(1): p. 164-71.

294. Spencer, L., et al., *Structural analysis of lanthanum-containing battery materials using La-139 solid-state NMR.* Canadian Journal of Chemistry-Revue Canadienne De Chimie, 2011. **89**(9): p. 1105-1117.

295. Dithmer, L., et al., *Characterization of Phosphate Sequestration by a Lanthanum Modified Bentonite Clay: A Solid-State NMR, EXAFS, and PXRD Study.* Environmental Science & Technology, 2015. **49**(7): p. 4559-4566.

296. Rollet, A.L., H. Matsuura, and C. Bessada, *An in situ spectroscopic study of the local structure of oxyfluoride melts: NMR insights into the speciation in molten LiF-LaF3-Li2O systems.* Dalton Transactions, 2015. **44**(2): p. 522-529.

297. *Chapter 8 NMR of Low-gamma Nuclides*, in *Multinuclear Solid-State NMR of Inorganic Materials*, J.D.M. Kenneth and E.S. Mark, Editors. 2002, Pergamon. p. 511-14.

298. Brauer, D.S., R.M. Wilson, and T. Kasuga, *Multicomponent phosphate invert glasses with improved processing.* Journal of Non-Crystalline Solids, 2012. **358**(14): p. 1720-1723.

299. Talos, F., et al., *Effect of titanium ions on the ion release rate and uptake at the interface of silica based xerogels with simulated body fluid.* Corrosion Science, 2013. **72**: p. 41-46.

300. Novajra, G., et al., *Effects of TiO2-containing phosphate glasses on solubility and in vitro biocompatibility.* Journal of Biomedical Materials Research Part A, 2011. **99A**(2): p. 295-306.

301. Ahmed, I., et al., *Cytocompatibility and Effect of Increasing MgO Content in a Range of Quaternary Invert Phosphate-based Glasses.* Journal of Biomaterials Applications, 2010. **24**(6): p. 555-575.

302. D'Inca, H., et al., *Automated Quantification of Tumor Viability in a Rabbit Liver Tumor Model after Chemoembolization Using Infrared Imaging.* Am J Pathol, 2015. **185**(7): p. 1877-88.

303. Choi, J.W., et al., *Comparison of drug release and pharmacokinetics after transarterial chemoembolization using diverse lipiodol emulsions and drug-eluting beads.* PLoS One, 2014. **9**(12): p. e115898.

Appendix A

Chapter 6 is published in the Journal of Biomaterials Applications with permission

Authors Reusing Their Own Work

(https://us.sagepub.com/en-us/nam/journals-permissions)

SAGE Journal authors are able to use their article in certain circumstances without any further permission. The chart above includes common requests and an explanation of which 'version' of the article can be used in each circumstance.

- Version 1 – original submission to the journal (before peer review)
- Version 2 – original submission to the journal with your revisions after peer review, often the version accepted by the editor
- Version 3 – copy-edited and typeset proofs and the final published version

I WANT TO:	CLEARED	REQUIRES PERMISSIONS
supply my article to my students or use the article for teaching purposes	Version 3	
supply my article to a research colleague at an academic institution	Version 3	
supply my article to a commercial organization for republication, distribution or a web posting		X
upload my article to my institution repository or department website	Version 2	
upload my article to a repository NOT affiliated with my institution, 12	Version 2	

I WANT TO:	CLEARED	REQUIRES PERMISSIONS
months after publication		
republish my article in a book I am writing or editing	Version 3	
contribute my article to a book edited or written by someone else		X

For the full explanation of SAGE's Journal Author Reuse Policy and for other resources, please visit our Journal Author Gateway.

For advice on how to clear permission for a manuscripts you intend to submit to for publication in a SAGE Journal, please visit our Author GatewayCopyright and Permissions FAQ.

Open Access

If you wish to re-use an Open Access article under a Creative Commons License, visit our page on Re-use of Open Access Content for more information.

Appendix B

Chapter 7 is published in the Journal of Non-Crystalline Solids with permission

Article Sharing

http://www.elsevier.com/about/company-information/policies/sharing

Authors who publish in Elsevier journals can share their research by posting a free draft copy of their article to a repository or website. Researchers who have subscribed access to articles published by Elsevier can share too. There are some simple guidelines to follow, which vary depending on the article version you wish to share.

Preprint

Accepted manuscript

Published article

Help and support

Preprint

- Authors can share their preprint anywhere at any time.
- If accepted for publication, we encourage authors to link from the preprint to their formal publication via its Digital Object Identifier (DOI). Millions of researchers have access to the formal publications on ScienceDirect, and so links will help your users to find, access, cite, and use the best available version.
- Authors can update their preprints on arXiv or RePEc with their accepted manuscript .

Please note:

- Cell Press, The Lancet, and some society-owned titles have different preprint policies. Information on these is available on the journal homepage.
- Preprints should not be added to or enhanced in any way in order to appear more like, or to substitute for, the final versions of articles.

Accepted Manuscript

Authors can share their accepted manuscript:

Immediately

- via their non-commercial personal homepage or blog

- by updating a preprint in arXiv or RePEc with the accepted manuscript
- via their research institute or institutional repository for internal institutional uses or as part of an invitation-only research collaboration work-group
- directly by providing copies to their students or to research collaborators for their personal use
- for private scholarly sharing as part of an invitation-only work group on commercial sites with which Elsevier has an agreement

After the embargo period

- via non-commercial hosting platforms such as their institutional repository
- via commercial sites with which Elsevier has an agreement

In all cases accepted manuscripts should:

- link to the formal publication via its DOI
- bear a CC-BY-NC-ND license – this is easy to do, click here to find out how
- if aggregated with other manuscripts, for example in a repository or other site, be shared in alignment with ourhosting policy
- not be added to or enhanced in any way to appear more like, or to substitute for, the published journal article

---

Published Journal Article

Policies for sharing published journal articles differ for subscription and gold open access articles:

Subscription articles

- If you are an author, please share a link to your article rather than the full-text. Millions of researchers have access to the formal publications on ScienceDirect, and so links will help your users to find, access, cite, and use the best available version
- Theses and dissertations which contain embedded PJAs as part of the formal submission can be posted publicly by the awarding institution with DOI links back to the formal publications on ScienceDirect
- If you are affiliated with a library that subscribes to ScienceDirect you have additional private sharing rights for others' research accessed under that agreement. This includes use for classroom teaching and internal training at the institution (including use in course packs and courseware programs), and inclusion of the article for grant funding purposes
- Otherwise sharing is by agreement only